Characterization of fiber tapers for fiber devices and sensors

by

Xiaozhen Wang

Thesis submitted to the
Faculty of Graduate and Postdoctoral Studies
In partial fulfillment of the requirements for the Degree of

Doctor of Philosophy

in

Physics

Ottawa-Carleton Institute for Physics
University of Ottawa

To my family

Abstract

Fiber tapers have attracted much attention and have been successfully employed in various applications, ranging from resonators, filters, interferometers to sensors. This thesis studies the properties of fiber tapers for the purpose of making tapered-based devices and sensors in aerospace related application where small size and light weight are critical.

This thesis includes theoretical derivation and experimental verifications of distributed mode coupling in tapered single-mode fibers (SMFs) with high-resolution optical frequency-domain reflectometry (OFDR) technique. The studies are realized with OFDR through phase detection of a Mach-Zehnder interferometer (MZI), which measures local refractive index change relative to the reference arm. The wavelength shifts converted by the phase change give the group index differences between the fundamental mode and higher-order modes of fiber tapers. The energy re-distribution is observed in Rayleigh backscatter amplitude as a function of fiber length with a $\sim$13μm resolution over the entire fiber taper, and group index difference between core and cladding modes is measured with a spatial resolution of $\sim$2cm by using autocorrelation data processing.

The thermal and mechanical properties of fiber tapers have also been characterized with OFDR. The cross-correlation wavelength shift is related to the refractive index change of the modes. It is shown that residual stress induced by the tapering process results in the inhomogeneous thermal property, which can be significantly reduced by an annealing treatment. A fiber taper with a waist diameter of $\sim$6μm has a force sensitivity of $\sim$620.83nm/N, $\sim$500 times higher than that of SMF. Furthermore, polarization-preserving character of tapered polarization-maintaining fibers (PMFs) is evaluated by OFDR-based distributed birefringence along tapered PMFs.

Three tapered-based micro-fiber devices have been used as effective mode selecting components to build narrow-linewidth tunable Erbium-doped fiber ring lasers. The fabrication is easy and at a low cost. 1) a tapered fiber tip forms multimode interference mechanism; 2) a two-taper MZI has been demonstrated by splitting/combining the fun-

damental mode and higher-order modes through fiber tapers and is tuned by bending one taper waist; 3) a novel tunable fiber Fabry-Perot filter, consisting of a hollow-core photonic bandgap fiber and a micro-fiber, is employed in the reflection mode.

Statement of Originality

This work contains no material which has been accepted for the award of any other degree or diploma in any university or other tertiary institution and, to the best of my knowledge and belief, contains no material previously published or written by another person, except where due reference has been made in the text.

I give consent to this copy of my thesis, when deposited in the University Library, being available for loan and photocopying.

SIGNED:. . . . . .

DATE:. . . . . .

Supervisor: Dr. Xiaoyi Bao

Acknowledgements

I am sincerely grateful to my advisor, Professor Xiaoyi Bao, for her guidance and support throughout my PhD studies. It is a great honor for me to know her both at the professional and personal level. Her broad knowledge, thoughtful insight, and positive attitude set a great example for me to take challenges both in research and life in the future.

I would like to express my great gratitude to Professor Liang Chen for his helpful and insightful suggestions during my research processes, which significantly improves the quality of this thesis.

I would like to acknowledge Dr. Yi Li, Dr. Wenhai Li, and Dr. Tao Zhu for their suggestions. It is a great pleasure to collaborate with them to conduct several exciting research projects.

I would like to appreciate Dr. Yongkang Dong, Dr. Dapeng Zhou, Dr. Ping Lu and Mr. Guolu Yin for helpful technical discussions and Jeremie Harris and Graeme Niedermayer for careful proofreading of this thesis. Aslo, I would like to thank Professor Wojtek Bock for supporting my experiment.

I would like to thank my other colleagues in Fiber Optics group – Dr. Yun Li, Mr. Zengguang Qin, and Ms. Xuan Liu – with whom I had many fruitful conversations on technical and non-technical topics. I am indebted to my dear friends Lufei Chen and Huihong Qiu, who have always been there to share the joy and sorrow of life.

I am thankful to Professor Xiaopeng Dong for his guidance and support during my graduate studies at Xiamen University. I would like to acknowledge funding support by the China Scholar Council over the past four years.

I cannot end without thanking my family, especially my parents and my husband, Bin Li, for their deep love, support and encouragement. Their care and understanding allowed me to attack obstacles with great confidence.

Contents

List of Tables

List of Figures

List of Acronyms

ASE	Amplified spontaneous emission
AOM	Acousto-Optical Modulator
BOTDA	Brillouin optical time-domain analysis
DAQ	Data acquisition card
EDF	Erbium-doped fiber
EDFA	Erbium-doped fiber amplifier
EDFRL	Erbium-doped fiber ring lasers
ER	Extinction ratio
ESA	Electrical spectrum analyzer
FBG	Fiber Bragg grating
FFT	Fast Fourier transfer
FSR	Free spectral range
FP	Fabry-Perot
FUT	Fiber under test
FWHM	Full-width at half-maximum
HC-PBF	Hollow-core photonic bandgap fiber
ISO	Isolator
LP	Linearly polarized
LPF	Low-pass filter
LPG	Long-period fiber grating
MFD	Mode field diameter

MMF	Multimode fiber
MZI	Mach-Zehnder interferometer
OFDR	Optical frequency-domain reflectometry
OPD	Optical path difference
OSA	Optical spectrum analyzer
OTDR	Optical Time domain reflectometry
PBS	Polarization beam splitter
PBG	Photonic bandgap
PC	Polarization controller
PD	Photodetector
PDL	Polarization dependent loss
PER	Polarization extinction ratio
PMF	Polarization-maintaining fiber
SLM	Single longitudinal mode
SMF	Single-mode fiber
SMSR	Side-mode suppression ratio
SOA	Semiconductor amplifier
SOP	State of polarization
TLS	Tunable laser source
WDM	Wavelength division multiplexing

Chapter 1

Introduction

Over the past three decades, tapered fibers have attracted much attention and have been successfully employed in many interesting applications, ranging from resonators, filters, interferometers, lasers to sensors. This thesis focuses on developing a distributed measurement of refractive index differences along a fiber taper and investigating its thermal and mechanical properties using high-resolution optical frequency-domain reflectometry (OFDR) technique. Secondly, three novel fiber taper-based devices, including a tapered fiber tip, a two-taper Mach-Zehnder interferometer (MZI) and a Fabry-Perot interferometer (FPI) consisting of a micro-fiber and a hollow-core photonic bandgap fiber (HC-PBF), have been separately employed as effective mode selecting components to build narrow-linewidth tunable Erbium-doped fiber ring lasers (EDFRL).

This chapter introduces the background, motivation, and contribution of the research work. Section 1.1 reviews the development of tapered fiber and its application. Section

1.2 clarifies the motivation of our research. Section 1.3 focuses on the contributions that we made to distributed mode coupling analysis along a fiber taper and on improvement of tunable fiber lasers. Section 1.4 presents the thesis outline.

1.1 Background

In the 1980s, studies on tapered fibers mainly focused on fused single-mode fiber (SMF) taper couplers [3, 4] and fiber polarizers based on tapered polarization-maintaining fiber (PMF) [5]. A reasonable parabolic model for a fiber taper shape was proposed in this period [6, 7]. Two complementary delineation criteria, including taper angle criterion and weak power transfer criterion, with both theoretical and experimental justification, were presented in 1991 [1, 8]. Practical procedures for the fabrication of fiber tapers with any reasonable shape were discussed in detail [9] and various fabrication technologies have been reported, such as a H_2 flame heating and stretching technique[9], a CO_2 laser heating and stretching approach [10], and a chemical etching method[11].

During the late 1990s and early 2000s, an optical fiber taper was used as a coupler for a high-Q microsphere resonator. This is because tapered fibers not only expose the evanescent field to the surroundings, but also have much stronger evanescent fields [12]. By adjusting the taper diameter to match the propagation constant of the mode in the taper with that of whispering-gallery modes (WGM) at the surface of a fused-silica microsphere, one can couple more than 90% of the light into the sphere [13, 14]. Furthermore, a fiber taper, placed in contact with a microsphere, could be made to form

a compact fiber laser with a side-mode suppression ratio (SMSR) of ∼40dB [15].

A designed taper featuring a long and highly uniform waist region was also successfully applied as a modal filter. This is because higher-order modes leaked from the taper by absorption, higher index coating, mode coupling to higher-order modes, or a combination of these principles [16]. By controlling the transition taper profile and reducing the diameter to sub-wavelength level (∼1μm), a truly single-mode operation was achieved over a broad spectral window (400–1700nm) [17].

Since 2000, taper-based devices have been widely used for strain, displacement, temperature, humidity and refractive index sensing [18–24]. Tapering is a simple, efficient, and low-cost method for mode conversion from the fundamental mode to higher-order modes. For example, an SMF taper can easily exhibit linearly polarized (LP) modes beating, LP_{01}–LP_{02}, in the waist region. One taper with a gold-coated end builds a fiber Michelson interferometer and two concatenating tapers form a fiber MZI. By contrast, the fabrication of fiber Bragg grating (FBG) requires expensive phase-masks. Taper-based sensors allow for sensitivity similar to that of FBG or long period grating (LPG)-based devices but are fabricated more easily and at a lower cost. The intended purpose of these designs is to couple the light from the fundamental core mode to the cladding modes and vice-versa. Since the core mode and the cladding modes have different propagation constants, the optical path difference (OPD) between them leads to interferences in the transmission spectra. Furthermore, the core mode and the cladding modes exhibit different responses to various external factors. Thus, the transmission spectra change when

the OPD value is altered and the environmental changes are detected.

1.2 Motivation

Tapering is a useful technique, which allows higher-order modes to be excited in a fiber by reducing its diameter to a few micrometers. When a standard SMF is tapered to pass the core-to-cladding mode transition point [25], higher-order modes are generated within this transition region. The mode coupling process along a tapered fiber occurs at the down-taper and up-taper regions with large taper slopes, while beating, instead of coupling, between the guided local modes occurs at the central quasi-adiabatic uniform waist region [26]. Earlier theoretical work evaluated the mode power evolution along the tapered fiber and gave the delineation criteria for mode coupling [8, 26, 27]. Experimental observations investigated the spectral response of the taper as a sinusoidal function, which signified the presence of two dominant modes participating in the interference [28]. The presence of more than two modes in the tapered fiber was understood to result from the power oscillation by varying the external index [27]. The distributed power oscillation along the tapered fiber was measured point-by-point by moving a thin film perturbation along the tapered fiber [26]. Another common method, the cutback measurement, was performed to find the exact transverse transmission spectra at different positions along the taper [29]. However, this destructive technique did not count the mode coupling continuously. In addition, during the tapering process, stress is introduced to the fiber taper and causes an inhomogeneous refractive index distribution. This will degrade the optical quality of

fiber taper for its applications. To the best of our knowledge, the thermal and mechanical properties, particularly their variations at different locations along a tapered fiber, have not been studied.

The application of fiber tapers as mode selecting components in an EDFRL configuration attracts our attention. Tunable optical bandpass filters are crucial components in tunable lasers, which are widely used in wavelength division multiplexed (WDM) communications, fiber sensors, high-resolution spectroscopy and optical coherent tomography. Filter features include wide tuning range, high SMSR, narrow optical passband, small size, and low cost. All-fiber-based filters include FBGs [30–32], in-line Fabry-Perot (FP) filters [33], arrayed waveguide gratings (AWGs) [34] and filters based on special fibers, such as multimode fibers (MMFs) [35], few-mode high-birefringence fibers (FM-HBFs) [36], tapered fibers [28]. Optical filters made by FBG can be tuned by either thermal or mechanical stress effects. The temperature sensitivity of FBG ($\sim$10pm/°C) limits the measurement accuracy of the wavelength shift to a nanometer region. A FBG filter based on piezoelectric stack actuators works over a tuning range of 45nm while its 3dB bandwidth reaches 0.7nm [30]. In-line fiber FP filters with bandwidths of tens of Megahertz to tens of Gigahertz range are commercially available, but they are rather expensive and their tuning ranges are limited to less than 1 nm because the cavity lengths are changed by the piezoelectric stretching elements. MMF filters have a larger tuning range of 60nm with tuning steps of 2.5–3nm and an SMSR of 40dB [35]. A new type of tunable laser, based on FM-HBFs, has also been reported recently. This new laser has a tuning range

in excess of 40nm with a tuning step of about 2.2nm and an SMSR of 40dB [36]. AWGs themselves are not tunable and they need to be combined with additional switching devices to achieve tunability. A polymeric AWG multiplexer has a tuning range wider than 10nm with a temperature change of 55°C [34], while its 3dB bandwidth is 0.2nm. By stretching an SMF taper, an EDFRL has a tuning range of over 20nm, a tuning step of over 2nm, a linewidth of 0.05nm and an SMSR better than 45dB over the entire tuning range [28]. Therefore, none of these optical filters have a tunable narrow bandwidth (pm resolution) over a wide tuning range (a few nanometers or more).

1.3 Thesis contributions

In this thesis, we develop a technique for the distributed mode coupling measurement along a fiber taper length and study the thermal and mechanical properties of a fiber taper using a high spatial resolution OFDR system. Secondly, three effective mode selecting components, including a tapered fiber tip, a two-taper MZI and an FPI including a micro-fiber and a HC-PBF, have been separately employed to build narrow-linewidth tunable fiber ring lasers.

First, the refractive index difference measurement between the fundamental mode and higher-order modes of fiber tapers using OFDR technique are theoretically derived. To the best of our knowledge, mode coupling along an SMF taper is observed continuously for the first time. The energy re-distribution through Rayleigh backscatter amplitude is detected with a $\sim$13μm resolution over the whole taper region. The refractive index

differences between the fundamental mode and higher-order modes of gentle tapers and abrupt tapers are measured with a spatial resolution of ∼2cm through wavelength shifts calculated by autocorrelation data processing. The experimental results match well with theoretical values.

Secondly, thermal and mechanical properties of fiber tapers are also investigated by using high-resolution, high-sensitivity OFDR technique. It is found that the spectral shifts induced by a temperature or strain change in the fiber taper region are strongly related to the refractive index change of the fundamental mode. It is shown that residual stress induced by the taper process results in inhomogeneous thermal properties, which are eliminated by an annealing treatment. The wavelength-force sensitivity is dramatically enhanced by the reduced waist diameter of the taper. It was found that a taper with a waist diameter of $\sim 6\mu$m has a high force sensitivity, ∼500 times higher than that of a standard SMF.

A simple and cost-effective tunable ring laser is built based on the interference of the spatial modes of a tapered SMF tip. Three optical amplifiers, including a semiconductor amplifier (SOA), an L-band erbium-doped fiber amplifier (EDFA), and a C-band EDFA, and two SMF tips with different slopes are separately employed by the fiber ring. In order to improve the laser parameters, such as SMSR, linewidth, and tuning range, we study the effects of the amplifier's relaxation time and gain, and the steepness of fiber tips. Furthermore, a chemical etching method is applied to enhance laser performance.

A stable C- and L-band tunable fiber ring laser is demonstrated by using a two-taper

MZI filter. The laser wavelength is tuned by mechanically bending one of the two taper waists. Amplified by an erbium-doped fiber (EDF) and an L-band EDFA, respectively, the fiber ring laser has a full C- and L-band tuning range with an SMSR as high as 50dB. The laser linewidth and minimum tuning step are related to the MZI's cavity length. It was also found that thermal annealing relieved the internal stresses within the tapers and substantially enhanced laser performance.

A novel tunable fiber FP filter is assembled using a HC-PBF and a micro-fiber. The interference cavity is the hollow core of a HC-PBF. One of the reflection mirrors is the splicing point between a section of HC-PBF and a SMF. The other reflection mirror is the gold-coated end of a chemical etched micro-fiber, which has a cladding diameter similar to the core diameter of a HC-PBF. Hence this inserted mirror is adjusted with long distance inside the hollow core of HC-PBF. This tunable FP filter is used as a mode selecting component in the reflection mode to implement stable single longitudinal mode (SLM) operation in a ring laser. With FP cavity length of 2.37±0.37mm, the SLM-EDFRL has an SMSR of ∼50dB and a linewidth less than 3kHz over 1557.3–1560.2nm.

1.4 Thesis outline

This thesis contains nine chapters and is organized as follows.

Chapter 1 reviews the development and applications of optical fiber tapers and outlines the motivations and contributions of this thesis. Chapter 2 presents the principle of optical fiber tapers based on the calculation of effective refractive index and describes

some related fabrication technologies. Chapter 3 focuses on theoretical study and experimental measurement of distributed mode coupling along the SMF taper with the OFDR technique. Chapter 4 investigates thermal and mechanical properties of fiber tapers by using a high-resolution, high-sensitivity OFDR scheme. A highly sensitive distributed force sensor has been demonstrated based on the mechanical characteristics of fiber tapers. Chapter 5 proposes a method to evaluate polarization-preserving character of tapered polarization-maintaining fibers (PMFs) by using OFDR-based distributed birefringence measurement along tapered PMFs.

In chapter 6, a simple and cost-effective tunable ring laser, which is tuned by the spatial modes interference of a tapered SMF tip, is proposed. The principle is demonstrated and laser performances are studied by using different optical amplifiers inside the fiber ring. The effect of the fiber tip shape is also analyzed. Furthermore, the chemical etching method is applied to improve the laser performance. Chapter 7 demonstrates a stable C- and L-band tunable fiber ring laser by using a two-taper MZI as a filter. The tunability mechanism is shown and fiber lasers with two different gain media are separately proposed. Thermal annealing is introduced and substantially enhanced the laser performance. Chapter 8 presents a novel tunable fiber FP filter by using a HC-PBF and a micro-fiber. The principle and fabrication of the FP filter are shown in detail. A simple and efficient mode selection mechanism is presented and stable SLM operation is demonstrated in the experiments.

Chapter 9 concludes all the work we have done and discusses some future topics.

Chapter 2

Physics of fiber taper

This chapter covers several important concepts necessary for the understanding of optical fiber tapers. Section 2.1 calculates the effective refractive indices of the core mode and the cladding modes along the fiber taper. Several important values, including the core-cladding transition value, and adiabaticity criterion based on the upper boundary of the core taper angle, are discussed. Section 2.2 lists three common fabrication techniques.

2.1 Principle

2.1.1 Wave equations for fiber taper

A fiber taper consists of a core embedded in a finite cladding, which is surrounded by air. At the beginning of a fiber taper, the fundamental mode, linearly polarized (LP) mode, LP_{01} is the only propagation mode in the fiber and propagates as the core mode,

which is defined to be the state when its effective refractive index n_{eff} lies between the cladding index n_{cl} and the core index n_{co}. When the core diameter is reduced during tapering, n_{eff} of the core mode decreases continually. The guided core mode exists in the infinite-cladding geometry with an effective index n_{eff}, which satisfies $n_{cl} < n_{eff} < n_{co}$. Here the thickness of the cladding can be assumed to be infinite and the cladding-air interface is negligible. Each cladding mode with an effective index n_{eff}, which satisfies $n_{air} < n_{eff} < n_{cl}$, is guided by the core-finite cladding-air waveguide. n_{air} is the refractive index of surrounding air. When we analyze the cladding modes, we evaluate the field on two boundary conditions, including the core-cladding and cladding-air interfaces, using a three-layer step-index fiber model [37].

First, we calculate the refractive index of the core mode. The weak-guidance approximation is applied due to a slight variation between the core and cladding indices. Thus the propagation constants for the local LP modes are obtained accurately by solving a set of scalar wave equations with continuity of the solution and its first derivative at the core-cladding interface along the fiber taper. Here we assume the ratio of cladding to core diameters S remains constant under tapering.

The electromagnetic fields, propagating in z-direction along the fiber, must satisfy the scalar wave equation, which is expressed in cylindrical coordinates (r, ϕ, z)

$$\left\{ \frac{\partial^2}{\partial r^2} + \frac{1}{r}\frac{\partial}{\partial r} + \frac{1}{r^2}\frac{\partial^2}{\partial \phi^2} + k^2 n^2 - \beta^2 \right\} \psi = 0, \tag{2.1}$$

where ψ represents electric or magnetic field, the wavenumber $k = \frac{2\pi}{\lambda}$ in terms of the free-space wavelength λ, n is the refractive index profile, and β the propagation constant, $\beta = kn_{eff}$.

For the core mode with $n_{cl} < n_{eff} < n_{co}$, we consider the bounded solution with the core-cladding interface and ignore the field in the air. The fiber parameter and modal parameters are defined by

$$u_1 = k\left(n_{co}^2 - n_{eff}^2\right)^{\frac{1}{2}}, \tag{2.2a}$$

$$w = k\left(n_{eff}^2 - n_{cl}^2\right)^{\frac{1}{2}}. \tag{2.2b}$$

We have the solution of Eq. (2.1) as follows,

$$\psi = \begin{cases} AJ_\upsilon\left(u_1 r\right) e^{i\upsilon\phi} & \text{if } 0 \le r \le \rho; \\ CK_\upsilon\left(wr\right) e^{i\upsilon\phi} & \text{if } \rho \le r \le \rho_{cl}. \end{cases} \tag{2.3}$$

where A and C are constants, ρ and ρ_{cl} are core and cladding radii, respectively. J_υ and K_υ are the υth-order Bessel function of the first kind and the modified Bessel function of the second kind, respectively. For the LP_{0m} modes and LP_{1m} modes, $\upsilon = 0$ and $\upsilon = 1$, respectively. Continuity of electromagnetic field ψ and its first derivative $\frac{d\psi}{dr}$ at the core boundary $r = \rho$ relates the values of A and C and leads to a set of the eigenvalue

equations. We obtain the following mode condition [38]

$$u_1 \frac{J_{\upsilon+1}(u_1\rho)}{J_\upsilon(u_1\rho)} = w\frac{K_{\upsilon+1}(w\rho)}{K_\upsilon(w\rho)}. \tag{2.4}$$

The eigenvalues obtained from Eq. (2.4) are labeled as $\beta_{\upsilon m}$ with $\upsilon = 0, 1, 2, \ldots, m = 1, 2, 3, \ldots$, where the subscript m indicates the mth root of Eq. (2.4). The modes are designated $\mathrm{LP}_{\upsilon m}$.

For the cladding mode with $n_{air} < n_{eff} < n_{cl}$, we consider the bounded solutions with the core-cladding and cladding-air interfaces. A three-layer step-index fiber model with dispersion relation is proposed [37] and a list of clearer, ready-to-program relations is included [39]. With defined modal parameters,

$$u_1 = k\left(n_{co}^2 - n_{eff}^2\right)^{\frac{1}{2}}, \tag{2.5a}$$

$$u_2 = k\left(n_{cl}^2 - n_{eff}^2\right)^{\frac{1}{2}}, \tag{2.5b}$$

$$w_3 = k\left(n_{eff}^2 - n_{air}^2\right)^{\frac{1}{2}}, \tag{2.5c}$$

The solution of Eq. (2.1) is as follows,

$$\psi = \begin{cases} AJ_\upsilon(u_1 r)\, e^{i\upsilon\phi} & \text{if } 0 \le r \le \rho; \\ \left[BJ_\upsilon(u_1 r) + CY_\upsilon(u_2\rho)\right] e^{i\upsilon\phi} & \text{if } \rho \le r \le \rho_{cl}; \\ DK_\upsilon(w_3 r)\, e^{i\upsilon\phi} & \text{if } r \ge \rho_{cl}. \end{cases} \tag{2.6}$$

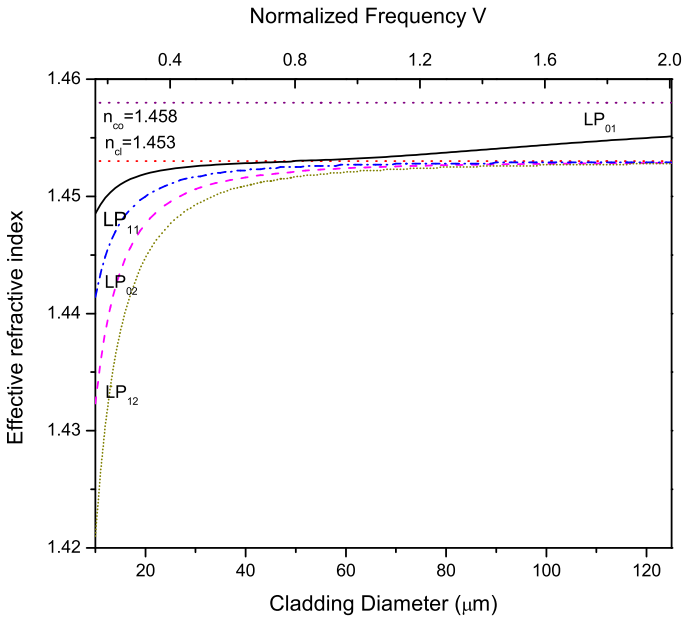

Figure 2.1: Effective refractive index of the LP_{vm} modes at wavelength $\lambda = 1550nm$, when a SMF-28^{TM} is tapered with a constant ratio of cladding to core diameter.

where A, B, C and D are constants, Y_v is the vth-order Bessel function of the second kind. Continuity of electric field and magnetic field and their first derivative at these two interfaces leads to a set of equations which relate the values of A-D and provide the eigenvalue equation from the consistency condition. Effective refractive indices of the LP_{vm} modes are plotted as a function of cladding diameter of fiber taper, as shown in Fig. 2.1. Detailed derivation could be found in Appendix A.

2.1.2 The core-cladding transition

As discussed above, n_{eff} of the core mode decreases continually as the core diameter is reduced during tapering. When n_{eff} approaches the cladding index, the core mode

LP_{01} is not guided any more and the cladding modes are generated at the state with $n_{air} < n_{eff} < n_{cl}$. The modes continue to propagate in the cladding. This is also called the core mode "cutoff" [1, 29]. The core-cladding transition value $V_{core/cladding}$ is given by [25]

$$V_{core/cladding} = \frac{2\pi}{\lambda}\frac{d}{2S}\sqrt{n_{co}^2 - n_{cl}^2} \cong \sqrt{\frac{2}{\ln S}}\{1 + \frac{0.26}{\ln S}\}^{-\frac{1}{2}}, \tag{2.7}$$

where d is cladding diameter of a fiber taper. For SMF-28^{TM}, core diameter is 8.2μm and cladding diameter is 125μm, and the ratio of cladding to core diameter is S=15.24 and we have $V_{core/cladding}$=0.82. Here, we assume the ratio S remains constant under tapering. Theoretically, the fundamental core mode is split into several cladding modes when the fiber is tapered down to a cladding diameter of 51.1μm.

2.1.3 Adiabaticity criterion

A fiber taper is approximately adiabatic if the local taper angle $\Omega(z)$ is small enough everywhere to ensure that there is no power transfer between different modes as the light propagates along the fiber taper length. As illustrated in Fig. 2.2, the local taper length-scale z_t is defined as the height of a right circular cone with base coincident with the local core cross-section. The local core taper angle $\Omega(z)$, the distance along the taper z, the local core radius $\rho(z)$ satisfy $\tan\Omega(z) = \frac{d\rho(z)}{dz}$. Because in practice $\Omega(z) \ll 1$, we have

$$\Omega(z) \approx \frac{d\rho(z)}{dz} \approx \frac{\rho(z)}{z_t(z)}. \tag{2.8}$$

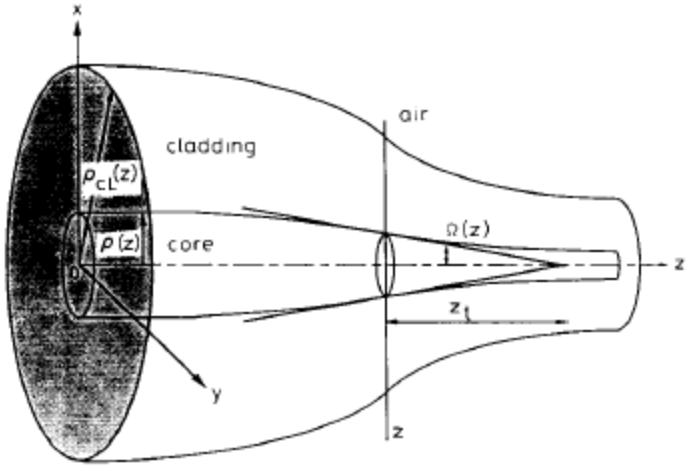

Figure 2.2: Tapered fiber showing finite cladding and air as surrounding medium [1].

The local coupling length between the fundamental and higher-order cladding mode is taken to be the beat length $z_b(z)$, where

$$z_b(z) = \frac{2\pi}{\beta_1(z) - \beta_2(z)}, \tag{2.9}$$

with the propagation constants $\beta_1(z)$ and $\beta_2(z)$. If a fiber taper has $z_t \gg z_b$ everywhere along its length, the fundamental mode will propagate approximately adiabatically with negligible coupling loss. Conversely, if $z_t \ll z_b$, the coupling will be significant and the fundamental mode will propagate nonadiabatically. Using the condition $z_t = z_b$, an approximate delineation between adiabatic and nonadiabatic tapers is equivalent to

$$\overline{\Omega}(z) = \frac{\rho(z)(\beta_1(z) - \beta_2(z))}{2\pi}. \tag{2.10}$$

The difference of effective indices between LP_{01} and LP_{0m} ($m > 1$) modes determines the core taper adiabatic angle Ω. The values of propagation constants for the LP_{01} and LP_{02} modes in Fig. 2.1 determines the taper adiabatic core taper angle at λ=1550nm through Eq. (2.10). This criterion is plotted as the red curve in Fig. 2.3 in radians, as a function of the normalized tapered core radius $\rho(z)/\rho$. The minimum of the curve corresponds to the smallest separation of the effective indices for the LP_{01} and LP_{02} modes in Fig. 2.1. To the right of the minimum, the fundamental mode is guided more by the core, whereas to the left, the same mode is increasingly guided by the finite cladding. As shown in Fig. 2.3, the core taper angle profiles of "abrupt tapers" and "Gentle tapers" are shown as the blue and green curves, respectively. When the core taper angle is greater than the adiabatic criterion, it means that the LP_{01} mode will be converted to $LP_{0m}(m > 1)$ modes. If the core taper angle is smaller than the adiabatic criterion over the whole taper, the taper is adiabatic. This simulation result is helpful to design an optimal adiabatic taper shape.

These abrupt tapers are LP_{01}–LP_{02} modal interferometers. Typically a "coupling-beating-coupling" structure is created [26]. The initial single-mode jacketed fiber supports only the LP_{01} mode followed by a jacket-off tapered region which generates cladding-mode propagation. Principally the LP_{02} mode is excited in the non-adiabatic part of a down-taper region, which then beats with the LP_{01} mode in a central adiabatic region. The LP_{02} mode may be coupled back to LP_{01} in the non-adiabatic part of an up-taper region depending on the relative phase. Finally, at the taper output the fibre jacket

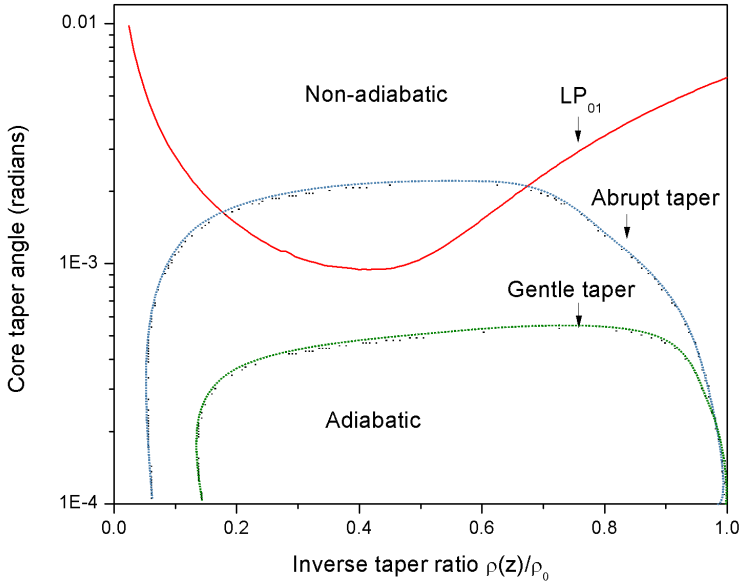

Figure 2.3: The core taper angle profile as a function of the normalized tapered core radius $\rho(z)/\rho$ at wavelength λ=1550nm. The red curve shows the adiabatic core taper angle criterion and the blue and green curves represent the core taper angle profiles of "abrupt tapers" and "Gentle tapers", respectively.

strips the LP_{02} cladding mode so that the measured output power corresponds to the LP_{01} mode.

2.1.4 Azimuthal symmetry

If fiber tapers are axisymmetric, the fundamental mode can couple only to modes with the same azimuthal symmetry, i.e. to the higher-order LP_{0m} cladding modes. As we are principally concerned with minimizing loss from the fundamental mode, it is intuitive that coupling will be predominantly to the higher order mode with a propagation constant closest to that of the fundamental mode, i.e. to the LP_{02} mode.

For nonaxisymmetric fibre tapers, or bent or kinked tapers, the fundamental mode will couple, in general, to the higher-order modes with the nearest propagation constant to the fundamental mode, i.e. to the LP_{11} mode.

2.2 Fabrication

2.2.1 Hydrogen flame heating and stretching technique

As illustrated in Fig. 2.4, the gentle tapers are fabricated by using a heating and stretching technique [9, 40]. A section of SMF is stretched by using two linear translation stages with submicron precision and its middle region is jacket-off. A small region of the jacket-off fiber is heated by a hydrogen gas flame with millimeter dimension. The small flame is scanned over a length of several centimeters along the fiber. After a pre-heating process, the fiber is elongated while the scanning range of the flame is increasing. The pulling speed of the translation stages, the scanning speed and the scanning range of the flame are accurately controlled by a computer. The slow stretching technique leads to fiber tapers with gentle slopes in the down- and up-taper regions and long uniform waist region. Figure 2.5(a) presents representative camera picture of fiber taper in its waist range and its cladding diameter curve along the whole fiber taper. The total length of fiber taper can reach ∼10cm with a ∼5cm highly uniform waist region.

Compared with gentle fiber tapers, abrupt fiber tapers are fabricated with heating and fast stretching technique [40, 41]. A constant hot-zone approach is used and the

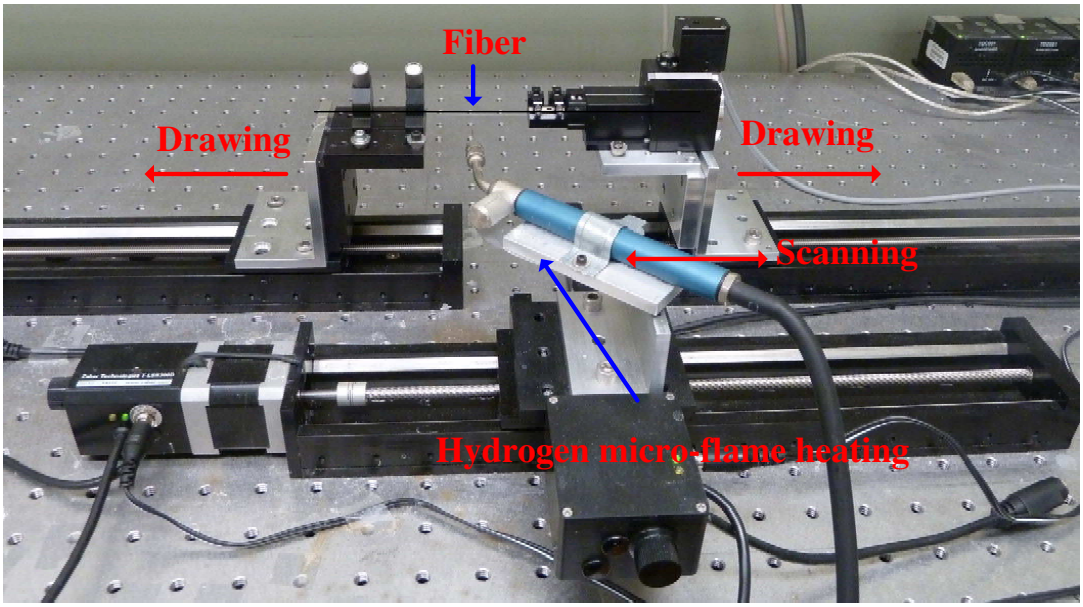

Figure 2.4: Experimental setup for H_2 flame heating and stretching technique.

drawing speed is higher than that of gentle tapers. Hence, the tapers have steep slope and are regarded as non-adiabatic tapers.

A tapered fiber tip is fabricated using the heating and fast stretching approach. The difference is that the drawing speed is sharply changed until the fiber breaks at the waist point. A fiber tip with a parabolic profile is formed due to the surface tension of the fused silica. The tips with steep slopes due to the fast drawing are non-adiabatic. Figure 2.5(b) shows representative camera picture of fiber tip and its cladding diameter curve. For tips with rather gentle slopes, the fundamental mode adapts the shapes according to the change of the waveguide structures. In this case, the propagation process is adiabatic.

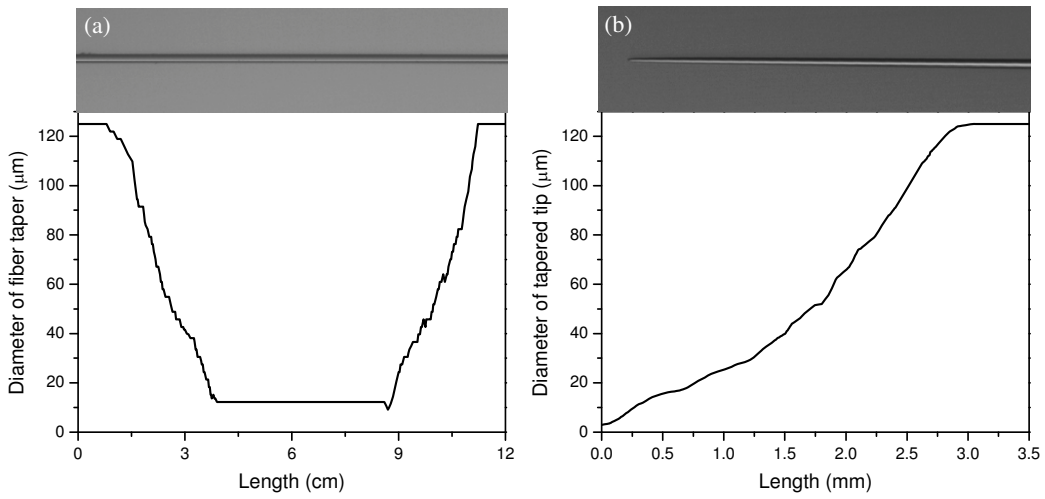

Figure 2.5: (a) Microscope image of a fiber taper in its waist range and its cladding diameter curve along the whole taper. (b) Microscope image of a fiber tip and its cladding diameter curve.

2.2.2 Electrical arc method

An electrical arc method is employed to fabricate abrupt fiber tapers using a fusion splicer, such as Ericsson FSU-995A. A built-in fiber tapering program is chosen and three sets of discharge current and time are customized. Then a section of fiber is fixed in the fiber clamps and the middle jacket-off segment without fiber coating is just under a pair of discharge electrodes. When heat from the electric arc melts the fiber, motorized clamps pull the fiber in opposite directions. The taper has a steep slope and a maximum length of ∼1mm. The length is limited by the speed and travel distance of the fiber clamps. Similarly, an abrupt tapered tip can be fabricated with a fusion splicer. Figure 2.6 presents representative tapered fiber tip and fiber taper.

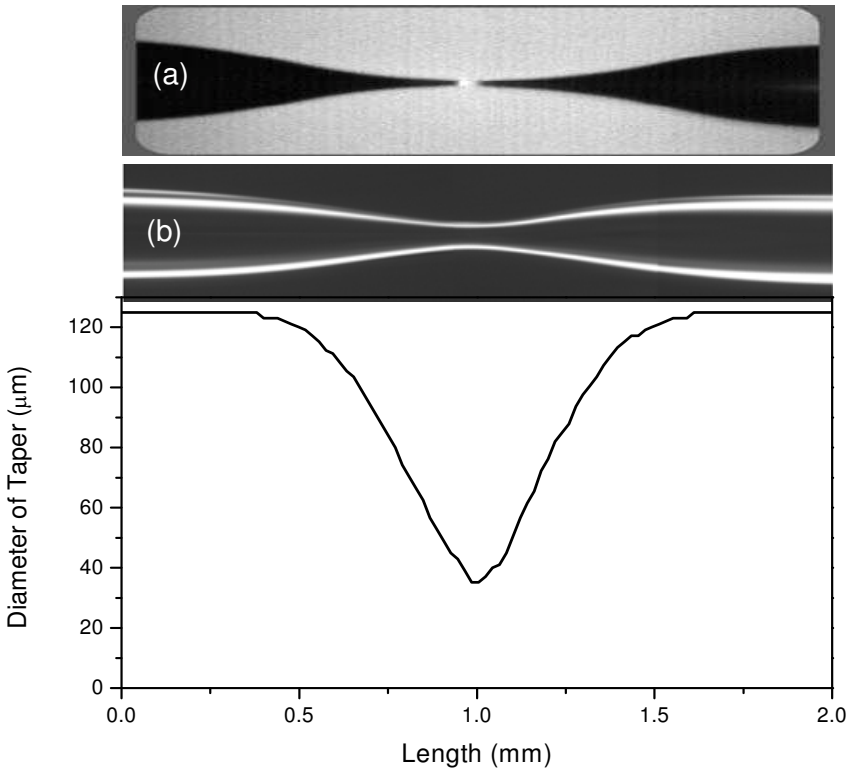

Figure 2.6: (a) Microscope image of a representative tapered fiber tip. (b) Microscope image of fiber taper and its corresponding cladding diameter curve.

2.2.3 Chemical etching method

Chemical etching method fabricates fiber tips with larger taper angle and shorter taper length than those fabricated by the H_2 flame heating and stretching technique. The chemical etching method has advantages over other methods in view of reproducibility, reliability, surface smoothness, symmetry and large taper angle of the tip. Various etching methods including hydrofluoric (HF) acid static etching [42, 43], HF acid dynamic etching [44], and tube etching [45, 46] to produce different configurations of fine optical fiber tips have been proposed. In our experiment, a static chemical etching method under surface

tension is presented in detail.

As illustrated in Fig. 2.7, a section of jacket-off fiber is vertically dipped into the surface of 5% HF acid, which is contained in a Teflon tube. The free surface of HF solution is covered by oil, which efficiently prevents evaporation of HF. Owing to the difference in the surface tension between the etching acid and the fiber, a meniscus is formed between the liquid-solid interface, as shown in Fig. 2.7(b). The general balance of capillary and hydrostatic forces and relation between meniscus rise h and radius of the fiber can be described as [47]

$$h = \left[2\frac{\gamma}{\rho g}(1-\cos\theta_a)\right]^{\frac{1}{2}}\left[1+\left(\frac{\gamma}{\rho g}\right)^{\frac{1}{2}}\frac{1}{r}\right]^{-\frac{1}{2}}, \tag{2.11}$$

where γ is surface tension, ρ density of liquid, θ_a contact angle, r the radius of fiber, g the acceleration due to gravity. Surface tension γ depends on HF concentration and temperature [48]. It is observed that the meniscus rises within 300μm to 400μm along the silica fiber of diameter 125μm depending on the degree of dilution of HF acid. As shown in Fig. 2.7(b)-(e), when the etching time increases, the diameter of fiber in the HF acid gradually decreases and the height of the meniscus also decreases as a function of the remaining tip diameter. Finally, a symmetrical taper is formed at the center of the fiber. In our experiment, the total length of a tapered fiber tip is 0.6mm. The camera picture of a tapered fiber tip and its cladding diameter curve are shown in Fig. 2.8. By adjusting these parameters in Eq. (2.11), the length and surface curvature of fiber tips

can be changed.

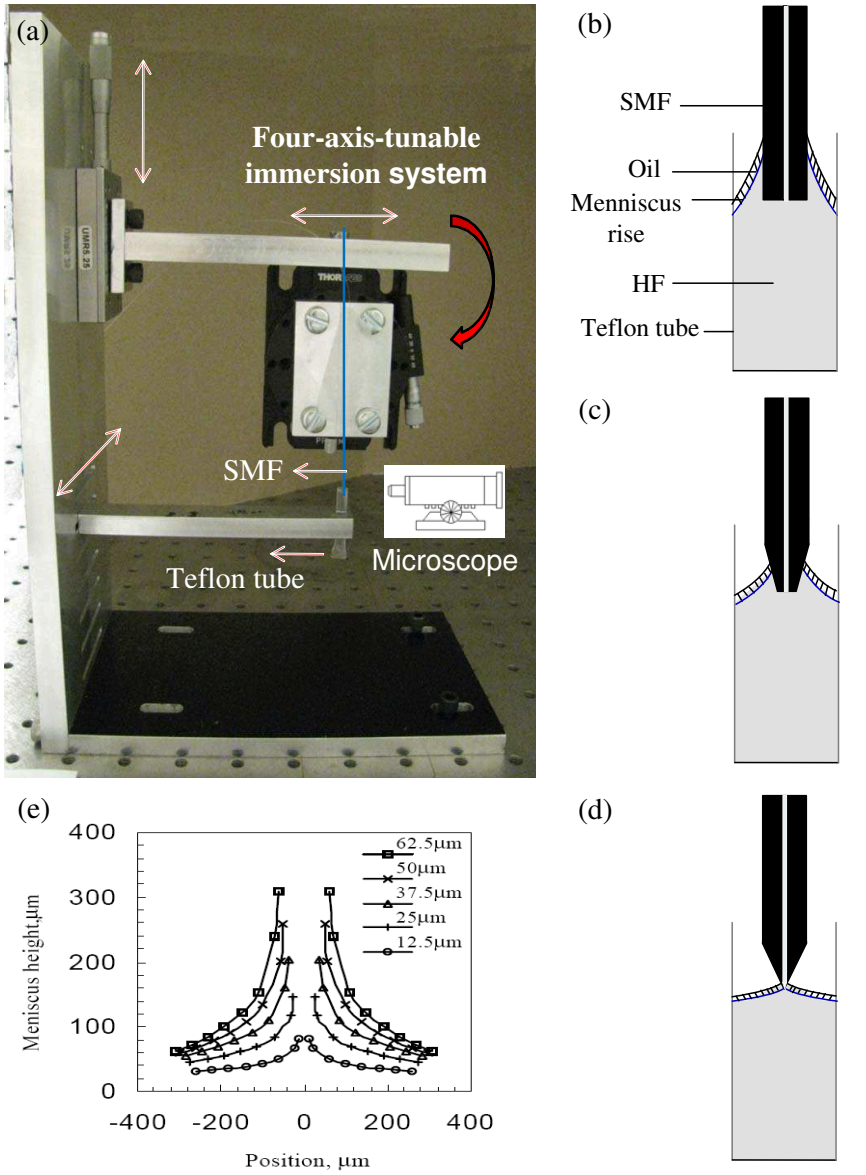

Figure 2.7: (a) Chemical etching setup. (b)-(d) Principle of the tip formation using chemical etching method. The conical shape is obtained by the regular decrease of the meniscus height related to a decrease of the tip diameter. (e) Meniscus profiles for different fiber radii.

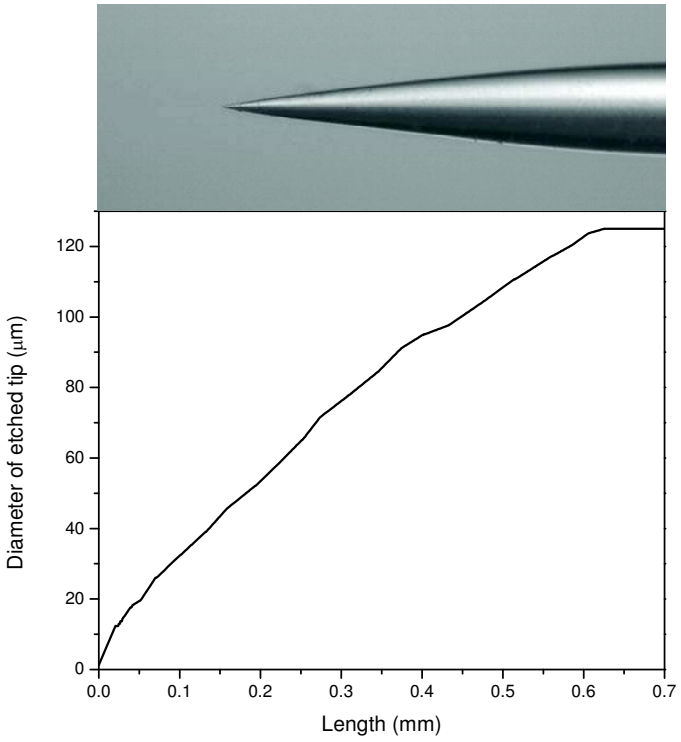

Figure 2.8: Microscope image of a representative tapered fiber tip and its corresponding cladding diameter curve.

Chapter 3

Distributed mode coupling measurement along tapered single-mode fibers with optical frequency-domain reflectometry

This chapter presents a novel method to measure distributed mode coupling along the gentle and abrupt tapers by using an Optical Frequency-domain Reflectometry (OFDR) scheme. Section 3.1 discusses the research motivation. Section 3.2 introduces the theoretical background and operation fundamentals of OFDR technique. Section 3.3 derives the relation between the group index difference and the wavelength shift by autocorrelation data processing in OFDR measurement. In section 3.4, the wavelength shifts between

the fundamental mode and higher-order modes of the gentle tapers and abrupt tapers are clearly displayed on autocorrelation figures. The measured results are compared with the theoretical group index differences.

3.1 Introduction

Tapering is an effective technique for mode conversion from the fundamental mode to higher-order modes in a fiber. When a single-mode fiber (SMF) is tapered to pass the core-to-cladding mode transition point, higher-order modes are generated within this transition region [25]. Mode coupling process along a tapered fiber occurs at the down- and up-taper regions with large taper slopes, while beating, instead of coupling, between the excited local modes occurs at the central quasi-adiabatic uniform waist region. Earlier theoretical works evaluated the mode power evolution along a tapered fiber and gave the delineation criteria for mode coupling [8, 26, 27]. Experimental observations showed the presence of more than two modes in a tapered fiber, which was seen as the power oscillation by varying the external index [27]. The distributed power oscillation along the tapered fiber was measured point-by-point by moving a thin film perturbation along the tapered fiber [26]. Another common method, the cutback measurement, was performed to find the exact transverse spectrum at different positions along the taper [29]. However, this destructive technique did not count the mode coupling continuously.

Recently, OFDR has been used to measure the Rayleigh backscatter spectrum as a function of fiber length, and the use of autocorrelation in the spectral domain has pro-

vided an easily implemented method for characterizing fiber birefringence [49]. Here we use OFDR to characterize single-mode and multimode regions of a tapered fiber and calculate the group index difference between the fundamental mode and higher-order modes of the taper by using autocorrelation data processing. The energy re-distribution along the tapered fiber is measured through Rayleigh backscatter amplitude versus distance with a $\sim$13μm resolution over the whole taper region. The wavelength shifts between the fundamental mode and higher-order modes of the taper are theoretically derived in OFDR scheme and clearly displayed on an autocorrelation figure. The average group index differences between the fundamental mode and higher-order modes within a $\sim$2cm region along the gentle and abrupt tapers are measured in the experiments. We found that, in the case of the gentle tapers, the coupling lengths are the same as their geometric structures, and the measured group index differences and theoretical value match well. While in the case of the abrupt tapers, the mode coupling processes exist in longer segments than their geometric structures.

3.2 Principle

3.2.1 Rayleigh scattering

Light scattering occurs as a consequence of fluctuations in the optical properties of a material medium. As long as the optical properties of the material system are unmodified by the presence of the incident light beam, the scattering process is said to be spontaneous.

Conversely, if the intensity of incident light is sufficiently large to modify the properties of the medium, then the regime becomes stimulated. Four types of spontaneous light scattering are Rayleigh, Brillouin, Raman and Rayleigh wing [50]. Rayleigh scattering (or Rayleigh-center scattering) is the scattering of light from nonpropagating density fluctuations, which in turn causes random microscopic variations in the refractive index. Rayleigh scattering is known as a quasielastic scattering process, because the frequencies of incident and scattered light are equal.

Rayleigh scattering in fiber arises from local microscopic fluctuations in density, which is produced when optical fibers are manufactured. Rayleigh scattering occurs when the size of the density fluctuation (fiber defect) is less than one-tenth of the operating wavelength λ [51]. The scattered intensity is proportional to the fourth power of the wavelength (λ^{-4}) and the intrinsic Rayleigh scattering loss of silica fibers is expressed as

$$\alpha_s = \frac{C}{\lambda^4}, \tag{3.1}$$

where the constant C is in the range of 0.7–0.9 (dB/km)μm^4, depending on the constituents of the fiber core [52].

There are two general ways to get energy losses in fiber: Rayleigh scattering and material absorption. The total attenuation coefficient α (with units of dB/km) is given by

$$\alpha = \alpha_s + \alpha_a. \tag{3.2}$$

At the wavelength of λ=1550nm, α_s=0.12–0.16dB/km and $\alpha\approx$0.2dB/km, indicating that fiber loss is dominated by Rayleigh scattering near 1550nm [52].

Owing to these fiber losses, the optical power decreases exponentially as a function of the propagating distance z,

$$P(z) = P_0 e^{(-\alpha z)}, \tag{3.3}$$

where P_0 is the power launched at the input end of a fiber, $P(z)$ is the transmitted power at distance z and α with units of km^{-1}. It is customary to express α in units of dB/km by using the relation

$$\alpha(dB/km) = -\frac{10}{z}\log_{10}(\frac{P(z)}{P_0}) \approx 4.343\alpha. \tag{3.4}$$

Rayleigh scattering radiates in all directions and the power of backscattered light $\mathrm{d}P_{bs}(z)$ is expressed as a function of the propagating distance z [53],

$$dP_{bs}(z) = S_b \alpha_s P_0 e^{-2\alpha z} dz, \tag{3.5}$$

where the backscattering capture coefficient S_b describes the fraction of the total Rayleigh-scattered power that gets captured in the fiber and propagates in the backwards direction and is given by [54]

$$S_b = \frac{1}{m}(\frac{NA}{n_{co}})^2, \tag{3.6}$$

where NA=$\sqrt{n_{co}^2 - n_{cl}^2}$ is the numerical aperture, n_{co} and n_{cl} are the refractive indices of

the core and cladding, respectively. Coefficient m depends on the refractive index profile and has a typical value of 4.55 for SMFs [55].

Light travels inside the optical fiber at the velocity $\nu_g = \frac{c}{n_g}$, where c is the light speed in vacuum and n_g is the group index for the fiber. Using the relation $2z = \nu_g t$, Eq. (3.5) is rewritten into the form

$$dP_{bs}(t) = \frac{S_b \alpha_s P_0 \nu_g}{2} e^{-\alpha \nu_g t} dt. \tag{3.7}$$

3.2.2 Fundamentals of OFDR operation

OFDR is one of the most distinguished techniques for distributed sensing [56]. The principle of operation is to measure the characteristics of various spatially-distributed Rayleigh backscattering. Based on swept-wavelength homodyne interferometry [57–59], an OFDR operates by splitting a light from a tunable laser source (TLS) and sending through sensing and reference arms of an interferometer and recombined at an optical detector. The interference fringes, generated as the laser frequency is tuned, are related to the optical amplitude and phase response of the reflected light. The reflected light is produced by two mechanisms: Fresnel reflection that occurs as light passes into a medium having a different index of refraction, and Rayleigh scattering which results from nonpropagating density fluctuations and in turn causes random microscopic variations in the refractive index.

In an OFDR system, we adopt the polarization diversity detection technique and a

trigger interferometer configuration. First, a general problem with coherent measurements is the polarization dependence. The state of polarization (SOP) of the reflected light with respect to the reference light influences the intensity of the measured signal. If the SOP of the reference and the test signals are orthogonal at the detector, the interference will be completely cancelled [60]. In order to avoid this dependence, the use of a polarization diversity receiver was proposed [61]. In this method, the sum of the reference and test signal is split into two orthogonal polarization states, detected by two photodetectors (PDs). The intensities of both detected light signals are summed and result in a measured signal that is independent of the polarization. Secondly, another general problem is nonlinearity in the optical frequency modulation. When explaining operational principles of OFDR, we assumed that the optical frequency sweep is perfectly linear in time. However, the available lasers exhibit in practice fluctuations in their optical frequency tuning rate. Due to these nonlinear tuning characteristics, sampling of the interference signal with a constant spacing in time gives rise to a non-uniform sampling in optical frequency which, in turn, degrades the spatial resolution of the OFDR measurement. It is well known that this problem can be avoided by sampling the interference signal at equidistant instantaneous optical frequency points rather than equally spaced time intervals [58]. The most common approach is known as frequency sampling. The time varying optical frequency is simultaneously monitored by means of an auxiliary Mach-Zehnder interferometer (MZI). The zero crossing points of the signal at the detector output of the auxiliary interferometer are used to generate trigger pulses which

are then used as an external sampling clock on the test interferometer [56, 59, 62, 63].

The achievable spatial resolution and measurement range of OFDR are related to the coherence length of the tunable laser, the laser frequency sweep range as well as the sweep speed. The spatial resolution of the measurement, Δz, is directly determined by the spectral bandwidth of the scan range according to [56]

$$\Delta z = \frac{\lambda_1 \lambda_2}{2 n_g \Delta\lambda}, \tag{3.8}$$

with scanning wavelength range $\Delta\lambda$=$|\lambda_1 - \lambda_2|$, λ_1, $lambda_2$ are the starting and the stopping wavelengths, and the group index of the fiber n_g=1.48. This resolution can be corrupted by environmental noise and insufficiently linear laser tuning. The maximum length of the FUT, L_{max}, is determined by the differential delay in the trigger interferometer using the Nyquist sampling criteria by [56]

$$L_{max} = \frac{c\tau_g}{4 n_g}, \tag{3.9}$$

where c is the speed of light in a vacuum, τ_g is the group delay introduced by the trigger interferometer and the factor of four is due to the sampling theorem and the double-pass nature of the measurement interferometer. Since the currently available tunable lasers depart from perfect coherence and produce phase noise that prevents a wide frequency sweep range, OFDR is predominantly operated over intermediate length (tens to hundreds of meters) with sub-centimeter resolution [61].

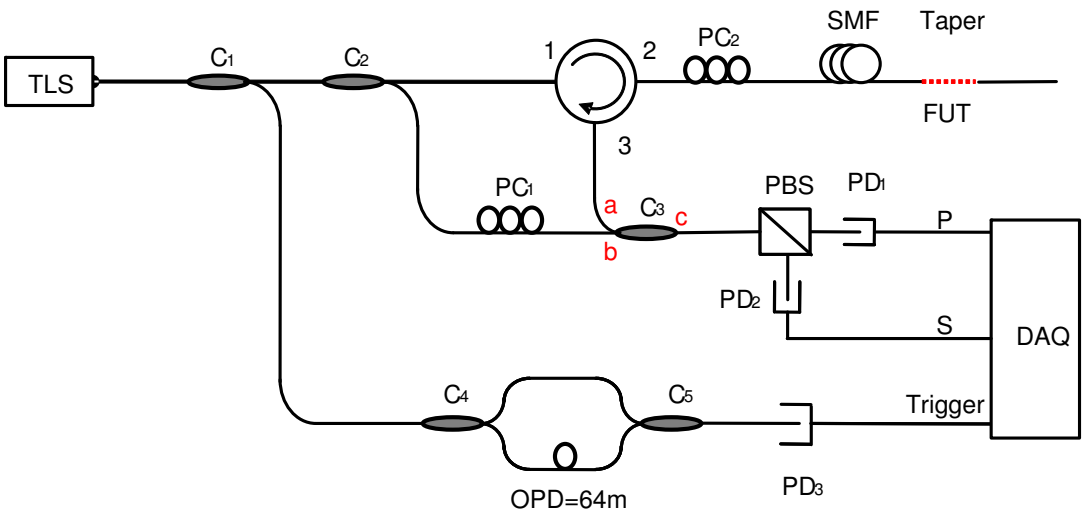

Figure 3.1: Schematic setup of OFDR system. TLS: tunable light source; C_1: 99 : 1 coupler; C_2, C_3, C_4, C_5: 50 : 50 couplers; PC: polarization controller; PBS: polarization beam splitter; PD: photodetector; OPD: optical path difference; DAQ: data acquisition; FUT: fiber under test.

A schematic setup of OFDR system is shown in Fig. 3.1. Rayleigh backscatter signal of the fiber taper is monitored and its complex Fourier transform is carried out to obtain OTDR-like curve along the taper length. A polarization-independent signal is obtained by calculating the vector sum of the p- and s-components of the detected signal. The amplitude of the OTDR-like curve as a function of distance indicates the energy re-distribution over the whole taper region. Then the wavelength shift can be calculated by applying an appropriate window within the OTDR-like curve of the taper, calculating its spectrum response through inverse Fourier transform data processing and doing the autocorrelation calculation.

3.2.3 Dispersion

Chromatic dispersion occurs because the refractive index of silica changes with the optical frequency ω. The origin is related to the characteristic resonance frequencies at which the material absorbs the electromagnetic radiation. Far from the medium resonances, the refractive index $n(\omega)$ is well approximated by the Sellmeirer equation [64]

$$n^2(\omega) = 1 + \sum_{j=1}^{M} \frac{B_j \omega_j^2}{\omega_j^2 - \omega^2}, \tag{3.10}$$

where ω_j is the resonance frequency and B_j is the strength of jth resonance. The sum in Eq. (3.10) extends over all material resonances that contribute to the frequency range of interest. In the case of optical fibers, the parameters B_j and ω_j are obtained experimentally by fitting the measured dispersion curves [65] to Eq. (3.10) with M=3 and depend on the core constituents [66]. For bulk-fused silica, these parameters are given in [67].

Fiber dispersion plays a critical role in propagation of short optical pulses because different spectral components associated with the pulse travel at different speeds given by $\frac{c}{n(\omega)}$. Mathematically, the effects of fiber dispersion are accounted for by expanding the mode-propagation constant β in a Taylor series about the frequency ω_0 at which the pulse spectrum is centered:

$$\beta(\omega) = n(\omega)\frac{\omega}{c} = \beta_0 + \beta_1(\omega - \omega_0) + \frac{1}{2}\beta_2(\omega - \omega_0)^2 + \ldots, \tag{3.11}$$

where

$$\beta_m = \left(\frac{d^m\beta}{d\omega^m}\right)_{\omega=\omega_0} \ (m = 0, 1, 2, \ldots). \tag{3.12}$$

υ_g is the group velocity, defined as

$$\upsilon_g = \frac{1}{\beta_1} = \frac{c}{n_g} = \frac{c}{n + \omega\frac{dn}{d\omega}}, \tag{3.13}$$

where n_g is the group index. Figure 3.2 shows how refractive index n and the group index n_g changes with wavelength λ for fused silica. As seen there, n has a value of about 1.46 in the visible region, and this value decreases by 1% in the wavelength region near 1.5μm. The dispersive behavior of actual glass fibers deviates from that shown in the figure for the following two reasons. First, the fiber core may have small amounts of dopants such as GeO_2 and P_2O_5. Eq. (3.10) in that case should be used with parameters appropriate to the amount of doping levels [66]. Second, because of dielectric waveguiding, the effective mode index is slightly lower than the material index $n(\omega)$ of the core, reduction itself being ω dependent [64, 66, 68]. This results in a waveguide contribution that must be added to the material contribution to obtain the total dispersion.

Even an SMF is not truly single mode because it can support two degenerate modes that are polarized in two orthogonal directions. Under ideal conditions (perfect cylindrical symmetry and a stress-free fiber), a mode excited with its polarization in the x direction would not couple to the mode with the orthogonal y-polarization state. In real

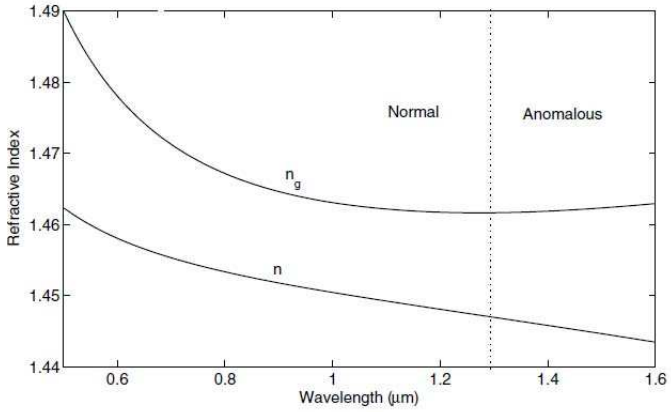

Figure 3.2: Variation of refractive index n and group index n_g with wavelength for fused silica.

fibers, small departures from cylindrical symmetry, occurring because of random variations in the core shape along the fiber length, result in a mixing of the two polarization states by breaking the mode degeneracy. The stress-induced anisotropy can also break this degeneracy. Mathematically, the mode propagation constant β becomes slightly different for the modes polarized in the x and y directions. This property is referred to as modal birefringence. The strength of modal birefringence is defined by a dimensionless parameter [69]

$$B_m = \frac{|\beta_x - \beta_y|}{k_0} = |n_x - n_y|, \tag{3.14}$$

where n_x and n_y are the modal refractive indices for the two orthogonally polarized states. For a given value of B_m, the two modes exchange their powers in a periodic fashion as

they propagate inside the fiber with the period [69]

$$L_B = \frac{2\pi}{|\beta_x - \beta_y|} = \frac{\lambda}{B_m}, \tag{3.15}$$

where L_B is the beat length. The axis along which the mode index is smaller is called the fast axis because the group velocity is larger for light propagating in that direction. For the same reason, the axis with the larger mode index is called the slow axis. In standard optical fibers, B_m is not constant along the fiber but changes randomly because of fluctuations in the core shape and anisotropic stress. As a result, light launched into the fiber with a fixed state of polarization changes its polarization in a random fashion.

3.3 Principle of mode coupling measurement in fiber tapers with OFDR

3.3.1 Group index difference measurement with OFDR

As shown in Fig. 3.1, the tunable laser has an angular frequency of $\omega(t)$ and a phase of $\varphi(t)$. The input port of the coupler C_2 is regarded as the original point of $z = 0$. Its electric field is expressed as

$$E_{z=0}(t) = E_0(t)\, e^{i\varphi(t)}. \tag{3.16}$$

The electric field at port b of the coupler C_3 is expressed as

$$E_b(t) = \frac{A_b}{\sqrt{2}} E_0 \left(t - \frac{z_b}{V}\right) e^{i\varphi\left(t-\frac{z_b}{V}\right)-\alpha z_b}, \tag{3.17}$$

where z_b is the length from output port of C_2 to the input port b of C_3. $V = \frac{c}{n_g}$ is the group velocity inside the fiber, n_g is the group index and c is the speed of light in vacuum. α is the decay coefficient. A_b represents a complex number describing the phase shift as the light goes through the arm of the upper MZI.

The electric field arriving at position z' along the fiber under test (FUT) is written as

$$E_{z'}(t) = \frac{A_{z'}}{\sqrt{2}} E_0 \left(t - \frac{z'}{V}\right) e^{i\varphi\left(t-\frac{z'}{V}\right)-\alpha z'}. \tag{3.18}$$

Rayleigh backscatter going back via the circulator to port a of the coupler C_3 is a sum of all points along the FUT, which is given by

$$E_a(t) = \frac{A_a}{\sqrt{2}} \sum_{z'} \left[e^{-\alpha(2z'-z_a)} r(z') E_0 \left(t - \frac{2z'-z_a}{V}\right) e^{i\varphi\left(t-\frac{2z'-z_a}{V}\right)} \right]. \tag{3.19}$$

where $r(z')$ is Rayleigh reflection coefficient and A_a describes the phase shift as the light goes through these components. z_a is the location of port a with respect to the tunable laser location considering all the lead fiber in the system.

The electric field at output port c of the coupler C_3 is shown as

$$E_c(t) = \frac{A_a}{2}\sum_{z'}\left[e^{-\alpha(2z'-z_a)}r(z')\,E_0\left(t-\frac{2z'-z_a}{V}\right)e^{i\varphi\left(t-\frac{2z'-z_a}{V}\right)}\right] + i\frac{A_b}{2}E_0\left(t-\frac{z_b}{V}\right)e^{i\varphi\left(t-\frac{z_b}{V}\right)-\alpha z_b}. \tag{3.20}$$

The signal passes through the PBS and is split into p- and s- components of the PBS as follows,

$$E_P(t) = \hat{P}\frac{T_P e^{i\Phi_P}}{2}\left\{A_a\sum_{z'}\left[e^{-\alpha(2z'-z_a)}r_P(z')\,E_0\left(t-\frac{2z'-z_a}{V}\right)e^{i\varphi\left(t-\frac{2z'-z_a}{V}\right)}\right] + iA_bE_0\left(t-\frac{z_b}{V}\right)e^{i\varphi\left(t-\frac{z_b}{V}\right)-\alpha z_b}\right\}, \tag{3.21}$$

$$E_S(t) = \hat{S}\frac{T_S e^{i\Phi_S}}{2}\left\{A_a\sum_{z'}\left[e^{-\alpha(2z'-z_a)}r_S(z')\,E_0\left(t-\frac{2z'-z_a}{V}\right)e^{i\varphi\left(t-\frac{2z'-z_a}{V}\right)}\right] + iA_bE_0\left(t-\frac{z_b}{V}\right)e^{i\varphi\left(t-\frac{z_b}{V}\right)-\alpha z_b}\right\}, \tag{3.22}$$

where $r_P(z')$ and $r_S(z')$ are Rayleigh reflection coefficient at p- and s-axes of the PBS, respectively. Φ_P and Φ_S describe the phase shift as the light goes through the p- and s-axes of the PBS, respectively. T_P and T_S are the split portion on the PBS axes.

Assuming no cross-talk condition, we force the condition $z_a = z_b = \ell$. Then the AC

current at p-detector is expressed as

$$I_{AC}^{P}(t) = \frac{T_P^2 A_a A_b^*}{4} \sum_{z'} \left\{ e^{-2\alpha(z'+\ell)} r_P(z') E_0\left(t - \frac{2z'-\ell}{V}\right) E_0^*\left(t - \frac{\ell}{V}\right) \times e^{i\left[\varphi\left(t-\frac{2z'-\ell}{V}\right) - \varphi\left(t-\frac{\ell}{V}\right) - \frac{\pi}{2}\right]} \right\} + c.c.. \tag{3.23}$$

We have the frequency of tunable laser $\omega(t) = \Omega t + \omega_0$, where Ω is a constant sweep rate of tunable laser and ω_0 is the initial angular frequency. Then the phase $\varphi(t)$ is written as

$$\varphi(t) = \int_0^t \omega(t)\, dt = \frac{1}{2}\Omega t^2 + \omega_0 t + \varphi_0, \tag{3.24}$$

where φ_0 is the initial phase. We have

$$\varphi\left(t - \frac{\ell}{V}\right) - \varphi\left(t - \frac{2z'+\ell}{V}\right) = \Omega\frac{2z'}{V}t + \frac{2z'}{V}\left(\omega_0 - \Omega\frac{z'+\ell}{V}\right). \tag{3.25}$$

Then Eq. (3.23) is reduced to

$$I_{AC}^{P}(t) = \frac{T_P^2 A_a A_b^*}{4} \sum_{z'} \left\{ e^{-2\alpha(z'+\ell)} r_P(z') E_0\left(t - \frac{2z'+\ell}{V}\right) E_0^*\left(t - \frac{\ell}{V}\right) \times e^{-i\left[\Omega\frac{2z'}{V}t + \frac{2z'}{V}\left(\omega_0 - \Omega\frac{z'+\ell}{V}\right) + \frac{\pi}{2}\right]} \right\} + c.c.. \tag{3.26}$$

We assume that the electric field amplitude is stable, leading to $E_0\left(t - \frac{2z'+\ell}{V}\right) \approx E_0(t)$

and $E_0^*\left(t-\frac{\ell}{V}\right)\approx E_0^*(t)$. The measured p-detector signal is

$$\begin{aligned}
I_{AC}^P(t) =& \sum_{z'}\Bigg\{ |r_P(z')|\,|m_P(t)|\,e^{-2\alpha(z'+\ell)} \\
&\times e^{-i\left[\omega\frac{2z'}{V}t+\frac{2z'}{V}\left(\omega_0-\Omega\frac{z'+\ell}{V}\right)+\theta_P(t)+\theta_{r_P}(z')+\frac{\pi}{2}\right]}\Bigg\}+c.c. \\
=&2\sum_{z'}\Bigg\{ |r_P(z')|\,|m_P(t)|\,e^{-2\alpha(z'+\ell)} \\
&\times\cos\left[\Omega\frac{2z'}{V}t+\frac{2z'}{V}\left(\omega_0-\Omega\frac{z'+\ell}{V}\right)+\theta_P(t)+\theta_{r_P}(z')+\frac{\pi}{2}\right]\Bigg\} \\
=&\sum_{z'} m_P(t,z')\cos\left[\Omega\frac{2z'}{V}t+\theta_P(t)+\varphi_P(z')\right],
\end{aligned} \tag{3.27}$$

where

$$r_P(z')=|r_P(z')|\,e^{i\theta_{r_P}(z')}, \tag{3.28}$$

$$m_P(t)=|m_P(t)|\,e^{i\theta_P(t)}=\frac{T_P^2A_aA_b^*}{4}\,|E_0(t)|^2\,, \tag{3.29}$$

$$m_P(t,z')=2\,|r_P(z')|\,|m_P(t)|\,e^{-2\alpha(z'+\ell)}, \tag{3.30}$$

$$\varphi_P(z')=\frac{2z'}{V}\left(\omega_0-\Omega\frac{z'+\ell}{V}\right)+\theta_{r_P}(z')+\frac{\pi}{2}. \tag{3.31}$$

By using the slowly-varying-amplitude approximation, we have $m_P(t,z')\approx m_P(z')$, and

Eq.(3.27) is reduced to

$$I_{AC}^{P}(t) \approx \sum_{z'} m_P(z') \cos\left[\Omega \frac{2z'}{V} t + \varphi_P(z')\right]. \tag{3.32}$$

By doing the complex Fourier transform, we obtain

$$\begin{aligned} I_{AC}^{P}(\omega) &\approx \frac{\sqrt{2}\pi}{2} \sum_{z'} m_P(z') \left[e^{i\varphi_P(z')} \delta\left(\omega - \frac{2z'}{V}\Omega\right) + e^{-i\varphi_P(z')} \delta\left(\omega + \frac{2z'}{V}\Omega\right)\right] \\ &= \frac{\sqrt{2}\pi}{2} \sum_{z'} m_P(z') e^{i\varphi_P(z')} \delta\left(\omega - \frac{2z'}{V}\Omega\right). \end{aligned} \tag{3.33}$$

Since $\omega > 0$, we can ignore the second term of Eq. (3.33). For simplicity, we assume

$$I_{AC}^{P}(\omega) = \sum_{z'} \kappa_P(z') \delta\left(\omega - \frac{2z'}{V}\Omega\right), \tag{3.34}$$

where $\kappa_P(z') = \frac{\sqrt{2}\pi}{2} m_P(z') e^{i\varphi_P(z')}$ and is related to local Rayleigh backscatter strength.

The derivations of the measured s-detector signal and its complex Fourier transform are similar to the above.

A polarization-independent signal is obtained by calculating the vector sum of the p- and s-components and could be given by

$$I(t) = \sum_{z'} m(z') \cos\left[\Omega \frac{2z'}{V} t + \varphi(z')\right], \tag{3.35}$$

and

$$I(\omega) = \sum_{z'} \kappa(z')\,\delta\left(\omega - \frac{2z'}{V}\Omega\right). \tag{3.36}$$

The definitions of $m(z')$ and $\kappa(z')$ are similar to that of $m_P(z')$ and $\kappa_P(z')$, respectively.

In the previous derivation, we assume that there is only one mode with group index n_g and its corresponding group velocity V inside the fiber. We obtain a final time signal $I(t)$ and its complex Fourier transform $I(\omega)$.

3.3.2 Principle of mode coupling measurement in fiber tapers with OFDR

The fundamental mode of axisymmetric tapers is only coupled to modes with the same azimuthal symmetry, i.e. to the higher-order linearly polarized (LP) modes, LP_{0m} modes. In the case of non-axisymmetric tapers, the energy of the fundamental mode will be predominantly coupled to $LP_{\upsilon m}$ modes, which have the nearest propagation constant to the fundamental mode, i.e. to the LP_{11} and LP_{02} modes. These modes propagate along the tapered fiber with different effective refractive indices. In the material, e.g. in the fiber, the wavelength of a mode is related to both its frequency and refractive index, which is shown as

$$\Delta\lambda_i = \frac{c}{n_i v_i}, \tag{3.37}$$

where λ_i, v_i, and n_i are the wavelength, frequency, and refractive index for the ith mode, respectively, inside the fiber. c is the velocity of light in vacuum. The relation between the wavelength shift and the refractive index difference at the position z of difference modes is obtained by

$$\Delta\lambda_{ij} = |\lambda_i - \lambda_j| = \left|\frac{c}{n_i v_i} - \frac{c}{n_j v_j}\right| = \frac{c}{v_i}\left|\frac{1}{n_i} - \frac{1}{n_j}\right| \approx \frac{c}{v_i n_i^2}\Delta n_{ij} \approx \frac{\lambda_i}{n_i}\Delta n_{ij}, \tag{3.38}$$

where $v_i = v_j$, $n_i \approx n_j$, $\Delta n_{ij} = |n_i - n_j|$. From Eq. (3.38), we have

$$\Delta n_{ij} = \frac{n_i}{\lambda_i}\Delta\lambda_{ij}. \tag{3.39}$$

Because a swept-wavelength OFDR scheme is used, the dispersion of the guided mode should be taken into account. Δn_{ij} should be replaced with the differential modal group index Δm_{ij} [70], and Eq. (3.39) is revised as

$$\Delta m_{ij} = \frac{n_{gi}}{\lambda_i}\Delta\lambda_{ij}. \tag{3.40}$$

with

$$\Delta m_{ij} = |n_{gi} - n_{gj}|\,\Delta n_{ij} - \lambda\frac{\partial\Delta n_{ij}}{\partial\lambda}. \tag{3.41}$$

where n_{gi} is the group index for the ith mode. Therefore, the group index difference between the fundamental mode and the higher-order mode of a segment of a tapered fiber is obtained by measuring the wavelength shift, which can be realized by utilizing

an OFDR scheme.

As mentioned above, the modes propagate and reflect in the tapered fiber with different group velocities due to different group indices. Then different group velocities result in different distance signals in the OTDR-like curves along the taper length. In the case of tapers, we assume that there are two modes with group indices n_{g1} and n_{g2}, respectively. Their corresponding group velocities are V_1 and V_2, respectively. Eq. (3.27) will include three components,

$$I(\omega) = \sum_{z'} \left\{ \alpha_1(z')\,\kappa(z')\,\delta\left(\omega - \frac{2z'}{V_1}\Omega\right) + \alpha_2(z')\,\kappa(z')\,\delta\left(\omega - \frac{2z'}{V_2}\Omega\right) + \alpha_{12}(z')\,\kappa(z')\,\delta\left[\omega - z'\Omega\left(\frac{1}{V_1} + \frac{1}{V_2}\right)\right] \right\}, \tag{3.42}$$

where $\alpha_i(z')$ is the proportion coefficient of ith mode and $\alpha_{ij}(z')$ is the proportion coefficient of mode coupling between ith mode and jth mode. These three proportion coefficients satisfy $\alpha_1(z') + \alpha_2(z') + \alpha_{12}(z') = 1$, $\forall z'$. $\kappa(z')$ is directly related to local Rayleigh backscatter strength.

Since $\delta(\omega - bz') = \frac{1}{|b|}\delta\left(z' - \frac{\omega}{b}\right)$, we have

$$I(\omega) = \sum_{z'} \left\{ \frac{V_1}{2\Omega}\alpha_1(z')\,\kappa(z')\,\delta\left(z' - \frac{\omega V_1}{2\Omega}\right) + \frac{V_2}{2\Omega}\alpha_2(z')\,\kappa(z')\,\delta\left(z' - \frac{\omega V_2}{2\Omega}\right) + \frac{V_1 V_2}{\Omega(V_1 + V_2)}\alpha_{12}(z')\,\kappa(z')\,\delta\left[z' - \frac{\omega V_1 V_2}{\Omega(V_1 + V_2)}\right] \right\}. \tag{3.43}$$

Then it is carried out to obtain OTDR-like curve along the taper length, which is

expressed as

$$\begin{aligned} S(\bar{z}) =& I\left(\frac{2\omega\bar{z}}{V_1}\right) \\ =& \sum_{z'}\left[\frac{V_1}{2\Omega}a_1(z')\,\kappa(z')\,\delta(z'-\bar{z}) + \frac{V_2}{2\Omega}a_2(z')\,\kappa(z')\,\delta\left(z'-\bar{z}\frac{V_1}{V_2}\right)\right. \\ &\left. + \frac{V_1 V_2}{\Omega(V_1+V_2)}a_{12}(z')\,\kappa(z')\,\delta\left(z'-\bar{z}\frac{2V_2}{V_1+V_2}\right)\right] \\ =& \frac{V_1}{2\Omega}a_1(\bar{z})\,\kappa(\bar{z}) + \frac{V_2}{2\Omega}a_2\left(\bar{z}\frac{V_2}{V_1}\right)\kappa\left(\bar{z}\frac{V_2}{V_1}\right) \\ &+ \frac{V_1 V_2}{\Omega(V_1+V_2)}a_{12}\left(\bar{z}\frac{2V_2}{(V_1+V_2)}\right)\kappa\left(\bar{z}\frac{2V_2}{V_1+V_2}\right), \end{aligned} \tag{3.44}$$

where $\bar{z} = \frac{V_1}{2\Omega}$.

An appropriate window with a width of Δz is applied at z' the position along the OTDR-like curve and its spectrum response is obtained through inverse Fourier transform data processing, as follows,

$$\begin{aligned} I_{\Delta z}(\omega, z') =& \left|\sqrt{2\pi}\int_{z'}^{z'+\Delta z} e^{i\omega z}S(z)\,dz\right| \\ =& \left|\sqrt{2\pi}\int_{z'}^{z'+\Delta z} e^{i\omega z}\left[\frac{V_1}{2\Omega}a_1(z)\,\kappa(z) + \frac{V_2}{2\Omega}a_2\left(z\frac{V_2}{V_1}\right)\kappa\left(z\frac{V_2}{V_1}\right)\right.\right. \\ &\left.\left. + \frac{V_1 V_2}{\Omega(V_1+V_2)}a_{12}\left(z\frac{2V_2}{V_1+V_2}\right)\kappa\left(z\frac{2V_2}{V_1+V_2}\right)\right]dz\right|. \end{aligned} \tag{3.45}$$

Let $K_j(\omega, z', \Delta z) = \sqrt{2\pi}\int_{z'}^{z'+\Delta z} e^{i\omega z}a_j(z)\,\kappa(z)\,dz$ and the second term in Eq. (3.45) is

expressed as

$$\begin{aligned}
&\sqrt{2\pi}\int_{z'}^{z'+\Delta z} e^{i\omega z} a_2\left(z\frac{V_2}{V_1}\right)\kappa\left(z\frac{V_2}{V_1}\right)dz \\
=&\frac{V_1}{V_2}\sqrt{2\pi}\int_{\frac{V_2}{V_1}z'}^{\frac{V_2}{V_1}z'+\Delta z} e^{i\omega\frac{V_1}{V_2}y} a_2(y)\,\kappa(y)\,dy \quad \left(\text{let } y = z\frac{V_2}{V_1}\right) \\
=&\frac{V_1}{V_2}K_2\left(\omega\frac{V_1}{V_2}, z'\frac{V_2}{V_1}, \Delta z\frac{V_2}{V_1}\right).
\end{aligned} \tag{3.46}$$

And the third term in Eq. (3.45) is given by

$$\begin{aligned}
&\sqrt{2\pi}\int_{z'}^{z'+\Delta z} e^{i\omega z} a_{12}\left(z\frac{2\,V_2}{V_1+V_2}\right)\kappa\left(z\frac{2\,V_2}{V_1+V_2}\right) \\
=&\frac{V_1+V_2}{2\,V_2}\sqrt{2\pi}\int_{\frac{2\,V_2}{V_1+V_2}z'}^{\frac{2\,V_2}{V_1+V_2}(z'+\Delta z)} e^{i\omega\frac{V_1+V_2}{2\,V_2}y} a_{12}(y)\,\kappa(y)\,dy \quad \left(\text{let } y = z\frac{2\,V_2}{V_1+V_2}\right) \\
=&\frac{V_1+V_2}{2\,V_2}K_{12}\left(\omega\frac{V_1+V_2}{2\,V_2}, z'\frac{2\,V_2}{V_1+V_2}, \Delta z\frac{2\,V_2}{V_1+V_2}\right).
\end{aligned} \tag{3.47}$$

We have

$$\begin{aligned}
I_{\Delta z}(\omega, z') =&\frac{V_1}{2\Omega}\Big| K_1(\omega, z', \Delta z) + K_2\left(\omega+\Delta\omega_{12}, z'\frac{V_2}{V_1}, \Delta z\frac{V_2}{V_1}\right) \\
&+ K_{12}\left(\omega+\frac{\Delta\omega_{12}}{2}, z'\frac{2\,V_2}{V_1+V_2}, \Delta z\frac{2\,V_2}{V_1+V_2}\right)\Big|,
\end{aligned} \tag{3.48}$$

where $\Delta\omega_{12} = \omega\frac{\Delta\,V_{12}}{V_2}$ with $\Delta\,V_{12} = |\,V_1 - V_2|$. The window width Δz is comparable to the beat length of the fiber, so the above integral essentially captures the feature of mode coupling. Most importantly, the frequency dependence of functions in Eq. (3.48) are correlated mainly because these functions $K_j(\omega, z', \Delta z)$ are originated from the same

function $\kappa(z')$ with only difference in scaling factors. Therefore, one can measure the group index difference in the autocorrelation functional plot of $I_{\Delta z}(\omega, z')$. The autocorrelation calculation of $I_{\Delta z}(\omega, z')$ will reveal a central peak at $\omega = \overline{\omega}$ and side peaks at $\omega = \overline{\omega} + \frac{\Delta\overline{\omega}_{12}}{2}$ and $\omega = \overline{\omega} + \Delta\overline{\omega}_{12}$. In other words, the distances between these side peaks and the central peak give the amounts of frequency shifts of $\frac{\Delta\overline{\omega}_{12}}{2}$ and $\Delta\overline{\omega}_{12}$.

Since

$$\begin{aligned}\Delta\omega_{12} &= \omega\frac{\Delta V_{12}}{V_2} = \omega\frac{|V_1 - V_2|}{V_2} \\ &= \omega\frac{\left|\frac{c}{n_{g1}} - \frac{c}{n_{g2}}\right|}{\frac{c}{n_{g2}}} = \omega\frac{|n_{g2} - n_{g1}|}{n_{g1}} = \omega\frac{\Delta m_{12}}{n_{g1}},\end{aligned} \tag{3.49}$$

we have

$$\Delta m_{12} = \frac{\Delta\omega_{12}}{\omega} n_{g1}. \tag{3.50}$$

Since $\lambda = \frac{2\pi c}{\omega}$, $\Delta\lambda = \frac{2\pi c}{\omega^2}\Delta\omega = \frac{\Delta\omega}{\omega}\lambda$, we have

$$\Delta m_{12} = \frac{\Delta\lambda_{12}}{\lambda} n_{g1}. \tag{3.51}$$

Therefore, the group index difference between the modes of the tapers is obtained by measuring the frequency shifts or wavelength shifts through autocorrelation calculation of the spectrum.

In the case of three modes in the tapers, we have group indices of n_{g1}, n_{g2} and n_{g3} and

corresponding group velocities of V_1 , V_2 and V_3. Eq. (3.36) will include six components as follows,

$$\begin{aligned} I(\omega) = \sum_{z'} \Bigg\{ & \alpha_1(z')\,\kappa(z')\,\delta\left(\omega - \frac{2z'}{V_1}\Omega\right) + \alpha_2(z')\,\kappa(z')\,\delta\left(\omega - \frac{2z'}{V_2}\Omega\right) \\ & + \alpha_3(z')\,\kappa(z')\,\delta\left(\omega - \frac{2z'}{V_3}\Omega\right) \\ & + \alpha_{12}(z')\,\kappa(z')\,\delta\left[\omega - z'\Omega\left(\frac{1}{V_1} + \frac{1}{V_2}\right)\right] \\ & + \alpha_{13}(z')\,\kappa(z')\,\delta\left[\omega - z'\Omega\left(\frac{1}{V_1} + \frac{1}{V_3}\right)\right] \\ & + \alpha_{23}(z')\,\kappa(z')\,\delta\left[\omega - z'\Omega\left(\frac{1}{V_2} + \frac{1}{V_3}\right)\right] \Bigg\}. \end{aligned} \tag{3.52}$$

Its OTDR-like curve along the taper length is given by

$$\begin{aligned} S(\bar{z}) = & \frac{V_1}{2\Omega} a_1(\bar{z})\,\kappa(\bar{z}) + \frac{V_2}{2\Omega} a_2\left(\bar{z}\frac{V_2}{V_1}\right)\kappa\left(\bar{z}\frac{V_2}{V_1}\right) + \frac{V_3}{2\Omega} a_3\left(\bar{z}\frac{V_3}{V_1}\right)\kappa\left(\bar{z}\frac{V_3}{V_1}\right) \\ & + \frac{V_1 V_2}{\Omega(V_1 + V_2)} a_{12}\left(\bar{z}\frac{2V_2}{(V_1 + V_2)}\right)\kappa\left(\bar{z}\frac{2V_2}{V_1 + V_2}\right) \\ & + \frac{V_1 V_3}{\Omega(V_1 + V_3)} a_{13}\left(\bar{z}\frac{2V_3}{(V_1 + V_3)}\right)\kappa\left(\bar{z}\frac{2V_3}{V_1 + V_3}\right) \\ & + \frac{V_2 V_3}{\Omega(V_2 + V_3)} a_{23}\left[\bar{z}\frac{2V_2 V_3}{V_1(V_2 + V_3)}\right]\kappa\left[\bar{z}\frac{2V_2 V_3}{V_1(V_2 + V_3)}\right]. \end{aligned} \tag{3.53}$$

Then an appropriate window is applied to the OTDR-like curve and its spectrum response

is expressed as

$$
\begin{aligned}
I_{\Delta z}(\omega, z') = & \left| \sqrt{2\pi} \int_{z'}^{z'+\Delta z} e^{i\omega z} S(z)\, dz \right| \\
= & \frac{V_1}{2\Omega} \Bigg| K_1(\omega, z', \Delta z) + K_2\left(\omega + \Delta\omega_{12}, z' \frac{V_2}{V_1}, \Delta z \frac{V_2}{V_1}\right) \\
& + K_3\left(\omega + \Delta\omega_{13}, z' \frac{V_3}{V_1}, \Delta z \frac{V_3}{V_1}\right) \\
& + K_{12}\left(\omega + \frac{\Delta\omega_{12}}{2}, z' \frac{2\,V_2}{V_1 + V_2}, \Delta z \frac{2\,V_2}{V_1 + V_2}\right) \\
& + K_{13}\left(\omega + \frac{\Delta\omega_{13}}{2}, z' \frac{2\,V_3}{V_1 + V_3}, \Delta z \frac{2\,V_3}{V_1 + V_3}\right) \\
& + K_{23}\left(\omega + \frac{\Delta\omega_{12} + \Delta\omega_{13}}{2}, z' \frac{2\,V_2\,V_3}{V_1\,(V_2 + V_3)}, \Delta z \frac{2\,V_2\,V_3}{V_1\,(V_2 + V_3)}\right) \Bigg|, \qquad (3.54)
\end{aligned}
$$

where $\Delta\omega_{ij} = \omega \frac{\Delta V_{ij}}{V_j}$ with $\Delta V_{ij} = |V_i - V_j|$. Similarly, the frequency dependence of functions in Eq. (3.54) are correlated mainly because these functions $K_j(\omega, z', \Delta z)$ are originated from the same function $\kappa(z')$ with only difference in scaling factors. Therefore, one can measure the group index difference in the autocorrelation functional plot of $I_{\Delta z}(\omega, z')$. The distances between these side peaks and the central peak give the amounts of frequency shifts of $\frac{\Delta\overline{\omega}_{12}}{2}$, $\frac{\Delta\overline{\omega}_{13}}{2}$, $\Delta\overline{\omega}_{12}$, $\frac{\Delta\overline{\omega}_{12}+\Delta\overline{\omega}_{13}}{2}$, $\Delta\overline{\omega}_{13}$ and their differences among these modes. Since

$$
\Delta m_{ij} = \frac{\Delta\omega_{ij}}{\omega} n_{gi} = \frac{\Delta\lambda_{ij}}{\lambda} n_{gi}, \qquad (3.55)
$$

the group index differences among these modes of the tapers are obtained by measuring the frequency shifts or wavelength shifts.

3.4 Experimental setup and results

The experimental setup to measure Rayleigh backscatter as a function of fiber length is shown in Fig. 3.1. It consists of a TLS (Agilent 81980A) with a sweep rate of 40nm/s, two polarization controllers (PC_1 and PC_2), a measurement interferometer, an auxiliary interferometer with 64m differential delay, and a polarization beam diversity receiver. According to Eq. (3.8), a wide sweep range of tunable laser (1510–1570nm) produces high spatial resolution of 13μm. PC_1 is required in polarization diversity measurement to adjust the polarization of the local path to have the same power for p- and s-components, respectively. PC_2 is used to adjust the polarization of the input light to the FUT for optimization of the measurement. Since the polarization state of the scattered signal is arbitrary, we adopt the polarization diversity detection technique, including a polarization beam splitter (PBS), two PDs and a high-speed data acquisition card (DAQ). The auxiliary MZI provides interference fringes, which are used to trigger data acquisition and help to mitigate the tuning errors of the laser. The measured p- and s-components of interference fringes are digitized as a function of laser frequency and stored in memory, as shown in Fig. 3.3(a). Figure 3.3(b) shows complex Fourier transform of p-component interference signal. The OTDR-like curves along the fiber length, including p- and s-components and their vector sum, are presented in Fig. 3.3(c). When a section of complex Fourier transform data is selected, as shown in Fig. 3.3(d), its inverse Fourier transform result and autocorrelation calculation are displayed in Figs. 3.3(e) and (f), respectively.

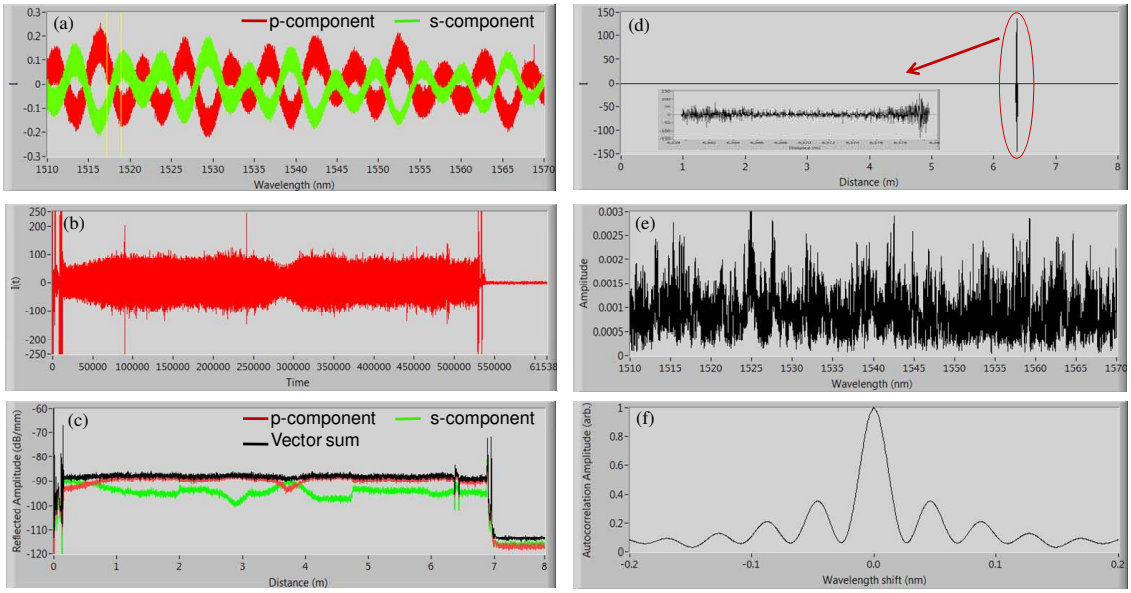

Figure 3.3: (a) AC interference signals measured at the detectors, which are digitized in the frequency domain. (b) Complex Fourier transform of p-component interference signal. (c) The OTDR-like curves, including p- and s-components and their vector sum. (d) A section of complex Fourier transform shown in (b) is selected. (e) Inverse Fourier transform result. (f) Autocorrelation calculation.

As shown in Fig. 3.4(a), the original data of the OTDR-like curve is presented, which is associated with a spatial resolution of 13μm. In order to show the profile of the taper, a low-pass filter (LPF) is added, as shown in Figs. 3.4(b) and (c). It seems that the spatial resolution, which is shown as the 3dB bandwidth of the reflection at the fiber end, becomes worse by using an LPF with a lower frequency. Figure 3.4(d) shows the result of taking average over every 1000 points and its effective spatial resolution is ~1cm. However, comparing Figs. 3.4(a)-(d), the OTDR-like curves over the taper range have similar shape. In order to show the profile of the taper, all OTDR-like curves in this chapter have been smoothed using a LPF of f=0.003Hz with an effective spatial

resolution of ∼1.7mm. Autocorrelation calculations are based on the original data.

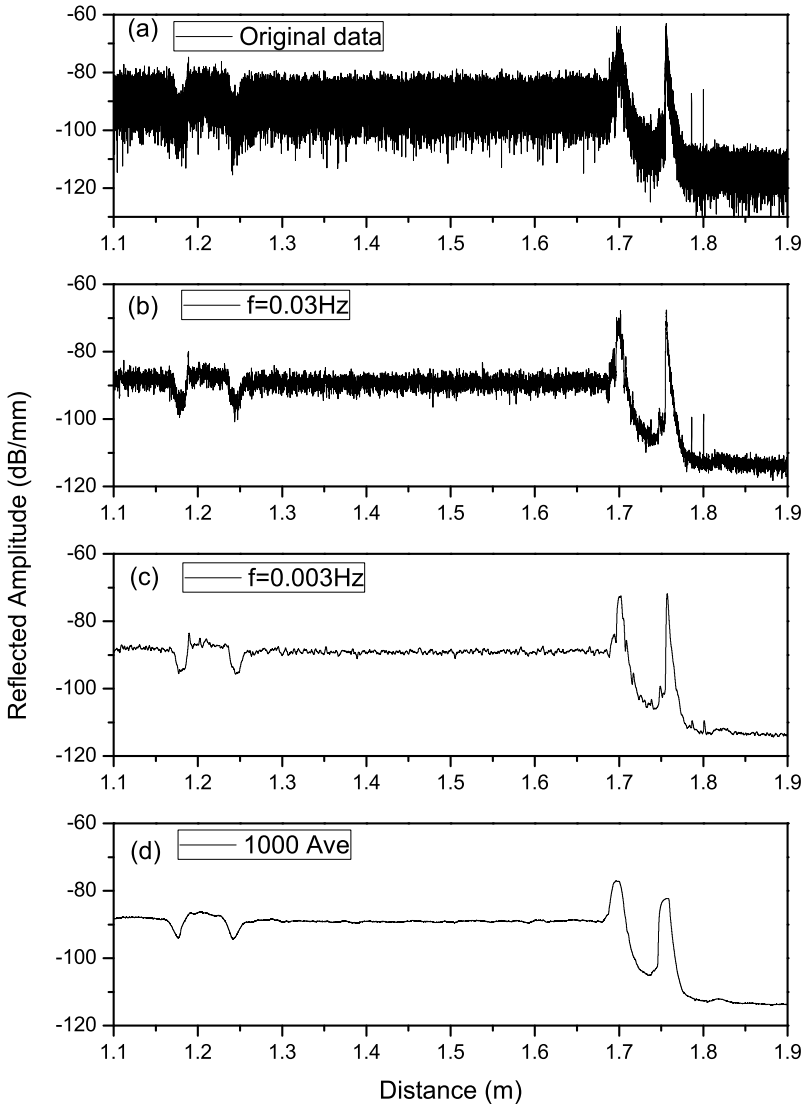

Figure 3.4: (a) The original data of the OTDR-like curve. (b), (c) The OTDR-like curves with a LPF of f=0.03Hz and f=0.003Hz, respectively. (d) The OTDR-like curve of taking average over every 1000 points.

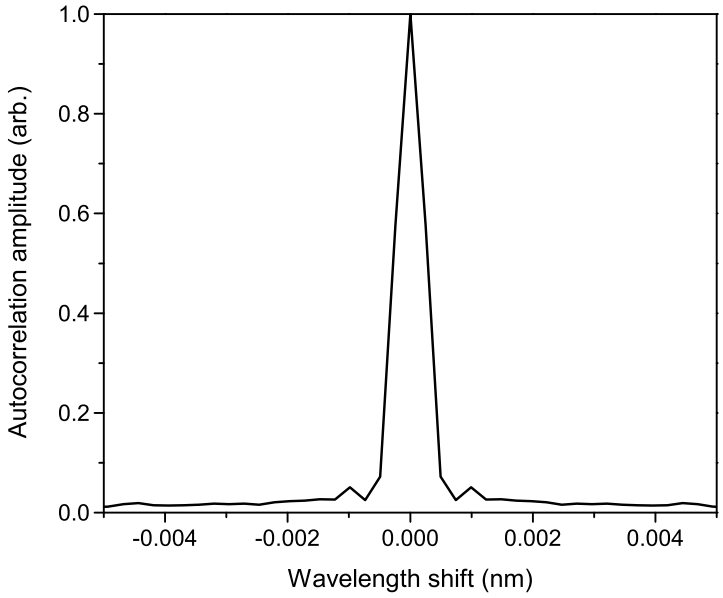

Figure 3.5: Autocorrelation of the spectrum of a 1.3m segment of SMF.

Within a section of SMF (Corning, SMF-28^{TM}), a ∼1.3m width of autocorrelation window is applied to obtain high spectral resolution and to measure this low residual stress-induced birefringence, which results from the fiber fabrication process. The window width should be comparable to the beat length of the FUT. The autocorrelation of the spectrum is shown in Fig. 3.5. By using Eq. (3.40), the wavelength shift of $\Delta\lambda$=0.001nm leads to the average group index difference Δm=9.47×10^{-7} for the segment of SMF. This value is consistent with the group birefringence measured by Brillouin optical time-domain analysis (BOTDA) [71]. Here n_g=1.4681 and λ=1550nm.

3.4.1 Gently tapered SMF

The gentle tapers are fabricated by using heating and stretching technique [9]. With help of a high magnification microscope, the geometric structure of tapered fiber is described point by point. The diameter of the tapered SMF is shown in Fig. 3.6(a). The waist diameter of the taper is $\sim$12.2μm and the lengths of the down-taper, uniform waist and up-taper sections are 3.1cm, 4.75cm, and 2.4cm, respectively. Figure 3.6(a) also shows the reflected spectrum of Rayleigh backscatter as a function of distance along the tapered SMF. In order to show the profile of the taper, the OTDR-like curve has been smoothed using a LPF with an effective spatial resolution of 1.7mm. Comparing the two curves in Fig. 3.6(a), the geometric waveguide structure cannot show the actual energy coupling between the fundamental mode and high order modes. Rayleigh backscatter in optical fiber is caused by a change in the refractive index along the fiber length. Therefore, the amplitude fluctuation of Rayleigh backscatter as a function of fiber distance provides more accurate information than the geometric image of the taper. When the amplitude of the reflected backscatter decreases, it indicates the energy re-distribution, in other words, the generation of higher-order modes. In the down-taper region, the energy is transferred from the fundamental mode to higher-order modes, which are leaky modes due to the small optical area. The lowest mode with reduced energy makes a dominating contribution to Rayleigh backscatter. Thus, the corresponding amplitude of backscatter signal is reduced. The first dip in the reflected amplitude of Rayleigh backscatter indicates the minimum scatter level, which is 6dB lower than that of SMF. The amplitude

increasing in the next region means that more energy is coupled back from higher-order modes to the fundamental mode. In the uniform waist region, the number of modes guided in the fiber is constant. The spectral fluctuations result from the energy coupling among these several modes. The scatter level of the uniform segment of taper is 2dB higher than that of SMF due to the reduced cross-sectional area of the taper.

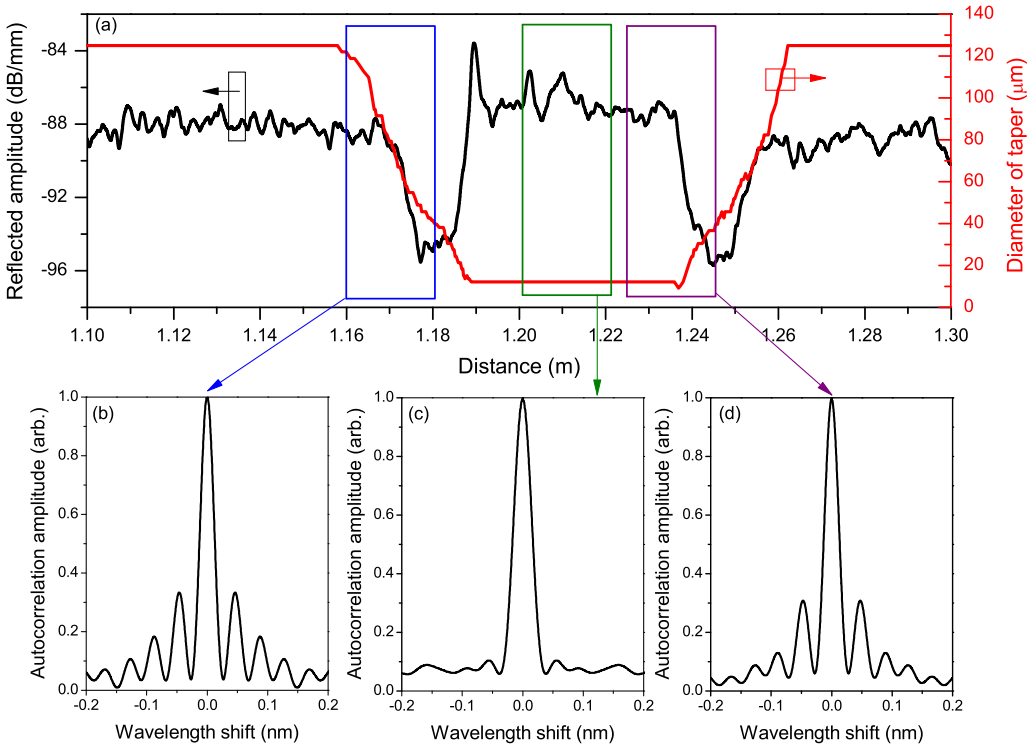

Figure 3.6: (a) Backscatter amplitude versus distance along the gently tapered SMF (the black curve) and the cladding diameter of the gently tapered SMF (the red curve). Length of taper: L=10.25cm; Uniform segment of taper: d=12.2μm, l=4.75cm. (b) The autocorrelation calculation of the spectrum of the down-taper range (the blue window in (a)). (c) The autocorrelation calculation of the spectrum of the uniform waist range (the green window in (a)). (d) The autocorrelation calculation of the spectrum of the up-taper range (the purple window in (a)). The widths of the windows are ~2.08cm.

At the edge of the uniform waist region, the backscatter signal starts to decrease. This is because the energy is transferred from the core mode to higher-order modes, which is not guided in the core. In the up-taper region, the scatter level reaches its second minimum value, which is 6dB lower than that of SMF. In the following region, the amplitude of Rayleigh backscatter starts to increase, because the energy is coupled back from higher-order modes to the fundamental mode as the diameter of tapered fiber increases. The analysis on Rayleigh backscatter shows the actual energy coupling process between the fundamental mode and higher-order modes in the tapered fiber. The length of mode coupling is in accordance with the geometric structure of the gently tapered fiber. However, more detailed energy re-distribution is observed through Rayleigh backscatter. Furthermore, the autocorrelations of the spectra of tapered fiber are shown in Figs. 3.6(b)–(d). A window with an appropriate width is applied to extract the response of the taper. It is important to note that the window width only affects the ratio of the amplitude of the side peaks to that of the central peak. A wider window incorporates more data points, and gives better spectral resolution and worse spatial resolution. There is a tradeoff between spectral resolution and spatial resolution due to finite rates of the TLS and the DAQ. In this case, we choose a width of 2.08cm, including 1600 data points in the time domain. The ratio of the amplitude of the first side peak to that of the central peak is over 0.3 and the amplitude ratio for the second side peak is $\sim$0.2. These peaks indicate the generation of one higher-order mode. The distances of the first and second side peaks from the central peak are equal to the wavelength shifts of $\frac{\Delta\lambda_{12}}{2}$

and $\Delta\lambda_{12}$, respectively. The measured results are 0.0456nm and 0.088nm, respectively. Therefore, the wavelength shift between the fundamental mode and higher-order mode is $\Delta\lambda_{12}$=0.0896nm. and the group index difference is Δm_{12}=8.49×10^{-5}. Here n=1.4681 and $\lambda = 1550nm$. The same wavelength shifts in Figs. 3.6(b) and (d) indicate the symmetrical generation of same higher-order modes in the down-taper and up-taper regions. Less side peaks in Fig. 3.6(c) means that negligible coupling between excited local modes take place at the central quasi-adiabatic uniform waist region. The experimental result agrees with the theoretical model [27].

The measured group index difference, which is an average parameter in the segment of the tapered fiber, results from two factors. The first factor is the geometric structure change of the taper. As the cladding diameter of fiber is tapered down, the effective refractive index of the fundamental mode decreases. The theoretical calculation of n_{eff} as a function of the cladding diameter of taper is shown in Fig. 2.1. It indicates that the group index difference results in part from the geometric structure. The second factor is the generation of higher-order modes. As the diameter of taper is reduced to the "cut-off" transition [25], the energy is coupled from the fundamental mode to higher-order modes. The group index difference results from different modes at a given location of the taper. Using theoretical values of effective refractive indices for LP_{01} and LP_{02} modes, we calculate the average group index difference in the same window as the blue one in Fig. 3.6(a). When the diameter of the tapered fiber is reduced from 122μm to 40μm, theoretical average group index difference between LP_{01} and LP_{02} modes is $\Delta m_{LP01-02}$=-

8.12×10^{-5}. Therefore, the experimental result of Δm_{12}=8.49×10^{-5} is reasonable. The first and second side peaks in Fig. 3.6(b) indicate the generation of LP_{02} mode in the gentle taper, which is regarded as an axisymmetric taper. In order to calculate the group index difference between modes, the impact of geometric structure change should be reduced by decreasing the window width for autocorrelation calculation. In order to obtain enough data points in the reduced window, we need to increase the sweep rate of TLS.

3.4.2 Abruptly tapered SMF

The abrupt tapers are fabricated by using an Ericsson fusion splicer (FSU–995FA) with a customized tapering program. Microscope images of tapers are shown in Fig. 3.7. The waist diameters of the tapers are 76μm, 66μm, 49μm and 35μm, respectively. The lengths of the tapers are 0.85mm, 0.85mm, 1mm and 1.23mm, respectively. In Fig. 3.7, the peaks around the distance of 0.3m mean the reflection of the knots near the end of fiber. In the case of weak tapers, such as taper (a), the scatter level drops by ∼1dB. When the waist diameter is reduced to 66μm, the scatter level drops by ∼2dB. In the case of abrupt tapers with the waist diameters of 49μm and 35μm, the scatter levels drop by ∼8dB and ∼12dB, respectively. The fluctuation of Rayleigh backscatter indicates the energy re-distribution among modes in tapered fibers. In other words, it indicates the generation of higher-order modes. As shown in Fig. 3.7(c), the energy of fundamental core mode is split into higher-order modes when the fiber is tapered down

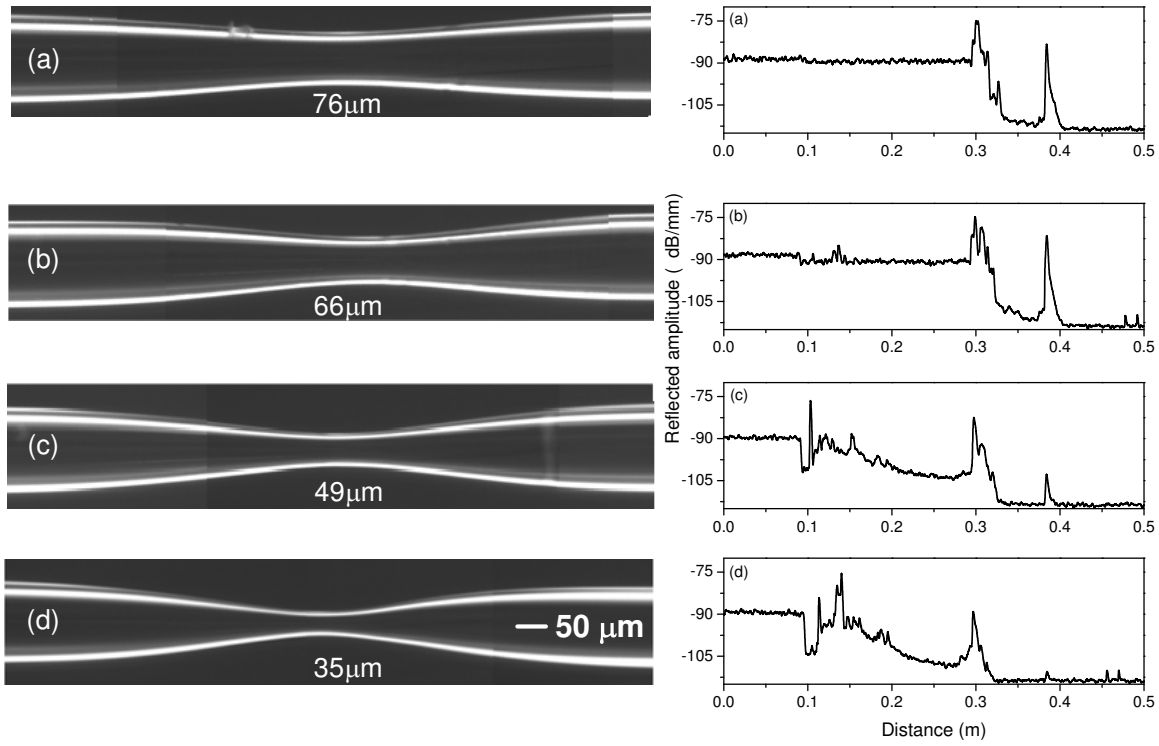

Figure 3.7: Microscope images of the abruptly tapered SMFs (left) and backscatter amplitude versus distance of the tapers (right). (a) d=76μm, L=0.85mm; (b) d=66μm, L=0.85mm; (c) d=49μm, L=1mm; (d) d=35μm, L=1.23mm. The length of inset scale bar is 50μm.

to a cladding diameter of 49μm. The experimental results accord with the theoretical calculation in Chapter 2, which shows that the "cut-off" transition value of the cladding diameter of the taper is 51.1μm. Furthermore, the fluctuation of the reflected amplitude of Rayleigh backscatter exists in a length of several centimeters, which is much longer than the geometric lengths of tapers (c) and (d).

Figure 3.8(a) shows the reflected spectrum of Rayleigh backscatter along a length of the taper (d) and its diameter. In order to show the profile of the taper, Fig. 3.8(a) has

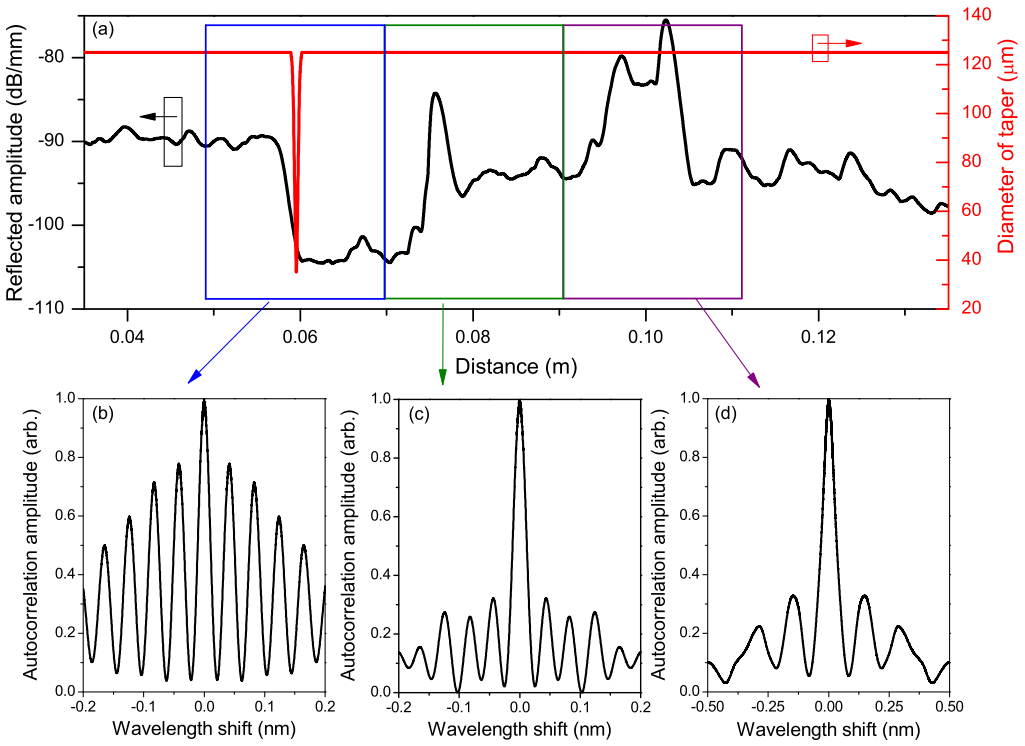

Figure 3.8: (a) Backscatter amplitude versus distance along the abrupt taper (the black curve), as shown in Fig. 3.7(d), and its cladding diameter (the red curve). (b)–(d) Autocorrelation calculations of the spectra of three segments of tapered fiber, respectively. The widths of the windows are ∼2.08cm.

been smoothed using a low-pass filter with an effective spatial resolution of ∼1.7mm. An autocorrelation of the spectrum of the first segment is shown in Fig. 3.8(b). The ratio of the amplitude of the first side peak to that of the central peak reaches ∼0.8. Even the fourth side peak has a ratio of ∼0.5 to that of the central peak. The distances of four side peaks from the central peak are 0.0417nm, 0.0829nm, 0.124nm and 0.165nm, respectively. As discussed in section 3.3.2, in the case of three modes, the side peaks of the autocorrelation will appear at $\frac{\Delta\lambda_{12}}{2}$, $\frac{\Delta\lambda_{13}}{2}$, $\Delta\lambda_{12}$, $\frac{\Delta\lambda_{12}+\Delta\lambda_{13}}{2}$, $\Delta\lambda_{13}$ and their differences.

We will obtain the measured wavelength shifts of $\Delta\lambda_{12}$=0.083nm and $\Delta\lambda_{13}$=0.165nm and the group index differences of Δm_{12}=7.86×10^{-5} and Δm_{13}=1.56×10^{-4}. Theoretical average group index differences are calculated when the diameter of the tapered fiber is reduced from 125μm to 35μm. We obtain theoretical values of $\Delta m_{LP01-11}$=-7.84×10^{-5} and $\Delta m_{LP01-02}$=-1.61×10^{-4}. Therefore, the corresponding wavelength shifts are $\Delta\lambda_{12}$=0.083nm and $\Delta\lambda_{13}$=0.171nm, respectively. Then theoretical wavelength shifts are 0.0415nm, 0.083nm, 0.085nm, 0.127nm and 0.171nm. The second and third terms, $\frac{\Delta\lambda_{13}}{2}$ and $\Delta\lambda_{12}$ cannot be distinguished and they are shown as the second side peaks. Comparing the theoretical values, these peaks in Fig. 3.7 (b) indicate the generation of LP_{11} and LP_{02} modes in the abrupt taper, which is regarded as a non-axisymmetric taper. However, theoretical average group index difference within the ∼2.08cm segment of fiber must be calculated based on a model combining a segment of SMF (0–1.96cm) and the abrupt taper with a length of ∼1.23mm and a waist diameter of 35μm, because the mode coupling length is unknown. The geometric length of the taper is regarded as minimum coupling length (∼1.23mm) and the window width is regarded as maximum coupling length (∼2.08cm). As shown in Table 3.1, the experimental results are closed to the upper limit of these theoretical values. This is because the higher-order modes exist in a longer physical length along the tapered fiber than its geometric length. The actual coupling process is observed through Rayleigh backscatter. The autocorrelation is performed to the next ∼2.08cm section of fiber. Figure 3.7(c) shows same wavelength shifts with different energy ratio. It indicates the energy re-distribution among these

modes in taper. The mode number reduces in the third ∼2.08cm segment of fiber, which shows fewer side peaks in Fig. 3.7(d). Here $\Delta\lambda_{12}$=0.29nm and hence Δm_{12}=2.75×10^{-4}. It indicates that there is still one mode in the third window in Fig. 3.7(a), even it is several centimeters away from the taper. It is found that the physical length of mode coupling of tapered fiber is different from its geometric image. By using OFDR scheme and Eq. (3.40), the observation of mode coupling and the accurate measurement of group index differences in tapers are achieved with a ∼2cm resolution.

Table 3.1: Measured and theoretical group index difference of LP_{01} and $LP_{\upsilon m}$ for the abrupt taper with d=35μm, L=1.23mm.

$\Delta\lambda$ (nm)	Δm	Theoretical values Δm
$\Delta\lambda_{12}$=0.083	Δm_{12}=7.86×10^{-5}	$\Delta m_{LP_{01-11}}$=-4.73×10^{-6} -7.84×10^{-5}
$\Delta\lambda_{13}$=0.165	Δm_{13}=1.56×10^{-4}	$\Delta m_{LP_{01-02}}$=-9.64×10^{-6} -1.61×10^{-4}

3.5 Conclusion

We propose a rapid and nondestructive approach to reveal the excited modes of fiber tapers. Distributed mode coupling processes along gentle and abrupt tapers are experimentally measured with OFDR technology. The detailed energy re-distribution among modes is measured continuously through Rayleigh backscatter as a function of distance with a 13μm resolution along the length of the tapers. In addition, a plot of the autocorrelation calculation shows the generation of higher-order modes. The wavelength shifts between the fundamental mode and higher-order modes of the taper are theoretically

derived and experimentally verified. The accurate measurement of group index differences between the fundamental mode and high order modes in tapered fibers with ∼2cm resolution is achieved through the autocorrelation calculation in the spectral domain. We find that the mode coupling in gentle tapers exists in the same lengths as their geometric lengths, while the mode coupling in abrupt tapers exists in longer segments than their geometric lengths. One could improve the measurement resolution by using a tunable laser with higher tuning rate. In this way, one could obtain a precise measurement of group index difference at a given location along the tapered fiber.

Chapter 4

Thermal and mechanical properties of tapered fiber measured with OFDR and its application for high-sensitivity force measurement

This chapter studies the thermal and mechanical properties of fiber tapers by using an Optical Frequency-domain Reflectometry (OFDR) scheme, and a highly sensitive force sensor is proposed based on the fiber taper. Section 4.1 shows the background of the research. Section 4.2 describes the fabrication of a gentle fiber taper and the principle of OFDR measurement based on our previous work [72]. Section 4.3.1 and section 4.3.2 present the experimental results on thermal and mechanical properties of the taper and

its variation along the taper length, respectively.

4.1 Introduction

During the tapering process, stress is introduced to a fiber taper and causes the inhomogeneous refractive index distribution. This will degrade the optical quality of the fiber taper for its applications. To the best of our knowledge, the thermal and mechanical properties, particularly their variations at different locations along the tapered fiber, have not been studied. Fiber tapers with small diameters become interesting also for force measurement. When a section of fiber taper is stretched by an axial force F, the strain applied on the taper scales inversely with the cross-sectional area or the square of the diameter of the taper as long as Young's modulus is considered independent of the diameter [73]. This dependence is because $\varepsilon = \frac{F}{EA}$, where ε is the applied strain in the fiber, F is the axial force, E is Young's modulus of the fiber material and A is the cross-sectional area of the fiber. Therefore, at the same force level, the fiber taper with reduced waist diameter has several hundred times more strain than that of single-mode fiber (SMF). A high force measurement has been achieved using fiber Bragg gratings (FBGs) inscribed in the waist of a tapered fiber [73]. However, for tapers with a diameter below $\sim 16\mu$m, the variation of the effective refractive index with diameter should be taken into account [73], so that it becomes hard to fabricate FBG in tapered SMFs with smaller waist diameters. As reported in this chapter, a high-sensitivity force sensor can be achieved by measuring the group index change, thus the force applied to the fiber

taper. Here we realize the force sensor by measuring Rayleigh backscattering spectral change by using high-sensitivity, high-resolution OFDR technique.

Rayleigh backscatter in optical fiber is caused by random fluctuations in the refractive index profile along the fiber length, and it varies randomly along the fiber length due to inhomogeneity of the fiber. Changes in the refractive index profile caused by an external stimulus, such as temperature or strain, will induce spectral shift being measured by OFDR. Recent publications have demonstrated that SMFs and polarization-maintaining fibers (PMFs) can be used as Rayleigh scattering-based temperature or strain sensor by using high-resolution, high-sensitivity OFDR, and the use of PMFs makes it possible to discriminate the temperature and strain through data processing schemes including complex fast Fourier transfer (FFT), autocorrelation and cross-correlation, etc. [59, 62]. In the case of PMFs, the group birefringence of the fiber, which is group index difference between the fast and slow modes, can be deduced from spectral shifts through auto-correlation calculation, while the group index change of the fast (or slow) mode can be deduced from using cross-correlation calculation. These two parameters are temperature and strain dependent, which makes it possible to assess these parameters simultaneously. In the case of fiber tapers, the autocorrelation wavelength shift indicates the group index difference between the fundamental mode and higher-order modes through mode coupling process; in the uniform region of taper with a small waist diameter, the cross-correlation wavelength shift indicates the group index change of the fundamental mode as the fundamental mode becomes the dominating one [72].

In this chapter, we represent our study on the thermal and mechanical properties of fiber tapers by using an OFDR scheme, and a highly sensitive force sensor is proposed based on the fiber taper. In temperature and force measurements, the temperature or force sensitivity is defined as the ratio of wavelength shift, and the change of temperature or force. The wavelength shift is calculated through cross-correlation of Rayleigh scatter spectra from a selected section of fiber before and after the temperature or force is applied to the fiber. As described in section 4.3.1, the non-annealed taper has its inhomogeneous thermal property and the annealed taper has homogeneous temperature coefficient, similar to that of SMF ($\sim$0.01nm/°C). In section 4.3.2, the mechanical property of the taper and its variation along the taper length are studied and measured with a spatial resolution of 3.85mm. It is demonstrated that the force sensitivity is improved by decreasing the waist diameter of the uniform segment along the taper, e.g., when the waist diameter is reduced to $\sim 6\mu$m, a force sensitivity of 620.83nm/N with a force resolution of 6.35μN is achieved, which is about 500 times higher than that of the SMF. It is noted that fiber taper can be used as a temperature-independent force sensor due to huge difference between its force and temperature sensitivities.

4.2 Principle

The heating and stretching technique [9] is introduced to fabricate the gentle tapers. A section of SMF is fixed on two linear translation stages with submicron precision and the middle jacket-off fiber is hanging. A small region of the fiber is heated by a scanning

hydrogen flame. After a pre-heating process, the fiber is stretched slowly while the scanning range of the flame is increasing. The pulling speed of the translation stages, the scanning speed and the scanning range of the flame are accurately controlled by a computer. The slow stretching technique leads to the taper with gentle slopes in the down-taper and up-taper regions and a uniform region with reduced diameter waist.

In OFDR, the interference Rayleigh backscatter signal of the fiber taper is monitored and the complex Fourier transform is carried out to obtain OTDR-like curves along the taper length. A polarization-independent signal is obtained by calculating the vector sum of the p- and s-components of the detected signal. During the uniform range of the gentle taper, linearly polarized (LP) mode, LP_{01} mode is a dominating mode, which contains most of energy, with group index n_g and its corresponding group velocity $V_g = \frac{c}{n_g}$ inside the fiber, where c is the speed of light in vacuum. The OTDR-like signal along the uniform taper length is expressed as [72]

$$S(\bar{z}) = \frac{V_g}{2\Omega}\kappa(\bar{z}), \tag{4.1}$$

where $\bar{z} = \frac{\omega V_g}{2\Omega}$ and Ω is a constant sweep rate of tunable laser, $\kappa(\bar{z})$ is directly related to local Rayleigh backscatter strength. An appropriate window with a width of Δz is applied at the position z' along the OTDR-like curve and the spectrum response is

obtained through inverse Fourier transform data processing, as follows:

$$\begin{aligned} I_{\Delta z}(\omega, z') =& \left| \sqrt{2\pi} \int_{z'}^{z'+\Delta z} e^{i\omega z} S(z)\, dz \right| \\ =& \frac{V}{2\Omega} \left| K(\omega, z', \Delta z) \right|, \end{aligned} \tag{4.2}$$

where $K(\omega, z', \Delta z) = \sqrt{2\pi} \int_{z'}^{z'+\Delta z} e^{i\omega z} \kappa(z)\, dz$. A reference measurement is taken in the initial state. Then a sensing measurement of the same taper is taken after the temperature or force is changed. Therefore, one can measure the spectral shift in the cross-correlation functional plot of $I_{\Delta z}(\omega, z')$, which gives the amount of changed group index of LP_{01} mode. Because the group index is determined by the change of temperature or force, the thermal and mechanical properties of the taper can be investigated by measuring the wavelength shift through cross-correlation calculation of the spectra. Here, the sensitivity is defined as the ratio of wavelength shift of cross-correlation calculation and the change of temperature or force, which is given by $\zeta_T = \frac{\Delta\lambda_{c.c.}}{\Delta T}$ and $\zeta_F = \frac{\Delta\lambda_{c.c.}}{\Delta F}$, respectively.

When a section of fiber is stretched, it is subjected to a deformation proportional to the amplitude of the force within elastic range of the fiber. Within this elastic range, the mechanical deformation is reversible. Here, the applied force F is expressed as

$$F = EA\frac{\Delta x}{x}, \tag{4.3}$$

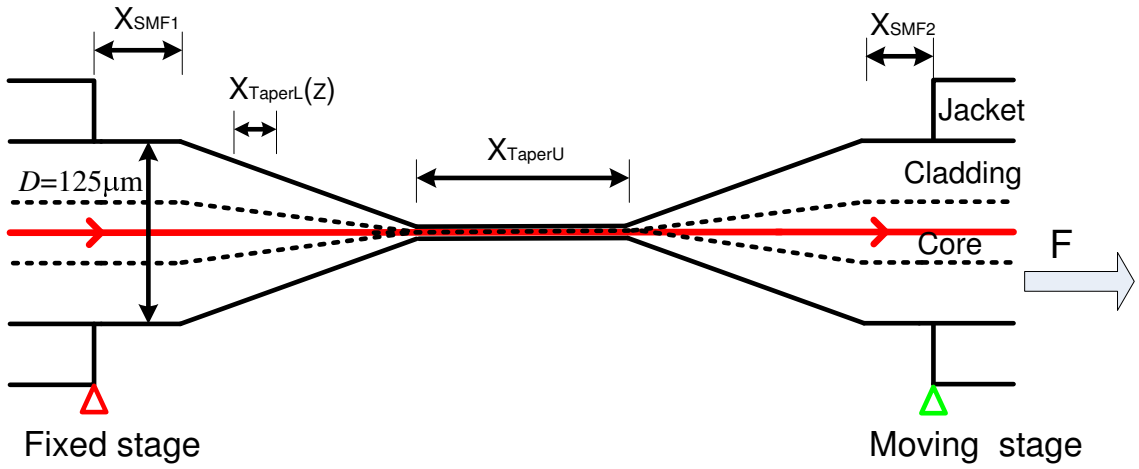

Figure 4.1: Sketch image of the gentle taper. x_{TaperU}, x_{SMF}, and $x_{TaperL}(z)$ are the initial length of jacket-off SMF, the uniform segment in taper, and a sub-segment in the up- and down-segment in taper, respectively.

where for fiber without coating, $E = 7.18 \times 10^{10} N/m^2$ [74], x is the initial length of the fiber, Δx is the length change of relative deformation imposed by the force F. As shown in Fig. 4.1, we have

$$\Delta x = \Delta x_{TaperU} + \Delta x_{SMF} + \sum_z \Delta x_{TaperL}(z), \tag{4.4}$$

$$x = x_{TaperU} + x_{SMF} + \sum_z x_{TaperL}(z), \tag{4.5}$$

where Δx_{SMF}, Δx_{TaperU}, and $\Delta x_{TaperL}(z)$ are the length change of SMF, the uniform segment in taper, and a sub-segment in the up- and down-segment in taper, respectively. x_{SMF}, x_{TaperU}, and $x_{TaperL}(z)$ are the initial length of jacket-off SMF, the uniform segment in taper, and a sub-segment in the up- and down-segments in taper, respectively. Δx and x are the total length change and initial length of the whole fiber, respectively.

The length changes of each segment satisfy the following relations

$$\frac{\Delta x_{SMF}}{\Delta x_{TaperU}} = \frac{Fx_{SMF}}{EA_{SMF}} \frac{EA_{TaperU}}{Fx_{TaperU}} = \frac{x_{SMF}}{x_{TaperU}} \left(\frac{d_{TaperU}}{d_{SMF}} \right)^2, \tag{4.6}$$

$$\frac{\Delta x_{TaperL}(z)}{\Delta x_{TaperU}} = \frac{Fx_{TaperL}(z)}{EA_{TaperL}(z)} \frac{EA_{TaperU}}{Fx_{TaperU}} = \frac{x_{TaperL}(z)}{x_{TaperU}} \left(\frac{d_{TaperU}}{d_{TaperL}(z)} \right)^2, \tag{4.7}$$

where d_{SMF}, d_{TaperU}, and $d_{TaperL}(z)$ are the diameter of SMF, the uniform segment in taper, and a sub-segment in the up- and down-segments in taper, respectively. Young's modulus is assumed to be constant when the fiber is tapered. Therefore, we have

$$\Delta x_{TaperU} = \frac{\Delta x}{\gamma}, \tag{4.8}$$

where γ is a normalization factor and given by

$$\gamma = 1 + \frac{x_{SMF}}{x_{TaperU}} \left(\frac{d_{TaperU}}{d_{SMF}} \right)^2 + \sum_z \frac{x_{TaperL}(z)}{x_{TaperU}} \left(\frac{d_{TaperU}}{d_{TaperL}(z)} \right)^2. \tag{4.9}$$

Inserting Eq. (4.8) into (4.3), the force is calculated by

$$F = EA_{TaperU} \frac{\Delta x_{TaperU}}{x_{TaperU}} = \frac{\pi E d_{TaperU}^2 \Delta x}{4\gamma x_{TaperU}}. \tag{4.10}$$

Thus, the force is calculated through the parameters of taper and the stretched length. Since the strain applied on the fiber is given by $\varepsilon = \frac{F}{EA}$, the strain applied on the uniform segment of taper is higher than that of the SMF. In theory, the ratio of the strains is

given by

$$\frac{\varepsilon_{TaperU}}{\varepsilon_{SMF}} = \frac{A_{SMF}}{A_{TaperU}} = \left(\frac{d_{SMF}}{d_{TaperU}}\right)^2. \tag{4.11}$$

The applied strain scales inversely with the cross-sectional area or the square of the diameter of the fiber. As the applied strain increases, the change of group index increases and then measured wavelength shift in cross-correlation is getting larger. Therefore, the uniform range of taper with smaller waist diameter has a higher force sensitivity ζ_F. Here we assume the diameter of the fiber is constant, which is independent on the applied force. This assumption is reasonable when the applied force is limited.

4.3 Experimental setup and results

The schematic diagram to measure Rayleigh backscatter as a function of fiber length is shown in Fig. 4.2. It consists of a tunable laser TLS with a sweep rate of 40nm/s, two polarization controllers (PC_1 and PC_2), a measurement interferometer, an auxiliary interferometer with 64m differential delay, and a polarization beam diversity receiver. A wide sweep range of tunable laser source (1510–1570nm) produces high spatial resolution of $13\mu m$. The auxiliary Mach-Zehnder interferometer (MZI) provides interference fringes, which are used to trigger data acquisition and help to mitigate the tuning errors of the laser. The polarization beam diversity receiver includes a polarization beam splitter (PBS), two photo-detectors (PD_1 and PD_2) and a high-speed data acquisition card

(DAQ). The interference fringes are digitized as a function of laser frequency and stored in memory. By scanning the segment window, all fiber length is mapped.

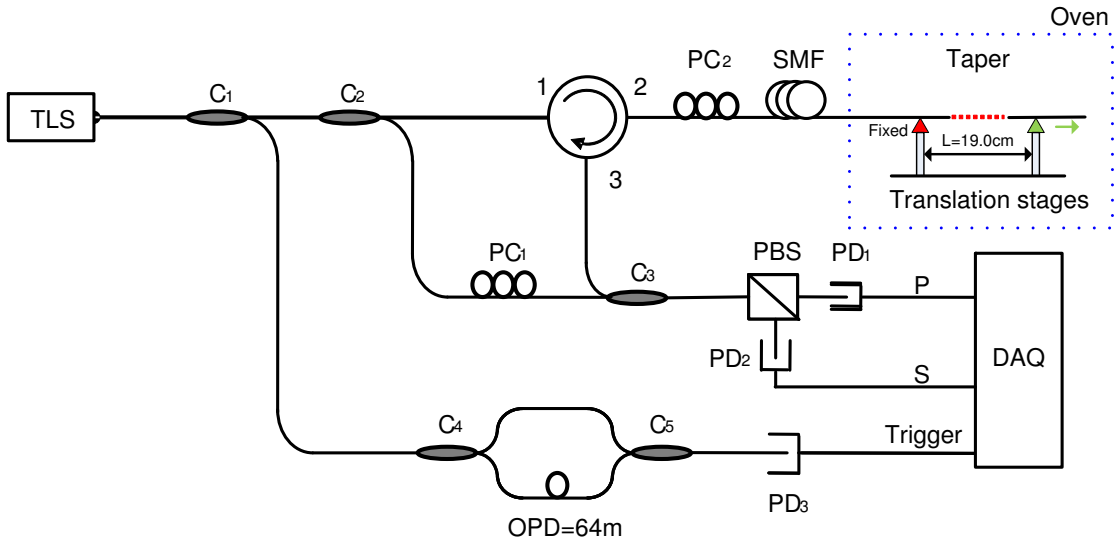

Figure 4.2: Schematic setup of OFDR system. TLS: tunable light source; C_1: 99 : 1 coupler; C_2, C_3, C_4, C_5: 50 : 50 couplers; PC: polarization controller; PBS: polarization beam splitter; PD: photodetector; OPD: optical path difference; DAQ: data acquisition.

With the help of a high-magnification microscope, the cladding diameter of taper A is measured point by point, as shown in Fig. 4.3(a). Figure 4.3(a) also shows the reflected spectrum of Rayleigh backscatter as a function of distance along the tapered SMF. The spectrum has been smoothed using a low-pass filter with an effective spatial resolution of ~1.7mm. The amplitude fluctuation of Rayleigh backscatter as a function of fiber distance shows the energy re-distribution among different modes continuously along the taper length [72].

4.3.1 Thermal properties

To investigate the thermal properties of a taper, taper A was put into an oven. A reference measurement was taken when the taper was at the initial temperature of 25°C. As shown in Fig. 4.3(a), we choose a window at position 4.37m with a width of ∼3.85mm, including 300 data points, along the OTDR-like curve. The spectrum response is obtained through inverse Fourier transform data processing. Then a sensing measurement of the same taper was taken after the temperature was changed. The cross-correlation of these two spectra reveals a central peak shift due to changed effective group index n_g, which represents the changed temperature. Figure 4.3(b) shows the left-shifted central peak in cross-correlation of the spectra of the non-annealed taper A, which indicates the temperature-induced refractive index change when the temperature is increased from 25°C to 38°C.

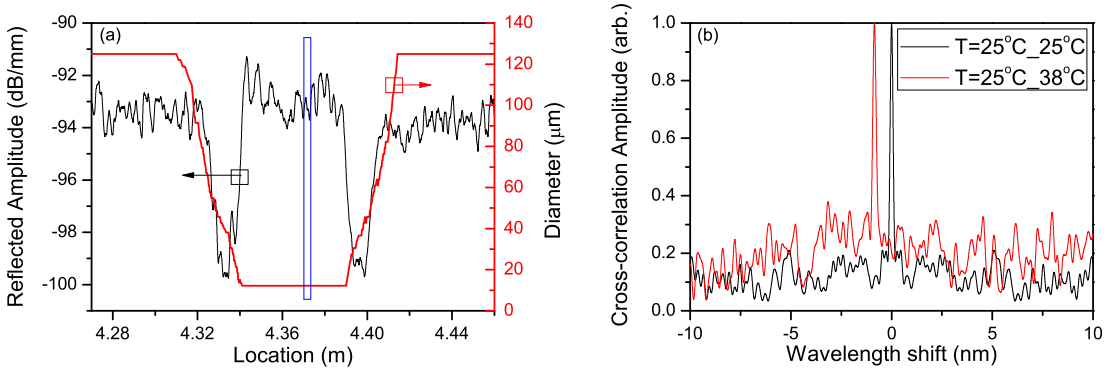

Figure 4.3: (a) Backscatter signal versus distance along the taper (left axis) and the cladding diameter of the taper (right axis). (b) Cross-correlation calculation of the spectra of the segment in the uniform taper range of non-annealed taper A (the blue window in (a)) with increasing temperature from 25°C to 38°C.

Figure 4.4 compares the thermal property of the non-annealed taper, annealed taper and SMF. From Fig. 4.4 (a), we observe that the non-annealed taper has the inhomogeneous thermal property. When the temperature increases, the wavelength shift of cross-correlation calculation is negative and decreases to ∼-0.9nm at the temperature of ∼40°C and then increases as the temperature increases. When the temperature decreases from 110°C to 30°C, the wavelength shift is a linear function of the temperature, with a negative slope. Then the taper is put in a closed oven at a constant temperature T=120°C. After 24 hours, the taper is slowly cooled to room temperature. Figure 4.4(b) indicates that the annealed taper has the same linear temperature dependence when the temperature increases or decreases. Comparing Figs. 4.4(b) and (c), the temperature sensitivity of the annealed taper is similar to that of SMF. After annealing, the inhomogeneous thermal property has been reduced significantly. Apparently, the residual stress from the taper process has been released by annealing treatment.

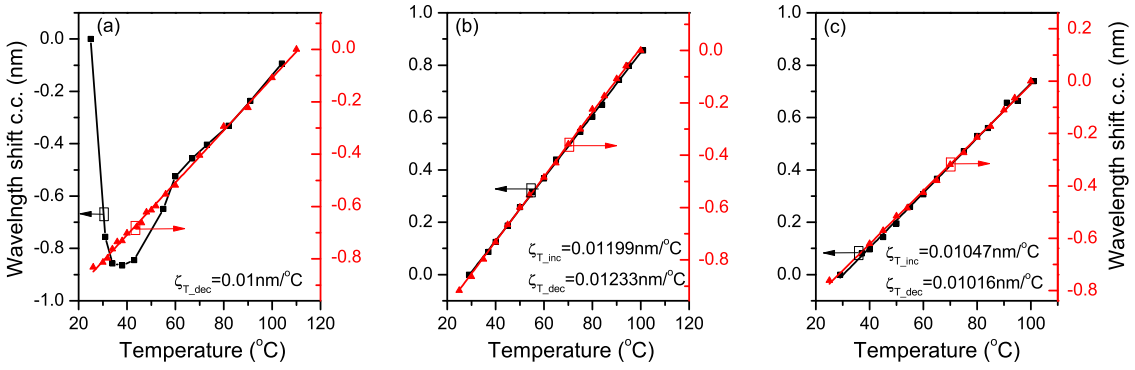

Figure 4.4: Wavelength shift vs. temperature for (a) non-annealed taper, (b) annealed taper, and (c) SMF, respectively. The left and right axes show the temperature increasing case and the temperature decreasing case, respectively. The samples are the experimental data and the linear curves are the fitting results.

Now we discuss the system resolution, including the spectral resolution and the spatial resolution. A larger window in OTDR-like curve includes more data points and gives better spectral resolution, but lower spatial resolution. There is a trade-off between spectral resolution and spatial resolution due to tuning range of the TLS and the sampling rate of DAQ. The OFDR measurement is performed 100 times at the room temperature and the standard deviation of cross-correlation calculation versus spatial resolution of OFDR system is plotted as a function of spatial resolution of OFDR system, as shown in Fig. 4.5(a). The standard deviation of the wavelength shift of cross-correlation measurement is as high as ∼17pm when the spatial resolution is ∼1mm. The standard deviation of wavelength shift is decreased to ∼3.94pm as the spatial resolution is ∼3.85mm. There is a trade-off between spatial resolution and standard deviation of the OFDR system. As an example, Fig. 4.5(b) displays the standard deviation of cross-correlation calculation of ∼3.94pm when the spatial resolution is set at ∼3.85mm, including 300 data points.

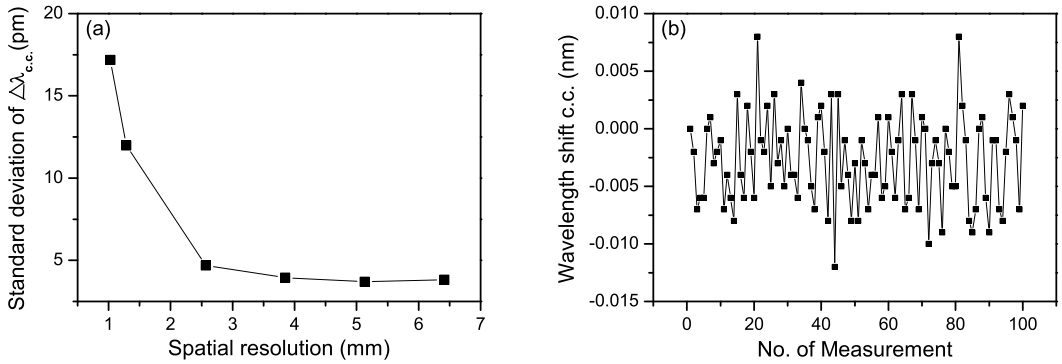

Figure 4.5: (a) The standard deviation of wavelength shift of cross-correlation calculation as a function of the spatial resolution. (b) The wavelength shifts of cross-correlation calculation over 100 measurements at the room temperature, when the spatial resolution is ∼3.85mm.

4.3.2 Mechanical properties

A section of the jacket-off fiber with a length of ∼19cm was stretched by using two translation stages at room temperature. A reference measurement was taken when the taper was in the initial state. Then the force measurement was taken when the fiber was stretched with a step of Δx. A ∼3.85mm window with 300 data points is applied along the OTDR-like curve and the spectrum response is obtained through inverse Fourier transform data processing. As discussed in previous subsection, the residual stress leads to inhomogeneous change of the refractive index. Tapers A, B and C are fabricated with different parameters and then all of these tapers are annealed. Taper A has a length of x_A=10.4cm and a uniform segment with diameter of d_{TaperU_A}=12.2μm and length of x_{TaperU_A}=4.9cm. The parameters for taper B and C are x_B=12.6cm, d_{TaperU_B}=7.8μm, x_{TaperU_B}=4.7cm, x_C=13.7cm, d_{TaperU_C}=6μm and x_{TaperU_C}=5.5cm. Using Eq. (4.9), we have γ_A=1.176, γ_B=1.205, and γ_C=1.127. Using Eq. (4.11), in theory, the uniform ranges of taper A, B and C should have ∼105, ∼257 and ∼434 times more strain than that of SMF.

A section of fiber (∼19cm) was stretched by a step of $1\mu m$. Using Eq. (4.10), the corresponding force step is 1.456×10^{-4}N. The measurement is performed with zero force applied to the fiber to produce a reference and again after a force has been induced. A ∼3.85mm window is applied at the location of 4.38m along taper A and as shown in Fig. 4.6(a), the increasing force results in a right-shifted main peak in the cross-correlation plot. Figure 4.6(b) shows the wavelength shift of cross-correlation calculation along the

whole taper length. In the taper region, compared with the zero force applied state, cross-correlation of the spectra reveals that the wavelength shift increases as the force applied on the taper increases. From Fig. 4.6(c), we observe that the taper with a smaller diameter has a higher force sensitivity. The force sensitivities of tapers A, B, and C are ζ_A =132.31nm/N, ζ_B=424.74nm/N and ζ_C=620.83nm/N, respectively. The resolution of the force measurement is related to the wavelength resolution of cross-correlation calculation in OFDR scheme. As mentioned in section 4.3.1, the standard deviation is optimized to ∼3.94pm as the spatial resolution is ∼3.85mm. Thus, the corresponding force resolutions are 29.78μN, 9.28μN and 6.35μN for tapers A, B and C, respectively. Figure 4.6(d) displays the force sensitivity along the uniform segments of these tapers. The force sensitivities fluctuate slightly along the whole uniform segment.

Now we increase the force level. Taper A was stretched with a step of 125μm, which corresponds to a step force of 0.0182N. Compared with a reference measurement, the sensing measurement is taken with an additional force of 0.0182N. Cross-correlation of the spectra reveals the wavelength shift between two conditions. Each wavelength shift data is calculated within a selected ∼3.85mm window along the OTDR-like curve. Figure 4.7(a) indicates that, in the first 12 states, the wavelength shift obeys a linear relationship with the applied force. When the force is larger than ∼0.2N, which is the elastic limit of the taper, the wavelength shift is not a linear function of the force. In the first 15 states, the wavelength shift of cross-correlation in the uniform range of taper shows the group index change of LP_{01} mode. The wavelength shift between states 15 and 16 shows

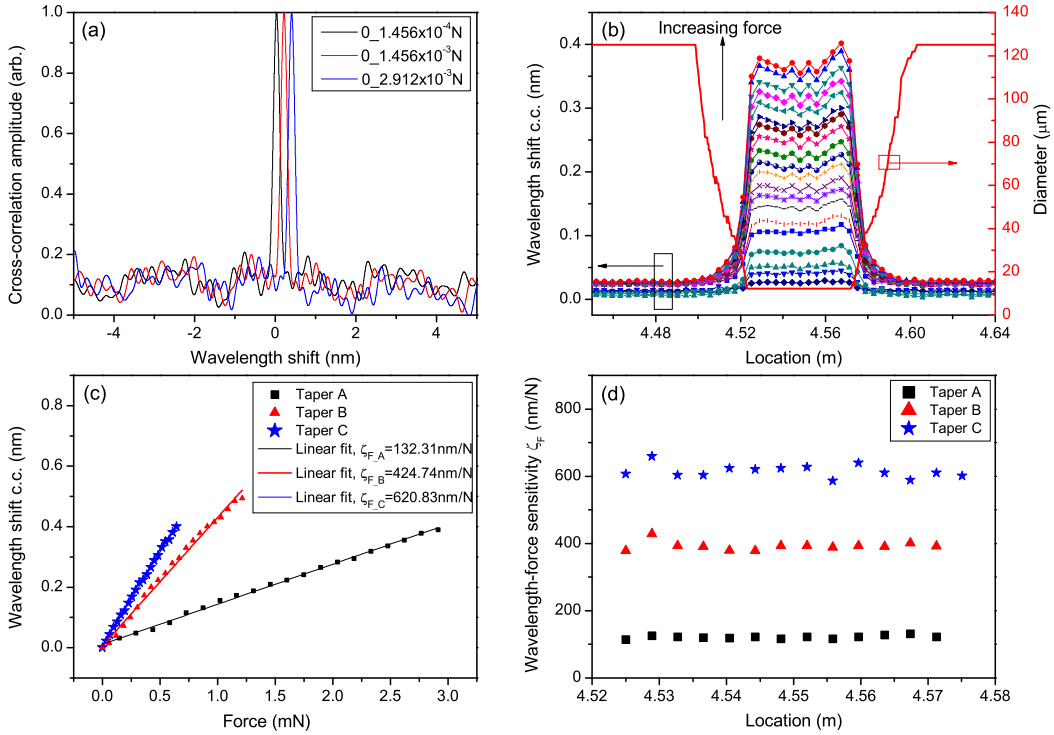

Figure 4.6: (a) Cross-correlation calculation of the spectra of the segment in the uniform taper range between the zero force applied state and three increasing force applied states. (b) Wavelength shifts of cross-correlation calculation along the taper length as the force increases (left axis), and the cladding diameter of taper A (right axis). (c) Wavelength shifts as a function of force in the case of tapers A, B and C. The samples are the experimental data and the curves are the linear fitting results. (d) The force sensitivities along the uniform segments of these tapers.

negative values. It means that the taper starts to be deformed in transverse direction in state 16, with a 0.2912N-force applied. The energy in original dominating mode LP_{01} is redistributed to higher-order modes; hence correlation between different modes gives negative values, while correlation results of the same mode show positive correlation. It is because higher-order modes have lower group indices [72]. Then the cross-correlation

wavelength shifts in states 16-19 become positive again because they show the group index change of the same higher-order mode, which has most energy in these states. The energy coupling between higher-order modes happens again in states 19 and 20, with negative cross-correlation wavelength shifts. The wavelength shift-force sensitivities for different modes are different. Linear fitting in separated ranges find that LP_{01} mode has a force sensitivity of 124.27nm/N, higher-order modes have sensitivities of 48.39nm/N and 18.15nm/N, respectively. In order to avoid the deformation of fiber and regard its diameter as a constant, the fiber taper should be used as an accurate force sensor in the range of milli or micro newtons. Here we only test the tapers with reversible mechanical perturbations, and consider the force sensitivity of LP_{01} mode. Reference [63] showed the experimental result of $\frac{\Delta\lambda_{c.c}}{\lambda} = 0.7314\Delta\varepsilon$, which results in a wavelength shift-strain sensitivity of $\zeta_\varepsilon = \frac{\Delta\lambda_{c.c}}{\Delta\varepsilon} = 0.73141\lambda$=1.13pm/$\mu\varepsilon$, here λ =1540nm. We transform it to the wavelength shift-force sensitivity by using

$$\zeta_F = \frac{\Delta\lambda_{c.c}}{\Delta F} = \frac{\Delta\lambda_{c.c}}{\Delta\varepsilon}\frac{\Delta\varepsilon}{\Delta F} = \frac{\zeta_\varepsilon}{EA} = \frac{4\zeta_\varepsilon}{\pi E d_{SMF}^2} \tag{4.12}$$

and the force sensitivity of SMF is 1.25nm/N. In our experiment, as shown in Fig. 4.7(b), SMF has a force sensitivity of 1.29nm/N, which is similar to the reference value. Compared with SMF, the taper is ∼96 times more sensitive, which is equivalent to 124.27nm/N. The optimization ratio is comparable to the theoretical strain ratio between taper A and SMF (∼105). Figure 4.7(b) displays distributed force sensitivity along the

whole taper fiber. There is small force sensitivity fluctuation along the uniform segment of taper A. Fluctuation of flame temperature during the tapering process results in inhomogeneities of geometric structure and mechanical strength of the taper. Hence, the inhomogeneity of geometric structure causes the inhomogeneous refractive index distribution in the taper.

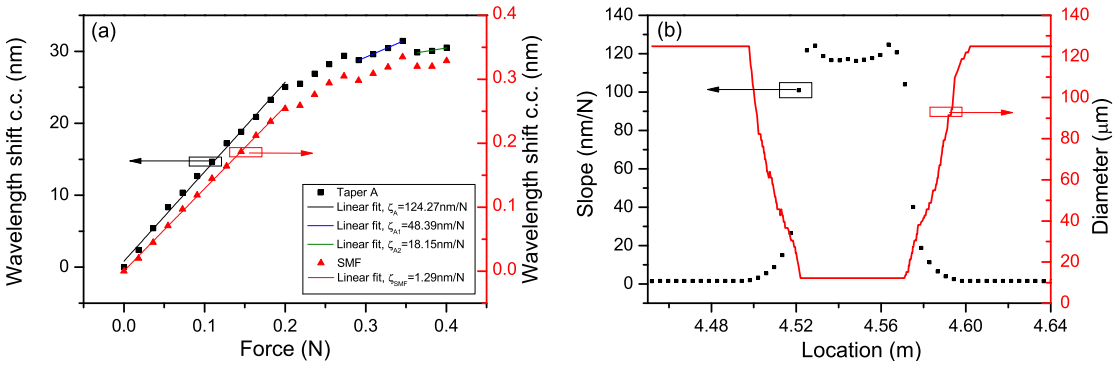

Figure 4.7: (a) Wavelength shifts as a function of force for the uniform segment of taper A (left axis) and SMF (right axis). The samples are the experimental data and the curves are the linear fitting results. (b) The force sensitivities along the fiber (left axis) and the cladding diameter of the gently taper A (right axis).

Taper B was tested with a stretched step of $125\mu m$. The total length of the stretched fiber is ∼19cm. The cross-correlation of the spectra reveals the wavelength shift between two states with an additional force of 7.574×10^{-3}N applied. Figures 4.8(a) shows that the wavelength shift obeys a linear relationship with the applied force. There is no new spatial mode generation. Figure 4.8(b) displays force sensitivity along the fiber. The uniform range of taper B obtains a force sensitivity of 339.89nm/N, which is ∼279 times higher than that of SMF, over a force range of 0–0.07N. The optimization ratio is close to the theoretical strain ratio between taper B and SMF (∼257).

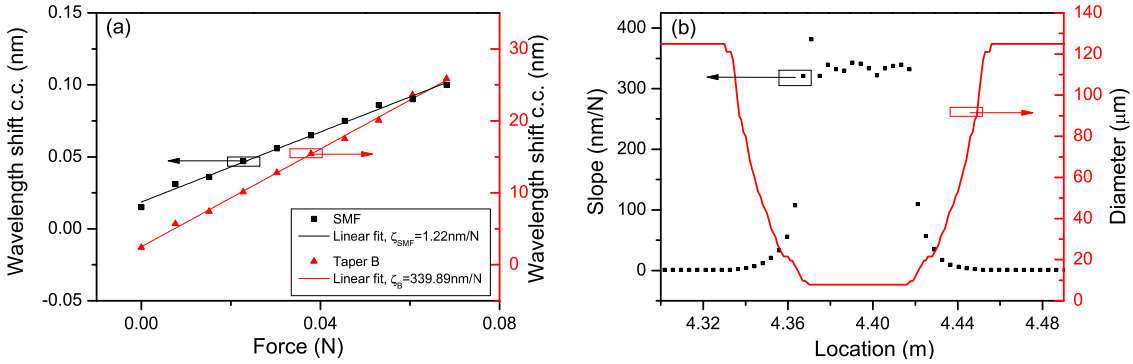

Figure 4.8: (a) Wavelength shift as a function of force for SMF (left axis) and uniform segment of taper B (right axis). The samples are the experimental data and the curves are the linear fitting results. (b) The force sensitivity along the fiber (left axis) and the cladding diameter of taper B (right axis).

4.4 Conclusion

In conclusion, we present the thermal and mechanical properties of tapered SMFs by using high-resolution, high-sensitivity OFDR technique. The cross-correlation spectral shifts induced by thermal or force in the uniform region of fiber taper indicate the group index change of the dominating fundamental mode. The annealed fiber taper will relieve its internal stress due to the tapering process and obtains similar homogeneous temperature coefficient to that of SMF. Therefore, annealing is regarded as an important treatment. It was also demonstrated experimentally that a fiber taper with a reduced waist diameter obtains high wavelength-force sensitivity. One can use a fiber taper with a designed waist diameter as a micro-force sensor.

Chapter 5

Distributed birefringence of tapered polarization-maintaining fibers with OFDR

This chapter presents polarization preserving character of tapered polarization-maintaining fibers (PMFs), which is evaluated by OFDR-based distributed birefringence along tapered PMFs. Section 5.1 introduces the research background and section 5.2 presents the experimental results.

5.1 Introduction

Tapering is a useful technique to enhance evanescent field, as well as to increase the power density at beam waist for research on nonlinear effect. Polarization-maintaining

fibers (PMFs) have unique polarization-preserving character and tapered PMFs may find use in many micro-/nanophotonics applications and devices, such as high-quality microresonators, high-performance optical sensors, and microlasers and so on. When tapering a PMF, one should observe how the polarization state of linearly-polarized light waves launched into the PMF is maintained during propagating along the fast and slow axes of the taper region. In the case of stress-induced high-birefringence PMF, such as Panda fibers, it is important to maintain both the internal stress and the refractive index profiles as required to preserve polarization during tapering process. This is because the tapering process could release stress in fast and slow axes leading to coupling between both axes, which makes tapered PMFs lose the polarization-maintaining property. In addition, if core taper angle is over the adiabaticity criterion [1], the taper becomes non-adiabatic and generates higher-order modes besides the fundamental mode. These features can be accurately monitored by distributed mode coupling measurement along the taper region. Polarization extinction ratio (PER) is defined as the optical power ratio of two polarization states with maximum power P_{max} and at the orthogonal axis with minimum power P_{min}. Such a definition works for PMFs with constant axes. However, for tapered PMFs with changed profiles along propagation direction, PER must be measured at every location of tapered PMFs. Alternatively one can use polarization analysis technique to measure input and output state of polarization (SOP) at every position of a tapered PMF. Both techniques require a cutback method at every ∼1cm, which is comparable to a beat length of PMFs. This is impossible, as a device cannot be re-used

and each device has slightly different birefringence property. A distributed birefringence measurement technique is required to characterize the birefringence change in up- and down-tapers, as well as uniform waist taper region by comparison with a PMF.

A PER of 16dB was obtained when a commercial Panda fiber (Nufern Inc. PM 1550HP) was tapered into a microfiber with a waist diameter of $\sim 1\mu$m, while a conventional PMF has a PER of 30dB [75]. The decreasing of PER and its relation to the decreasing of birefringence have not been studied before, especially distributed birefringence change along taper PMFs.

In order to investigate the distributed mode coupling change along tapered PMFs, a high-resolution Optical Frequency-domain Reflectometry (OFDR) system [49, 72] is employed to measure distributed birefringence of tapered PMFs. The birefringence change in tapered single-mode fiber (SMF) has been demonstrated in [72]. In SMF tapers, the birefringence is increased in the taper region due to low refractive index of cladding modes. This is not the case for tapered PMFs and the birefringence of tapered PMFs is decreased due to the stress release of the taper process [76–79], especially at small beam waist. The distributed birefringence, which is defined as the refractive index difference between the fast and slow modes, is measured along tapered PMFs with a spatial resolution of $\sim$1.25cm. With a waist diameter of 80μm, there are only fast and slow modes within the taper region and the birefringence of the tapered PMF is slightly reduced from 3.28×10^{-4} to 2.86×10^{-4} at the taper waist. The fast/slow axes are constant and the SOP of the launched light is maintained. Therefore, the PDL of this kind of tapered

PMFs has low wavelength dependence, which is similar to that of PMFs. In the case of waist diameters of 60μm and 40μm, higher-order modes are generated in the taper region. The fast/slow axes are changed and the SOP of the launched light varies. The polarization-maintaining property of tapered PMFs is lost. Hence, PDLs of this kind of tapered PMFs increase and has high wavelength dependence. Compared with PERs, the PDLs and distributed birefringence measurement provide more accurate information on the polarization maintaining property.

5.2 Experimental results

The experimental setup to measure Rayleigh backscatter as a function of fiber length is described in Fig. 3.1. The fiber under test (FUT) is three tapered PMFs (PM1550, Panda, Corning) fabricated by a fiber glass processing system (GPX-3400, Vytran LLC). Taper A has a length of L_A=4.5cm, a uniform waist segment with diameter of $d_A \sim 80\mu$m, and a length of ℓ_A=3cm. The parameters for taper B and C are L_B=5.2cm, d_B=60μm, ℓ_B=3.1cm; L_C=5.23cm, d_C=40μm, ℓ_C=3.08cm.

Figures 5.1(a) and (b) present distributed birefringence and cladding diameter as a function of the taper length for tapers A and B, respectively. Autocorrelation is calculated within a 1.25cm-subsection along the fiber length. It is noted that the window width must be larger than the beat length of a Panda PMF (3.0–5.0mm) [76]. The insets display autocorrelation plot of the spectra at the waists. It is found that taper A keeps high birefringence along the taper region while the birefringence is decreased slightly

from 3.28×10^{-4} to 2.86×10^{-4} at the taper waist. By contrast, the birefringence of taper B is reduced by a factor of ∼5 at the taper waist. The mode coupling is observed in the form of significantly decreased birefringence. In order to further examine the

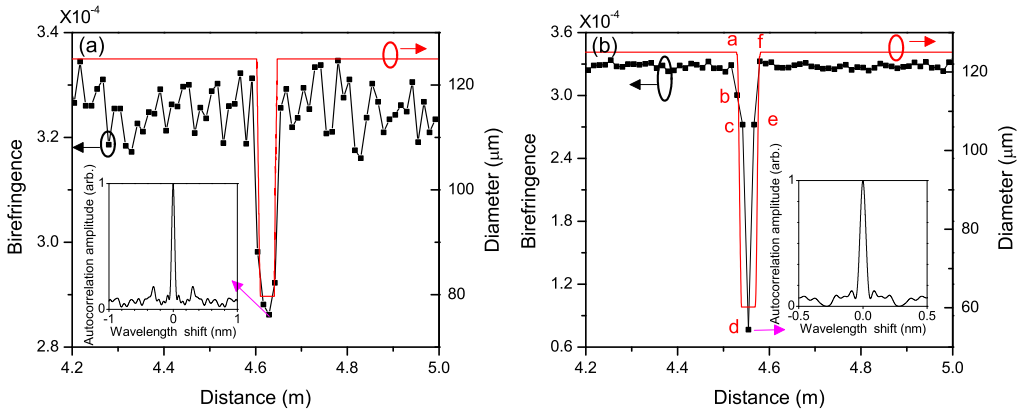

Figure 5.1: (a) Distributed birefringence along taper A (left axis) and its cladding diameter (right axis). (b) Distributed birefringence along taper B (left axis) and its cladding diameter (right axis). The insets are autocorrelation calculation of the spectra at the taper waists.

distributed birefringence change of taper B, autocorrelation calculations of the spectra at the corresponding positions of points a-f in Fig. 5.1(b) along taper B are illustrated in Figs. 5.2(a)-(f). At position a, taper B has high birefringence and energy is mainly distributed in the fast and slow modes. If we assume the slow mode has more energy, the normalized autocorrelation amplitude of side peaks in Fig. 5.2(a) mean the energy ratio between the fast and slow modes. When the diameter of taper A decreases, the amplitude of Rayleigh backscatter decreases which indicates the energy redistribution among new modes excited by tapering in addition to original fast and slow modes. The higher-order modes can be illustrated by side peaks close to the central peak in Fig.

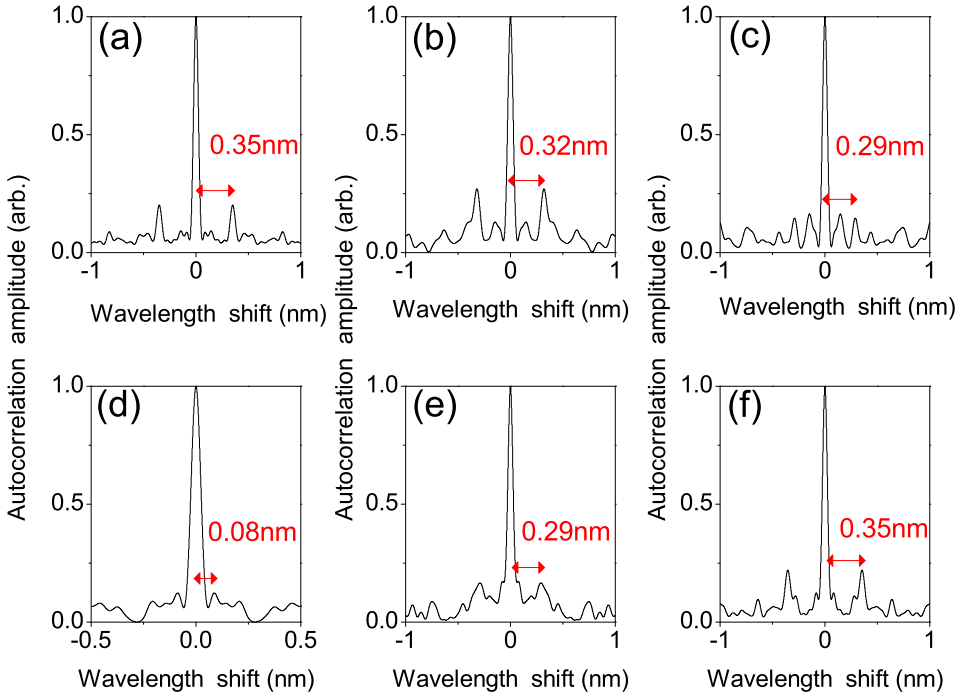

Figure 5.2: (a)-(f) Autocorrelation calculations of the spectra of five segments within the taper region and their corresponding birefringence and location are marked as a-f in Fig. 5.1(b).

5.2(b). Comparing Figs. 5.2(a)-(c), the change of relative amplitudes of side peaks represents energy redistribution among the fast and slow modes and higher-order modes. In addition, the birefringence is reduced along the down-taper region, at positions a, b, and c as 3.29×10^{-4}, 3×10^{-4}, and 2.72×10^{-4}, respectively. Figure 5.2(d) indicates the minimum birefringence 7.7×10^{-5} at the taper waist. In the up-taper region, as shown in Figs. 5.2(e) and (f), the energy couples back from higher-order modes to the fast and slow modes and the birefringence increases.

As shown in Fig. 5.3(b), the birefringence of taper C is reduced by a factor of 5

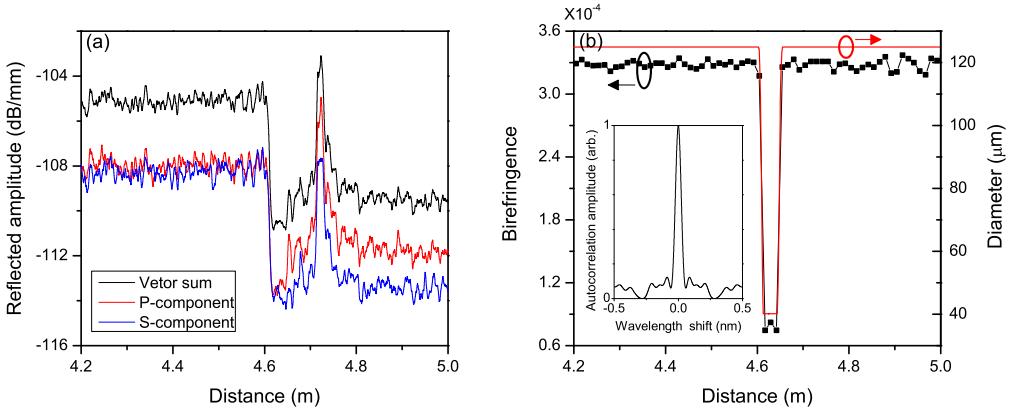

Figure 5.3: (a) Backscatter amplitude versus distance along taper C. (b) Distributed birefringence along taper C (left axis) and its cladding diameter (right axis). The inset is autocorrelation calculation of the spectrum at the taper waist.

within the taper waist region. Taper C has a similar energy redistribution process to that of taper B and a longer coupling length. Figure 5.3(a) illustrates the OTDR-like curves, which have been smoothed using a low-pass filter (LPF) with an effective spatial resolution of ∼4.1mm. The scatter level drops by ∼6dB at taper C. As we mention in previous paragraph, it reveals that energy is coupled from the fast and slow modes to higher-order modes generated via tapering. Before taper C, the p- and s-components of Rayleigh backscatter of the PMF have same scatter level because the light is launched at 45^o to the fast and slow axes; after taper C, the scatter level difference between the p- and s-components is ∼2dB, because the fast and slow axes of PMF varies among the taper region and the SOP of the launched light is not preserved along taper C. The decreasing of scatter level is ∼2dB and ∼0dB for tapers B and A, respectively, and the scatter level difference between p- and s-components of Rayleigh backscatter before and after the taper are ∼1dB and ∼0dB, which reveals different polarization preserving character

and mode coupling process for tapers B and A.

PERs of the PMF and tapers A, B, and C are measured by using a polarization beam splitter (PBS) and the results are ∼41dB, ∼34dB, and ∼27dB, respectively. It seems that all these fibers have high polarization preservation abilities. However, based on the distributed birefringence measurement by using OFDR, mode coupling within the tapered PMFs is revealed. We choose different window width to perform autocorrelation calculation and obtain average birefringence over the whole taper region and average birefringence over the uniform waist region of the tapered PMF, which are noted as B_1 and B_2. These parameters of a PMF and tapers A, B, C are listed in Table 5.1. High birefringence of taper A demonstrates that SOP of the launched light is maintained along the whole taper. In the case of tapers B and C, B_1 shows average birefringence over the taper region, while these tapers have weak polarization preservation abilities within the waist region of the tapered PMFs. The mode coupling is presented in the form of significantly decreased birefringence.

PDL is defined as the ratio of the maximum and minimum transmission of an optical device with respect to all polarization states. By employing a TLS, a polarization

Table 5.1: Measured distributed birefringences of PMF and tapered PMFs.

	PMFs	Tapered PMFs		
		Taper A 80μm	Taper A 60μm	Taper C 40μm
B_1	3.28×10^{-4}	2.93×10^{-4}	2.9×10^{-4}	2.9×10^{-4}
B_2	3.28×10^{-4}	2.89×10^{-4}	2.54×10^{-5}	3.29×10^{-5}

scramble and a power meter, the PDLs of tapers A, B, and C are measured as a function of wavelength. The results are shown in Fig. 5.4. It is noted that the PDL of a tapered PMF increases as its waist diameter decreases. The large PDLs for tapers B and C also apparently indicate their poor polarization preserving characters.

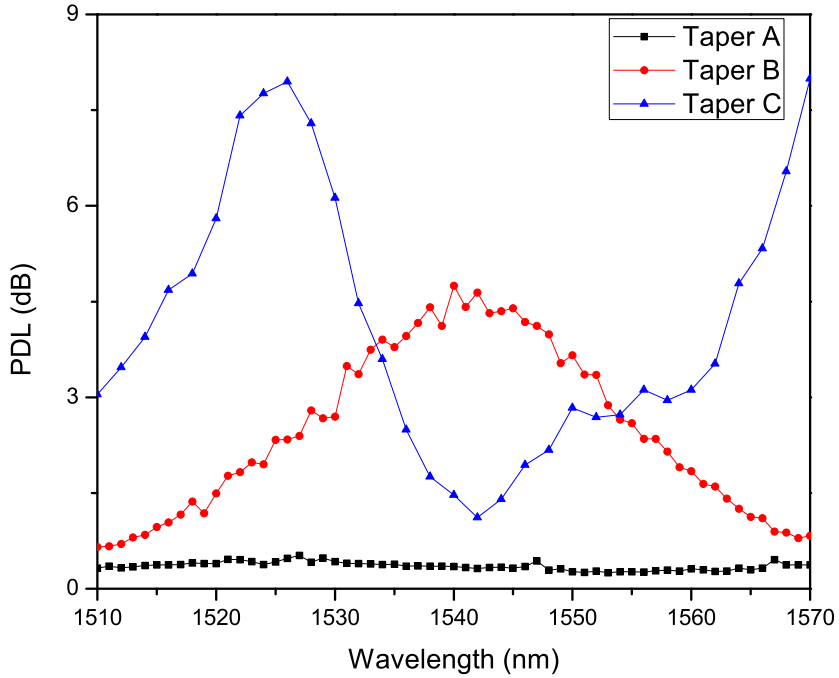

Figure 5.4: PDLs of tapers A, B, and C as a function of wavelength.

5.3 Conclusion

In summary, we measure distributed birefringence along tapered PMFs by using a high-resolution OFDR system. Autocorrelation data processing reveals mode coupling be-

tween the fast and slow modes and higher-order modes excited in the tapering process along the taper region. With a waist diameter of 80μm, the SOP of the launched light is maintained and the birefringence of the tapered PMF is reduced from 3.28×10^{-4} to 2.86×10^{-4} at the taper waist. In the case of the tapered PMFs with waist diameter of 60μm and 40μm, respectively, significant mode coupling is investigated in the form of reduced birefringence by a factor of 10 at the taper waists. The measured PDL of a tapered PMF increases as the waist diameter decreases. Compared with PER, this approach provides more accurate information on the polarization preserving character.

Chapter 6

Tunable fiber laser using a tapered fiber tip

This chapter presents a simple and cost-effective tunable ring laser, which is tuned by the spatial modes of a tapered single-mode fiber (SMF) tip acting as a tunable bandpass filter. Section 6.1 discusses the research background. Section 6.2 introduces the principle of fiber lasers, including gain medium, cavity losses and mode-selecting mechanism; section 6.3 investigates the characteristics of tapered fiber tip filters and section 6.4 discusses the laser setups and optimization of laser parameters, such as the side-mode suppression ratio (SMSR), bandwidth, and tuning range, by means of changing the relaxation time and gain of amplifiers, as well as the steepness of fiber tips. Section 6.5 proposes two more chemical polish techniques to improve the performances of the laser.

6.1 Introduction

Cost-effective tunable lasers have extensive applications in wavelength division multiplexing optical communication and multiplexing of fiber sensors based on fiber Bragg gratings (FBGs). Tunable optical bandpass filters are essential components in tunable lasers. Filter features include wide tuning range, high SMSR, narrow optical passband, small size, and low cost. Currently, single-passband tunable optical filter techniques include FBGs [30–32], in-line Fabry-Perot (FP) filters [33], arrayed waveguide gratings (AWGs) [34] and so on. Optical filters made by FBGs can be tuned by either thermal or mechanical stress effects. However, the temperature sensitivity of FBG ($\sim$10pm/°C) limits the measurement accuracy of the wavelength shift to a nanometer region. An FBG filter based on piezoelectric stack actuators works over a tuning range of 45nm, while its 3dB bandwidth reaches 0.7nm [30]. FP filters have bandwidths in the range of tens of megahertz to tens of gigahertz, but they are rather expensive and their tuning ranges are limited to less than 1nm because their cavity lengths are changed by piezoelectric techniques. AWGs themselves are not tunable and they need to be combined with additional switching devices to achieve tunability. A polymeric AWG multiplexer has a tuning range wider than 10nm with a temperature change of 55°C [34], while its 3 dB bandwidth is 0.2nm. Therefore, none of these optical filters has a tunable narrow bandwidth (picometer resolution) over a wide tuning range (a few nanometers or more).

Optical interference fringes are usually obtained by splitting one single light beam into two or several beams using a beam splitter, and letting the beams interfere with each

other using a beam combiner. The small size of tapered SMF tips (from micrometers to nanometers) results in the generation of cladding modes in SMFs. Due to the multibeam interference of the cladding modes in the near field, tapered fiber tips are proposed to be near-field, easy-handling, and high resolution filter devices [80]. The object of this chapter is to build a simple and cost-effective tunable ring laser that is tuned by the spatial modes of a tapered SMF tip acting as a tunable bandpass filter. This is an extension of the work reported in Applied Physics Letters [80]. We optimize the laser parameters, such as SMSR, bandwidth, and tuning range, using different optical amplifiers, including semiconductor amplifiers (SOAs), L-band erbiumdoped fiber amplifiers (EDFAs), and C-band EDFAs inside the fiber ring. The ring laser can achieve a high SMSR, a tunable narrow bandwidth, and a wide tuning range.

6.2 Principle of fiber laser

Classical solid state lasers consist of a bulk crystal or glass gain medium pumped by a flash lamp or diode lasers. The beam propagates in free space through the gain medium with standard free space optics such as flat mirrors, lenses, and diffraction gratings to control the beam. The high performance of this type of laser comes at the cost of strict spatial alignment condition. Its disadvantages also include high cost and large dimension. By contrast, semiconductor lasers are cheap and compact and feature a wide range of limitations, such as high frequency noise. Compared with these lasers, fiber lasers, in general, have more advantages, including compact size, low cost, high optical quality,

high stability and reliability. Another advantage is that fiber lasers are easy to connect to other fiber systems. The theory behind lasers has been well established [81, 82]. Here we give a brief description of the theory behind the fiber laser, by examining its gain medium, cavity losses, and mode-selecting mechanism.

6.2.1 Gain medium

Many different rare-earth elements, such as erbium, ytterbium, neodymium, dysprosium, praseodymium, and thulium, can be used to dope the fiber core during the manufacturing to prodece a gain medium. Erbium-doped fibers (EDFs) have attracted the most attention because they operate in the wavelength region near 1550nm [82, 83]. Most of the fiber lasers presented in this thesis employ EDFs as the gain medium. Figure 6.1(a) shows the absorption and emission cross-sections of erbium-doped silica and their physical meanings are absorption and emission efficiencies as the functions of the wavelength. The optical pumping scheme in an EDF is usually described by a simplified three-level energy system as illustrated in Fig. 6.1(b). An EDF can be pumped at a wavelength of 980nm, which corresponds to the bandgap between the excited state and the ground state, to create a population inversion. The carriers stay in the excited state for only about 1ms, and after that they decay into a metastable state through a nonradiative transition. In this process, the energy loss is turned into mechanical vibrations in the fiber. The energy band of the metastable state extends roughly from 0.8eV to 0.84eV, which correspond to a wavelength band from 1480nm to 1550nm. Within the metastable

energy band, carriers tend to move down from the top of the band to somewhere near the bottom through intraband relaxation. Finally, radiative recombination occurs when carriers step down from the bottom of the metastable state to the ground state and emit photons in the 1550nm wavelength region. The carrier lifetime in the metastable state is on the order of 10ms, which is much longer than the carrier lifetime in the excited state. Therefore, with constant optical pumping at a wavelength of 980nm, almost all the carriers will accumulate in the metastable state. An EDF can also be pumped at a wavelength of 1480nm. In this case, 1480nm pump photons excite carriers from ground state to the top of metastable state directly. Then these carriers relax down to the bottom part of the metastable band. Typically, 1480nm pumping is more efficient than 980nm pumping because it does not involve the nonradiative transition from the 980nm to the 1480nm band. Therefore, 1480nm pumping is often used for high-power optical amplifiers. However, amplifiers with 1480nm pumping usually have 1dB higher noise figures than 980nm pumping [2]. Erbium ions can be pumped at 1480nm and amplified near 1550nm because at 1480nm the absorption cross-section σ_a is larger than the emission cross-section σ_e, whereas for longer wavelength, σ_e is comparable to or larger than σ_a (see Fig. 6.1(a)). However, because of stimulated emission at the pump wavelength, complete inversion cannot be achieved for 1480nm pumping. As a result, noise figure less than 4dB cannot be achieved even with high pump powers, whereas noise figure approaching the 3dB quantum limit can be achieved for 980nm pumping.

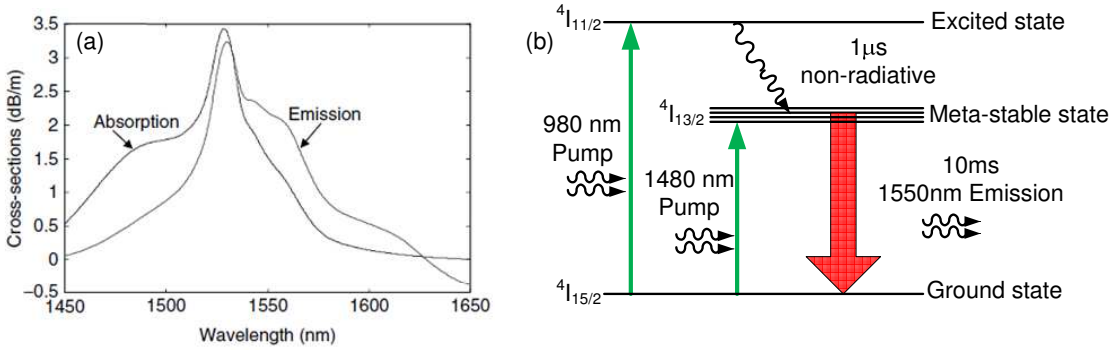

Figure 6.1: (a) Absorption and emission cross-sections for Er^{3+}-doped silica [2]. (b) Energy-level diagram of erbium ions in silica fibers.

6.2.2 Cavity losses

In the steady state, the gain per round trip should exactly cancel the cavity losses per round trip. Hence it is important to take into account the cavity losses. Propagation losses inside the fibers are usually negligible, but we need to consider the losses at intersections between different fibers, and especially in the presence of components such as wavelength division multiplexers (WDMs), couplers, isolators and so on. In fiber lasers, a 10–20dB gain per round trip is reasonable, which is much larger than the gain expected in some kinds of lasers, such as solid state lasers. Hence much higher cavity losses are acceptable in fiber lasers. Cavity losses should be minimized, as high losses result in smaller laser outputs.

6.2.3 Mode-selecting mechanism

First, dense longitudinal modes are generated due to long ring cavity length L. The mode spacing $\triangle v$ is given by

$$\triangle v = \frac{c}{nL}, \tag{6.1}$$

where c is the velocity of light in vacuum and n is the refractive index of fiber. Secondly, a mode selection filter or a combination of filters are employed. Common methods include multiple subring-cavities combined with either an FBG [84] or with an intracavity FP filter [85], and a saturable absorber combined with either a tunable FBG [86, 87] or with an FP filter [88, 89], and a tunable FBG FP etalon [90, 91]. If the mode selection device has a high SMSR, sometimes a stable solution can be found in a few round trips, but if the effect is weak, more round trips may be needed. Because the mode spacing is dense due to long cavity length, it is hard to find an ultra-narrow bandpass filter. In order to select mode effectively, we need to increase the round trip number. The number of round trips is limited by the ratio of fluorescence relaxation time of the gain medium, e.g. EDF ($\sim$10ms), and round trip time ($\sim$100ns) in the cavity. Finally, a single longitudinal mode (SLM) is achieved.

6.3 Tapered fiber tip filter

6.3.1 Principle

A tapered SMF tip is fabricated from an SMF using a heating and fast stretching technique [40, 41]. As described in Chapter 2, a fiber tip with a parabolic profile is formed due to the surface tension of the fused silica. For tips with rather gentle slopes, the propagation process is adiabatic [1]. However, when the slopes of the tips are steep due to the fast drawing, the tapered fiber tips are nonadiabatic. Figure 6.2 shows two representative tapered fiber tips used in the experiment. Tip A has a small slope, and tip B has a large slope. Different tip profiles lead to different spectral characteristics and filter properties. The measured lengths of the tapered tips A and B are 3.05mm and 2.74mm, respectively. The diameters of the tip ends are 3μm and 3.4μm, respectively.

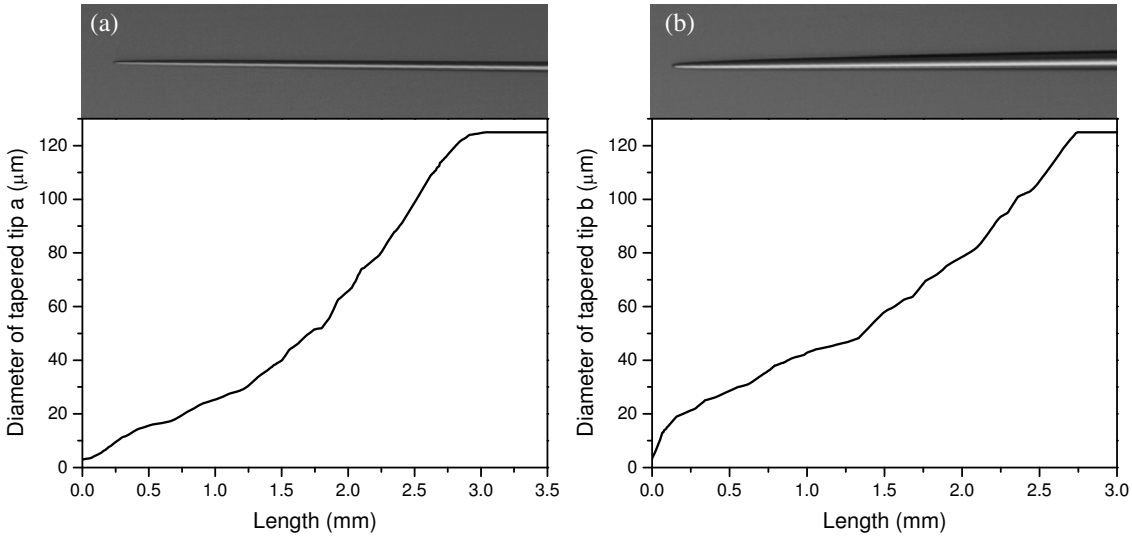

Figure 6.2: (a) (b) Camera pictures of two representative tapered fiber tips A and B, and their corresponding cladding diameter curves.

The basic principle of tapered fiber tip filters depends on multibeam optical interference. At the beginning of the taper, only the fundamental mode linearly polarized (LP) mode, LP_{01}, propagates in the fiber. When the core diameter is decreased during tapering, the effective index n_{eff} of the core mode decreases continuously. When $n_{air} < n_{eff} < n_{cl}$, the core mode is "cut off" [1, 29]. At this point, cladding modes are generated, which propagate with the fundamental mode along the length of the fiber. The transition value $V_{core/cladding}$ for the fundamental mode is obtained from Eq. (2.7). SMF-28^{TM} fibers with a core diameter of 8.2μm and a cladding diameter of 125μm have a ratio of cladding to core diameter $S = 15.24$. We have $V_{core/cladding} = 0.82$. Here, we assume the ratio S remains constant under tapering. This means that the fundamental core mode is split into several cladding modes when the fiber is tapered down to a cladding diameter of 51.1μm in the experiment. Intermodal beating among these cladding modes has been observed in previous studies [17, 27, 92].

For tips A and B, the local taper angles are apparently larger than the critical taper angle mentioned in Chapter 2. Therefore, significant mode coupling and large power transfer take place. Power is transferred from LP_{01} to higher-order modes (LP_{02}, LP_{03}, ...) by mode coupling effects [8]. As the end of the tip is approached, the number of cladding modes decreases, and some cladding modes are emitted outside of fiber. Energy in these modes eventually leaks out of the fiber. When the cladding diameter of the tip $D = 5\mu$m, seven cladding modes are generated in the fiber tip. When D is reduced to 4μm, the number of cladding modes is five. When D is 3.4μm and 3.3μm, the number

of cladding modes varies in the L-band wavelength. When D is less than 3.2μm, only LP_{01}, LP_{02}, and LP_{03} can be transmitted in the fiber tip. As shown in Fig. 6.3(b), the number of cladding modes remains constant in the short wavelength range. The number decreases as the wavelength increases. The critical wavelengths for LP_{04} and LP_{05} are 1604nm and 1596nm, respectively. Previous theoretical work and experimental data have both shown that the number of cladding modes reduces when a fiber is tapered down [29].

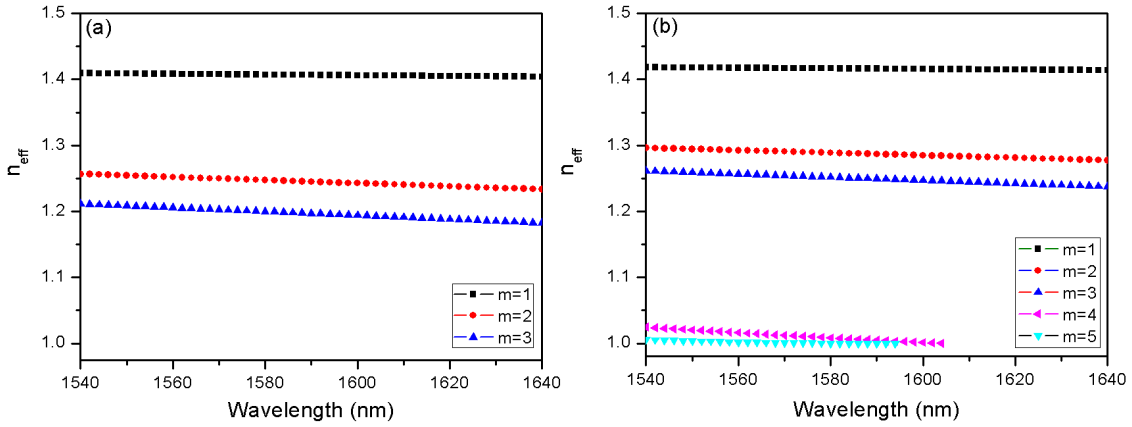

Figure 6.3: Effective refractive index of LP_{0m} mode in different tapered SMF tips with diameters (a) 3μm and (b) 3.4μm, respectively.

If only considering two dominant modes, the interference is given by

$$I = I_1 + I_2 + 2\sqrt{I_1 I_2}\cos\phi, \tag{6.2}$$

with

$$\phi = \frac{2\pi\Delta nL}{\lambda}, \tag{6.3}$$

where ϕ is the phase difference accumulated over a physical length L; I_1 and I_2 are the powers distributed in the lower-order and higher-order dominant modes, respectively; $\Delta n = n_1 - n_2$ is the refractive index difference of these two modes and λ is the wavelength of light in vacuum.

The extinction ratio, ER, of the interferometer is defined as

$$ER = 10 \lg(\frac{1 + \sqrt{\frac{I_2}{I_1}}}{1 - \sqrt{\frac{I_2}{I_1}}})^2. \tag{6.4}$$

Figure 6.4 shows the extinction ratio as a function of the power ratio $\frac{I_2}{I_1}$ of the two interfering modes with $\frac{I_2}{I_1} < 1$. It can be seen that larger power ratio of $\frac{I_2}{I_1}$ gives rise to a higher extinction ratio.

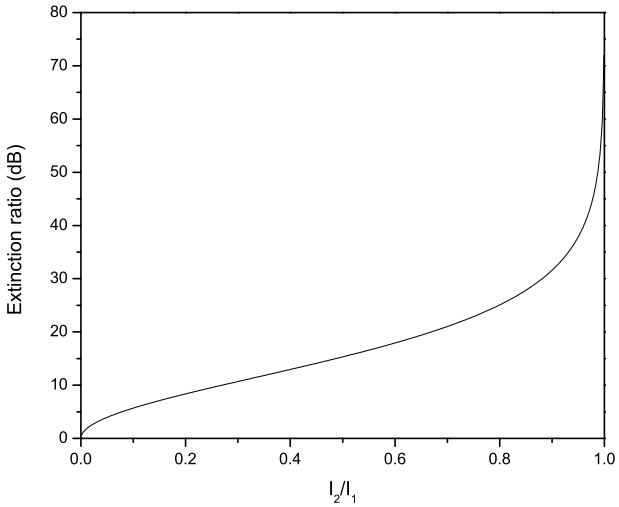

Figure 6.4: Extinction ratio as a function of the power ratio $\frac{I_2}{I_1}$ of the two interference modes.

Since the interference spectrum is obtained over a wavelength range, it must be described using the center wavelength λ_0 and the deviation from it, $\Delta\lambda$ ($\Delta\lambda \equiv \lambda - \lambda_0$). Taylor expanding of Eq. (6.2) at the center wavelength λ_0 and taking only the first order term gives

$$\begin{aligned}\phi \simeq & 2\pi\Delta nL\left(\frac{2}{\lambda_0} - \frac{\lambda}{\lambda_0^2}\right) \\ = & \frac{4\pi\Delta nL}{\lambda_0} - \frac{2\pi\Delta nL}{\lambda_0^2}\Delta\lambda \quad \left(\text{let } \phi_0 = \frac{4\pi\Delta nL}{\lambda_0}\right) \\ = & \phi_0 - \frac{2\pi\Delta\lambda}{\lambda_0^2}\Delta nL. \end{aligned} \tag{6.5}$$

To be more general, the dispersion of the guided mode is taken into account and Δn should be replaced with the differential modal group index Δm [70], which leads to

$$\phi = \phi_0 - \frac{2\pi\Delta\lambda}{\lambda_0^2}\Delta mL, \tag{6.6}$$

with

$$\Delta m = \Delta n - \lambda_0\frac{\partial\Delta n}{\partial\lambda}. \tag{6.7}$$

A sinusoidal interference pattern represented mathematically Fourier transform of the interference spectrum reveals a peak in the spatial frequency spectrum with spatial frequency value ξ with units of nm^{-1}, which is defined as [93]

$$\xi = \frac{\Delta mL}{\lambda_0^2}. \tag{6.8}$$

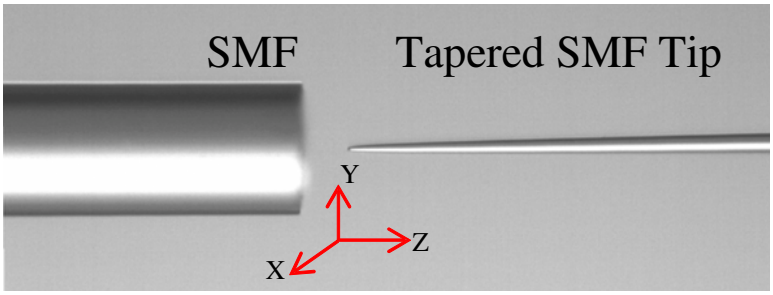

Figure 6.5: Camera picture of a fiber tip and an SMF acting as a probe. The left is one free end of the probe fiber with a cladding diameter of 125μm; the right is the tapered SMF tip B with a diameter of 3.4μm.

The spatial frequency is proportional to the interferometer length L and related to the differential modal group index Δm between two interference modes. The presence of more than one peak in the frequency spectrum indicates that many cladding modes are involved in the interference.

6.3.2 Experimental results

To further investigate of multibeam interference, a broadband light source, the amplified spontaneous emission (ASE) from an L-band EDFA over 1540–1640nm, was connected to a tapered fiber tip and as shown in Fig. 6.5, a cleaved SMF was used as a probe and placed in front of the fiber tip. The other end of this SMF was connected to an optical spectrum analyzer (OSA).

When the SMF is far from the tip, there is no obvious interference pattern. In this case, Fig. 6.6 shows the broadband transmission spectra and attenuation spectra of tapered fiber tips A and B. Tip A has highly wavelength-dependent loss. The long

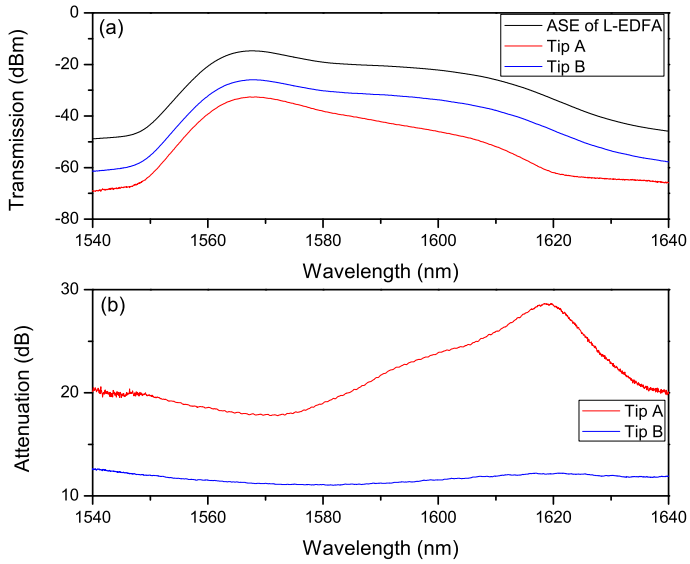

Figure 6.6: The broadband transmission spectra (a) and attenuation spectra (b) of tapered fiber tips A and B. The attenuation spectra are obtained by subtracting background ASE spectra.

wavelength component is found to have higher loss, which is over 25dB at a wavelength around 1620nm. Tip B has lower attenuation (∼13dB), which is only slightly dependent on wavelength. As discussed in previous section, the long-wavelength component in high-order modes cannot propagate through the waveguide, but the light below the cutoff wavelength can still go through the tip. Therefore, in the transmission spectrum, the long wavelength light shows relatively higher loss. It is also noted that, by varying the fiber tip sizes, the cutoff wavelength of higher-order cladding modes can be tuned. By contrast, tip B has a larger tip end and more higher-order modes continue to propagate through tip B. Therefore, tip B has weak long-wavelength loss.

Figure 6.7 show the transmission and attenuation spectra of tapered fiber tips A and

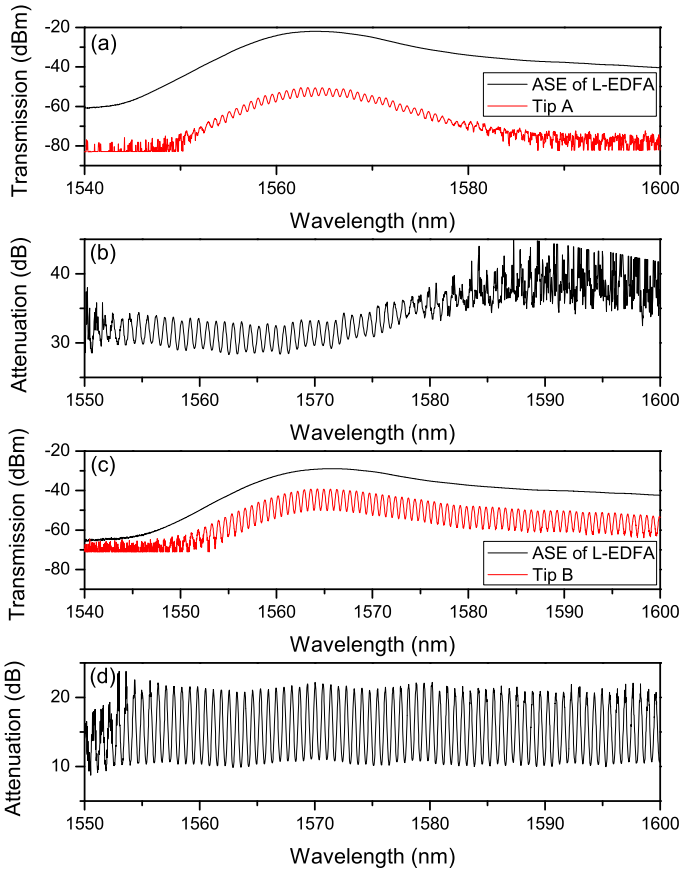

Figure 6.7: The reshaped comb-like transmission and attenuation spectra of tapered fiber tips A and B, respectively. The attenuation spectra are obtained by subtracting background ASE spectra.

B, respectively.The attenuation spectra of tips A and B have *ER* of ∼5dB and ∼12dB, respectively. As shown in Eq. (6.4), more energy is redistributed from the fundamental mode to the cladding modes in tip B because of larger taper angle or steeper slope, and hence higher ER is achieved.

When the relative position of the tip and the probe SMF is slightly adjusted, the interference spectrum is shifted. In the case of tip B, a clear wavelength shift is presented

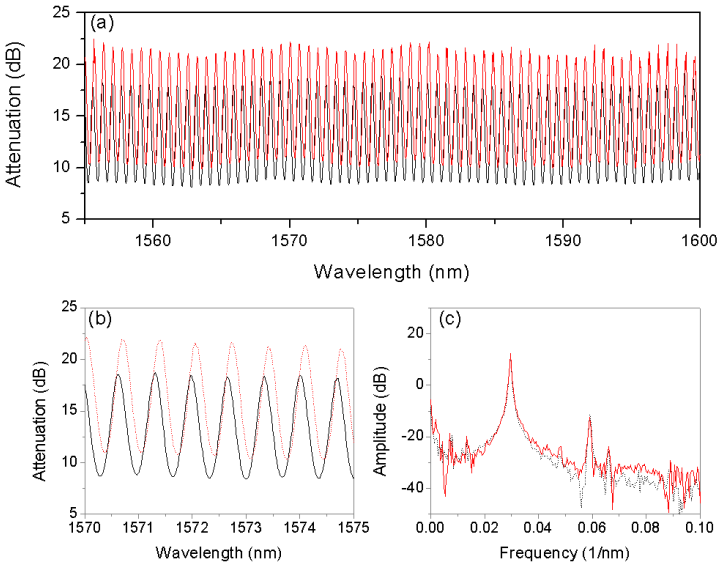

Figure 6.8: (a) The attenuation spectra of tapered fiber tip B at two positions. (b) The attenuation spectra. (c) FFT response of the detected transmission spectrum.

in Fig. 6.8(a) and part of its spectra is magnified and shown in Fig. 6.8(b). The spectra in Fig. 6.8(a) are normalized and Fourier transformed to get the spatial frequency spectra of the interference fringes. Interestingly, as shown in Fig. 6.8(c), one dominant peak and a second peak are observed. According to previous discussion, multi-peaks in the spatial frequency spectrum indicate that many cladding modes are involved in the interference.

6.4 Laser setup and results

Due to the multibeam interference in the near field, tapered fiber tips can be used as high-resolution filter device. A tunable laser using a tapered fiber tip as a tunable bandpass filter is built in a fiber ring. The experimental setup is shown in Fig. 6.9. The laser

consists of a tapered fiber tip, an SMF, an optical amplifier, a 50 : 50 coupler and an isolator. The isolator plays an important role, avoiding optical reflections at the interfaces of optical components going into the optical amplifier. Since the optical amplifier provides a significant amount of optical gain, even a small amount of optical reflection may result in oscillation, and therefore degrade the amplifier′s performance. An OSA is connected to the output port of the coupler to monitor the output spectrum. The ASE of optical amplifiers propagated through the tapered fiber tips and went into the probe SMF. With the help of translation stages, as shown in Fig. 6.5, the relative positions of the fiber tip and the SMF can be adjusted. The broadband light was reshaped to the comblike transmission peaks due to the characteristic of the fiber tip. The transmission loss between the tip and the SMF was over 10dB. The total cavity loss was over 13dB, which included 3dB loss due to the 50 : 50 coupler. When the gain of the amplifier compensates for the total cavity loss including coupling loss, 50% of the comb-like peaks are selectively amplified each cycle. Thus, through drastic competition between comb-like peaks, the highest intensity peak received the most gain from the amplifier and became the dominant spectral component in the ring. The tuning range of the relative positions of the fiber tip and the SMF is $\pm 7\mu$m in the X and Y directions in the experiment for spatial mode selection of cladding modes. The wavelength of the laser shifts to shorter wavelengths as the center-to-center distance between the SMF and the tip in the XOY plane increases. In this way, a tunable ring laser can be obtained easily. Optimization of the tunable laser involves increasing the SMSR, decreasing the bandwidth and enlarging the tuning range.

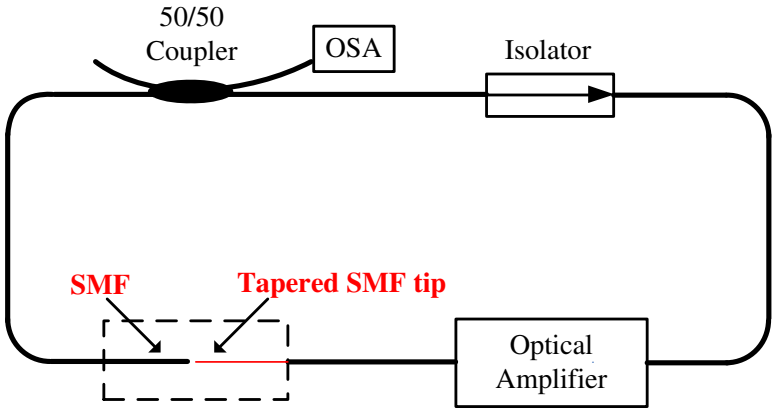

Figure 6.9: Experimental setup of a tunable ring laser using a tapered SMF tip.

Three kinds of optical amplifiers, an SOA, a C-band EDFA and an L-band EDFA, were used inside the fiber ring.

The SOA (QSOA-1550, QPhotonics, Inc.) has a gain of 25dB at a bias current of 400mA. Figure 6.10(a) presents the ASE spectrum of SOA at I_{SOA}=400mA. By adjusting the relative position of the fiber tip and the probe fiber in the transverse direction (XOY plane), the output of the light source is reshaped, resulting in one-peak, two-peak and multi-peak output states, which are shown in Figs. 6.10(b)–(d), respectively. This means that there is fierce gain competition between wavelength components. A 5m fiber ring cavity length results in a round-trip time of ∼25ns and the SOA has a relaxation time of 100ps or so [52]. Therefore, the system suffers from the relatively fast response of the SOA. This is why the highest intensity peak has little advantage due to multiple cycle amplification for comparison of low intensity peaks.

In order to build an efficient mode-selecting mechanism, an EDFA may be introduced to the laser ring, instead of SOA. As a result, the fluorescence relaxation time is extended

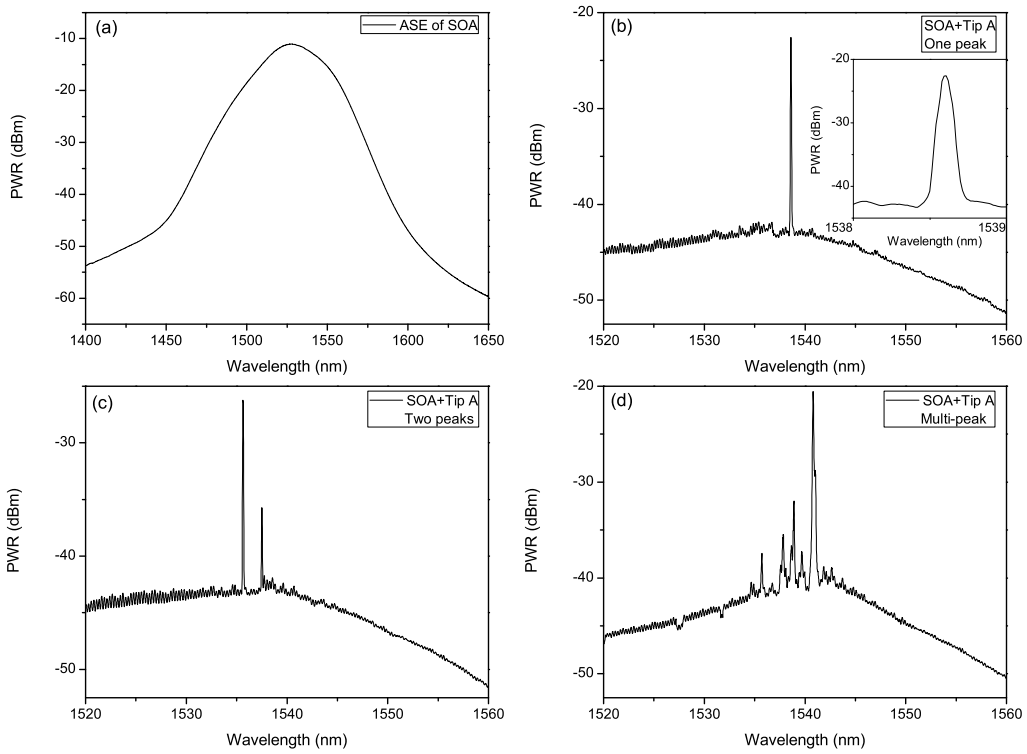

Figure 6.10: (a) ASE spectrum of SOA with $I_{SOA} = 400mA$. (b)-(d) Power spectra of the light output with SOA and tip A.

to ∼10ms. A C-band EDFA with a gain of 20dB is introduced in the tunable ring laser. With precise adjustment of the relative position of the fiber tip and the probe fiber in the transverse direction, a tunable laser is obtained. With the help of the C-EDFA, the competition between different modes is gradual rather than drastic, as in the case of an SOA with a shorter relaxation time. The highest intensity peak becomes the dominant spectral component in the ring. This results from the relatively large fluorescence time associated with the excited erbium ions. Thus, the EDFA can keep high gain with

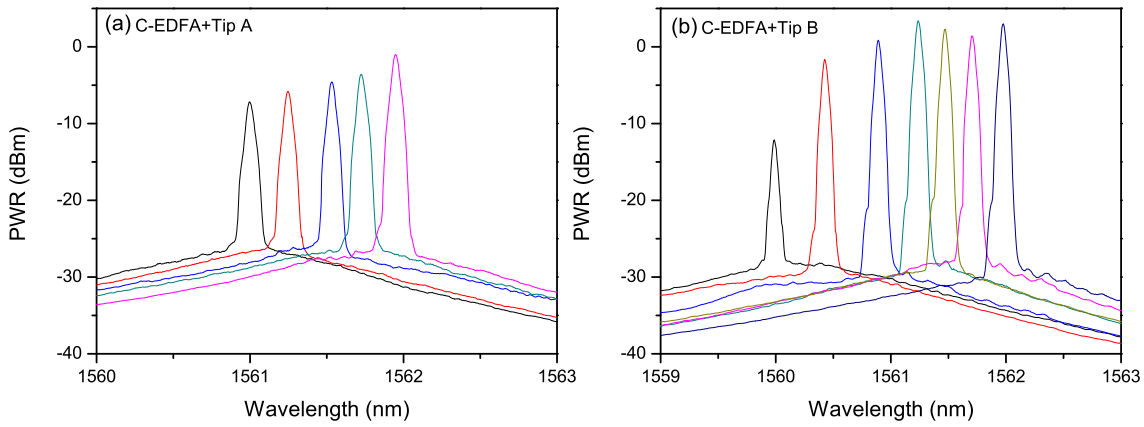

Figure 6.11: Power spectra of the laser output with a C-band EDFA for (a) tip A and (b) tip B, respectively.

more round-trip time. The experimental results are summarized in Table 6.1 and Fig. 6.11. The measurement of bandwidth is limited by the maximum resolution of the OSA. However, the tuning range of the ring laser is found to be only 1–2nm, which is limited by both the C-band amplifier and the tip's long wavelength characteristics. This is because the energy redistribution happens at the long wavelength range due to the cutoff of higher-order modes.

In the case of the L-band EDFA, with precise adjustment of the relative position

Table 6.1: Laser characteristics with C-EDFA and L-EDFA, respectively.

Characteristics	C-EDFA		L-EDFA	
	Tip A	Tip B	Tip A (50:50; 99:1)	Tip B (50:50; 99:1)
SMSR (dB)	25	31	22/26	27/29
Bandwidth (nm)	0.06	0.06	0.06	0.06
Tuning range (nm)	1	2	9	9

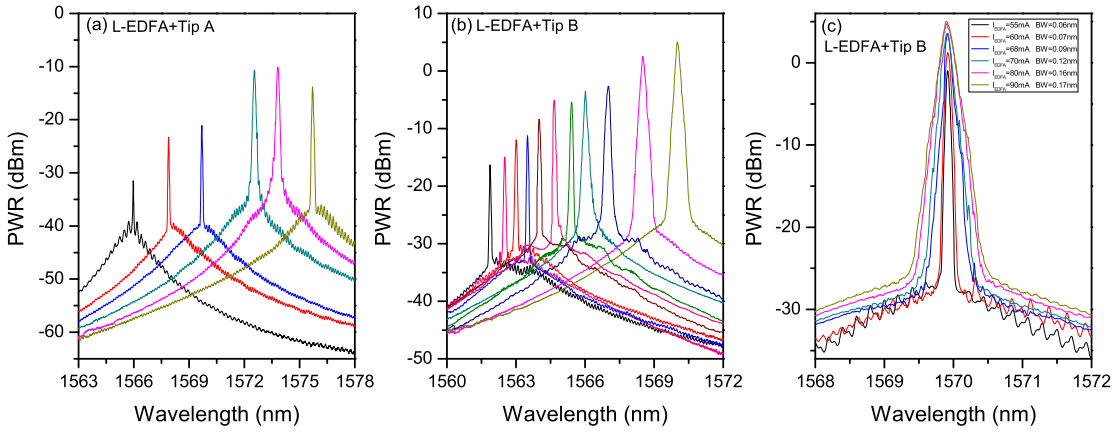

Figure 6.12: (a)(b) Power spectra of the laser output with an L-band EDFA for tips A and B, respectively, with $I_{EDFA} = 90$mA. (c) The bandwidths of the laser are broadened when the current of the L-band EDFA is increased.

of the fiber tip and the probe fiber, the wavelength of the laser was made to change steadily from 1566nm to 1575nm, with a bandwidth less than 0.06nm (the L-band EDFA wass at the threshold current of 55mA). The experimental results for tips A and B are summarized in Table 6.1 and Fig. 6.12. Figure 6.12(b) shows that, with the L-band EDFA current of 90mA, the bandwidth of the laser increases as the wavelength increases. Figure 6.12(c) shows that, when the current of the L-band EDFA is increased, the bandwidth is broadened at a fixed center wavelength. The bandwidth of the laser can be tuned from 0.06nm to 0.17nm with a 35mA current change of the amplifier.

As listed in Table 6.1, comparing the characteristics of the ring lasers with tips A and B, it was found that the laser including tip B, which has a larger slope, has a better SMSR. As we discussed in previous section, tip B acts as a filter with a higher ER. Therefore, tip B builds a more efficient mode-selecting mechanism and the laser obtains

a higher SMSR.

When the 50 : 50 coupler was replaced with a 99 : 1 coupler, the SMSR of the laser was improved by 2–4dB. If the total loss of the ring is reduced by changing the coupler ratio or the total gain of the ring is increased by increasing the current of the amplifier, the SMSR of the laser will be enhanced.

6.5 Discussion on chemical polish technique

Two more methods are demonstrated experimentally to have resulted in an improved setup. The first one is the fabrication of tips. The tapered tip was vertically dipped into the surface of 5% HF acid. Due to surface tension, the meniscus rise can nearly perfectly polish the surface of the tip, which can reduce the loss of the filter by 2dB. Secondly, the filter was placed in a tube with water. The smaller refractive index difference between the cladding and the liquid reduced the loss of the propagation of light in the down-tapering region of the tip by 2.5dB. In addition, the viscosity of water made the lightweight tip insensitive to the disturbance of environment. As shown in Fig. 6.13, by comparison with previous work, the laser tuning range increases from 9nm to 13nm in the L-band wavelength range and SMSR increases from 27dB to 33dB.

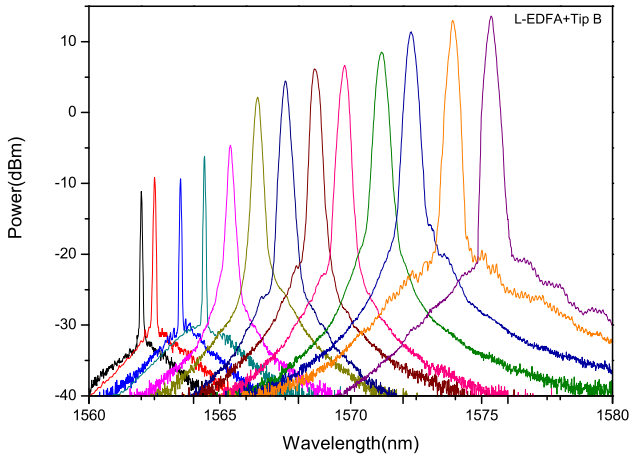

Figure 6.13: Power spectrum of the laser output with an L-band EDFA for chemically polished tip B.

6.6 Conclusion

We have demonstrated that a ring laser using a tapered SMF tip can achieve high SMSR, and tunable narrow bandwidth over a wide tuning range. To optimize the ring laser, we choose fiber tips with a steep slope and L-band EDFA with a long relaxation time. The bandwidth was tuned from 0.06nm to 0.17nm by varying the gain of the amplifiers. The tuning speed of the ring laser can be compared to the relaxation time of amplifiers, which is 10ms for the L-band EDFA. With the same tuning range, the bandwidth of the laser is more than ten times narrower than that of an FBG laser, and it is tunable, while the FBG laser and the FP laser both have a fixed bandwidth. With the same bandwidth, the tuning range of the laser is more than ten times larger than that of an FBG laser and an FP laser. In addition, this new tuning mechanism is simple and cost effective. Due

to the lightweight tapered SMF tip, the stability of the tunable laser is less than that of commercial tunable FBG lasers and FP lasers. However, enclosure of the device on a vibration-free bench can greatly reduce the environmental disturbance to the fiber tip. Furthermore, piezoelectric transducer tuning mechanics and additional feedback circuits can be used to achieve high stability. The proposed ring laser with a tunable narrow bandwidth over a wide wavelength range has great potential for wavelength division multiplexing systems in sensing and communications.

Chapter 7

C- and L-band tunable fiber ring laser using a two-taper Mach-Zehnder interferometer filter

In this chapter, a two-taper Mach-Zehnder interferometer (MZI), is proposed as a mode-selecting device in a fiber ring laser over both C- and L-band wavelength ranges. Section 7.1 introduces the research motivation. Section 7.2 presents the principle of a two-taper MZI. Section 7.3 introduces the experimental setup and results. A thermal annealing treatment is also applied to the tunable filter and substantially enhances the performance of the tunable laser. Section 7.4 discusses the bandwidth measurement using delayed self-heterodyne detection.

7.1 Introduction

Tunable lasers have a variety of applications, in particular for wavelength division multiplexing (WDM), optical communication, and as optical sensors. Tunable filters are often used as the wavelength tuning components of tunable lasers. All-fiber-based filters include fiber Bragg gratings (FBGs) [30–32], in-line Fabry-Perot (FP) filters [33], and filters based on special fibers, such as multimode fibers (MMFs) [35], few-mode high-birefringence fibers (FM-HBFs) [36], tapered fibers [28], and tapered fiber tips [94]. FBGs incorporated with piezoelectric stack actuators have a tuning range of over 45nm with a 3dB bandwidth of 0.7nm. In-line fiber FP filters are commercially available, but they are rather expensive and their tuning ranges are limited to less than 1nm by the piezoelectric stretching element. MMF filters have a larger tuning range of 60nm with tuning steps of 2.5–3nm and a side-mode suppression ratio (SMSR) of 40dB [35]. A new type of tunable laser, based on FM-HBFs, has also been reported recently. This new laser has a tuning range in excess of 40nm with a tuning step of about 2.2nm and an SMSR of 40dB [36]. By stretching an SMF taper, an EDFRL has a tuning range of over 20nm, a tuning step of over 2nm, a bandwidth of 0.05nm and an SMSR better than 45dB over the entire tuning range [28]. For lasers based on tapered SMF tips, the tuning range is less than 8nm with steps of 0.5–1.5nm and an SMSR of less than 35dB [94].

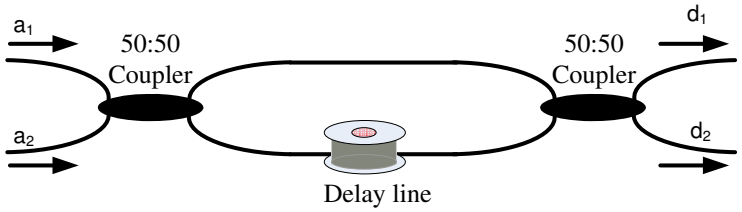

Figure 7.1: Illustration of a fiber MZI.

7.2 Principle

7.2.1 Principle of Mach-Zehnder interferometer

An MZI is a device used to determine the relative phase shift between two collimated beams from a coherent light source. The interferometer has been used, amongst other things, to measure small phase shifts in one of the two beams caused by a small sample or the change in length of one of the paths. In free space, an MZI consists of two optical beam splitters (combiners) and two mirrors to alter the directions of the beams. The basic configuration of a fiber MZI is shown in Fig. 7.1, and its basic components are optical couplers and optical delay lines.

By cascading the transfer functions of two 3dB optical couplers and that of the optical

delay line, the transfer function of an MZI may be found to be

$$\begin{aligned}\begin{bmatrix} d_1 \\ d_2 \end{bmatrix} &= \begin{bmatrix} \frac{1}{\sqrt{2}} & i\frac{1}{\sqrt{2}} \\ i\frac{1}{\sqrt{2}} & \frac{1}{\sqrt{2}} \end{bmatrix} \begin{bmatrix} e^{-i\phi_1} & 0 \\ 0 & e^{-i\phi_1} \end{bmatrix} \begin{bmatrix} \frac{1}{\sqrt{2}} & i\frac{1}{\sqrt{2}} \\ i\frac{1}{\sqrt{2}} & \frac{1}{\sqrt{2}} \end{bmatrix} \begin{bmatrix} a_1 \\ a_2 \end{bmatrix} \\ &= \frac{1}{2} \begin{bmatrix} e^{-i\phi_1} - e^{-i\phi_2} & i(e^{-i\phi_1} + e^{-i\phi_2}) \\ i(e^{-i\phi_1} + e^{-i\phi_2}) & -(e^{-i\phi_1} - e^{-i\phi_2}) \end{bmatrix} \begin{bmatrix} a_1 \\ a_2 \end{bmatrix}, \end{aligned} \tag{7.1}$$

where $\phi_i = \frac{2\pi}{\lambda} n_i L_i$ is the phase delay of each delay line.

If the input port 2 is disconnected (a_2=0), the optical power transfer function from input port 1 to output ports 1 and 2 are

$$T_{11} = \left| \frac{d_1}{a_1} \right|^2_{a_2=0} = sin^2 \frac{\Delta\phi}{2}, \tag{7.2}$$

$$T_{12} = \left| \frac{d_2}{a_1} \right|^2_{a_2=0} = cos^2 \frac{\Delta\phi}{2}, \tag{7.3}$$

with

$$\Delta\phi = \phi_1 - \phi_2 = \frac{2\pi}{\lambda}(n_1 L_1 - n_2 L_2), \tag{7.4}$$

where $\Delta\phi$ is the differential phase shift between two MZI arms. The transmission efficiencies T_{11} and T_{22} are functions of both the wavelength λ and the differential optical length $\Delta l = n_1 L_1 - n_2 L_2$ between two MZI arms. Obviously, an MZI can be widely

used as an optical filter. As long as the optical length difference changes, the phase will change, and so does the spectrum. Note that this optical length difference may arise either from a different path length $\Delta L = L_1 - L_2$ or through a refractive index difference $\Delta n = n_1 - n_2$.

7.2.2 Principle of two-taper Mach-Zehnder interferometer

Two abrupt fiber tapers made of single-mode fiber (SMF) are concatenated to form an in-line fiber MZI [22], which is shown in Fig. 7.2(a). The abrupt tapers are fabricated by an Ericsson fusion splicer (FSU-995FA) using a customized tapering program. The taper profiles are quite uniform, with a typical waist diameter of 33μm. A microscope image of a representative fiber taper is shown in Fig. 7.2(b). When a fiber is tapered down to tens of micro-meters, it becomes more pliable and can be bent at a much larger angle than SMF without breaking. By making use of this mechanical characteristic, a simple and cost-effective tunable MZI is built. The tapers are fixed on three positioning stages, and the middle jacket-off fiber is straightened. The curvature of the first taper is adjustable in three dimensions, while the second taper is always kept straight. The fundamental mode is partly coupled to the cladding modes (the two solid blue lines in the cladding of the jacket-off SMF in Fig. 7.2(a)) by the first taper [8]. The excited cladding modes propagate along the jacket-off fiber, which is assumed to be a lossless waveguide. The remaining energy is kept in the core mode (the single red line in the core of the jacket-off SMF in Fig. 7.2(a)). Then, on passing through the second taper,

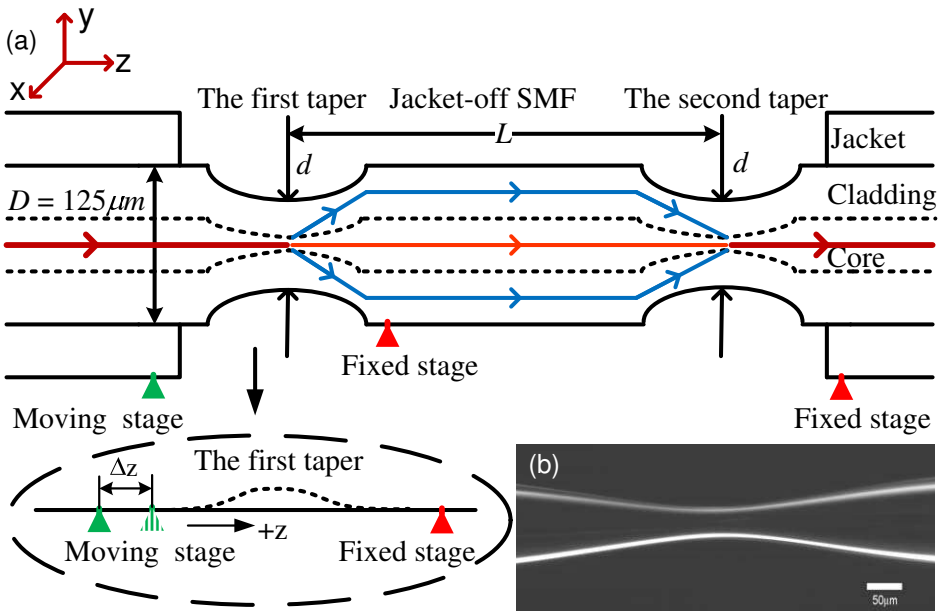

Figure 7.2: (a) Schematic of a two-taper MZI. D: cladding diameter of SMF; d: cladding diameter of the fiber taper waist; L: the cavity length. (b) Microscope image of a representative taper. The length of scale bar is 50μm.

part of the cladding modes are coupled back into the core. According to Eq. (7.4), the refractive index differences between the core mode and the cladding modes give rise to the differential phase shift between two MZI arms and results in multiple interferences, which are observable as a pattern of oscillation in transmission spectra [95].

7.3 Experimental setup and results

First, the transmission spectrum of a two-taper MZI is inspected. An amplified spontaneous emission (ASE) from an L-band EDFA was connected to a two-taper MZI and the reshaped spectrum was monitored by an optical spectrum analyzer (OSA). Because of the interference between the core mode and the cladding modes in the two-taper MZI,

the ASE is reshaped into a comb-like transmission spectrum [95]. As a taper is bent, the deformed taper waveguide may excite more cladding modes and change the coupling coefficients of the different cladding modes [96–98]. As shown in Figs. 7.3(a) and (b), the total transmission loss is about 8–24dB, which increases as curvature of the bent taper increases. The normalized attenuation spectra are Fourier transformed to get the spatial frequency spectra of the interference fringes. The spatial frequency value ξ is defined as [93]

$$\xi = \frac{\Delta m L}{\lambda_0^2}. \tag{7.5}$$

The spatial frequency is proportional to the interferometer length L and related to the differential modal group index Δm between two interference modes. If there is more than one peak in the spatial frequency spectrum, many cladding modes are involved in the interference. The amplitude of the peak indicates the energy of the cladding mode. Comparing Figs. 7.3(c) and (d), the amplitudes of the peaks increase greatly. It means that more energy is coupled from the fundamental mode to the cladding modes when the taper is bent.

The bending also introduces a small cavity length change ΔL in the MZI. All these factors can result in the observed variation of the transmission spectrum [96].

The two-taper MZI is employed as a bandpass filter in a fiber ring laser. Figure 7.4(a) shows the laser setup, which consists of a two-taper MZI filter, an L-band Erbium-doped fiber amplifier (EDFA), an isolator, a polarization controller (PC), and a $99:1$ coupler. The optical amplifier provides the gain, while the isolator keeps the laser unidirectional

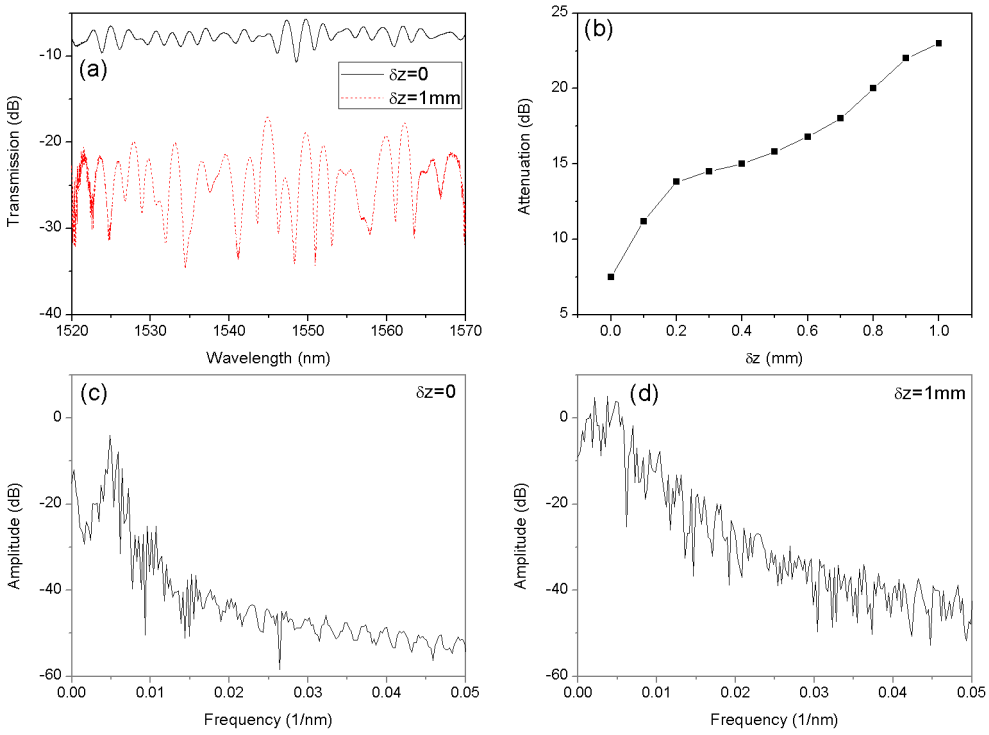

Figure 7.3: (a) The transmission spectra of a two-taper MZI filter at δz=0 and δz=1mm states. (b) The attenuation as a function of the position change along z axis. (c) (d) FFT responses of the normalized transmission spectra at δz=0 and δz=1mm states, respectively.

and the PC is used for suppressing the side modes. An OSA is connected to the 1% output port of the coupler to monitor the spectrum. The millisecond-scale fluorescence time of the EDFA keeps the light going through a nanosecond round trip with high gain millions of times. Only peaks with higher intensity can be amplified in these trips so that, after many passes, a one-peak output is achieved. When no external stress is applied to the taper region, the wavelength of the laser output is around 1600nm. This wavelength

decreases consistently as the taper bending angle is increased. In this way, the fiber ring laser can be tuned easily.

Thermal annealing was also used to optimize the two-taper MZI filter. The whole MZI filter was put in a closed oven at a constant temperature T=120°C. After 24 hours, the oven was switched off and then the filter was allowed to slowly cool to room temperature. The transmission loss of the filter was thus improved by 2dB. This improvement arose because the annealing treatment releaves internal mechanical stresses, eliminates interstitial defects, and stabilizes the MZI structure, while in taper fabrication, many internal stress points are formed and result in density nonuniformity, which creates many local scattering centers. Figure 7.4(c) shows that, with an L-EDFA current of 63mA and an annealed 35cm MZI, the laser is tunable over the entire L-band (1564–1605nm) with an SMSR of 50dB, a bandwidth of 0.1nm, and tuning steps of 0.8–1nm. The annealing treatment allows the tunable laser to cover a larger range with smaller tuning steps.

Instead of an EDFA, an Erbium-doped fiber (EDF) was used to provide the gain for the C-band laser. As shown in Fig. 7.5(a), the laser includes a 1m two-taper MZI filter, a section of forward pumped 7m EDF (R37PM01, OFS Inc.), a 1480nm laser diode (LD), a 1480/1550 wavelength-division multiplexer (WDM) coupler, an isolator, a PC, and a 99 : 1 coupler. The WDM is used to combine the short wavelength pump with the longer wavelength signal. The WDM combiner was used instead of a simple optical coupler to avoid the combination loss. Figure 7.5(b) shows the relation between the SMSR and the pump power; the threshold pump power is 17.68mW. The threshold value is related to

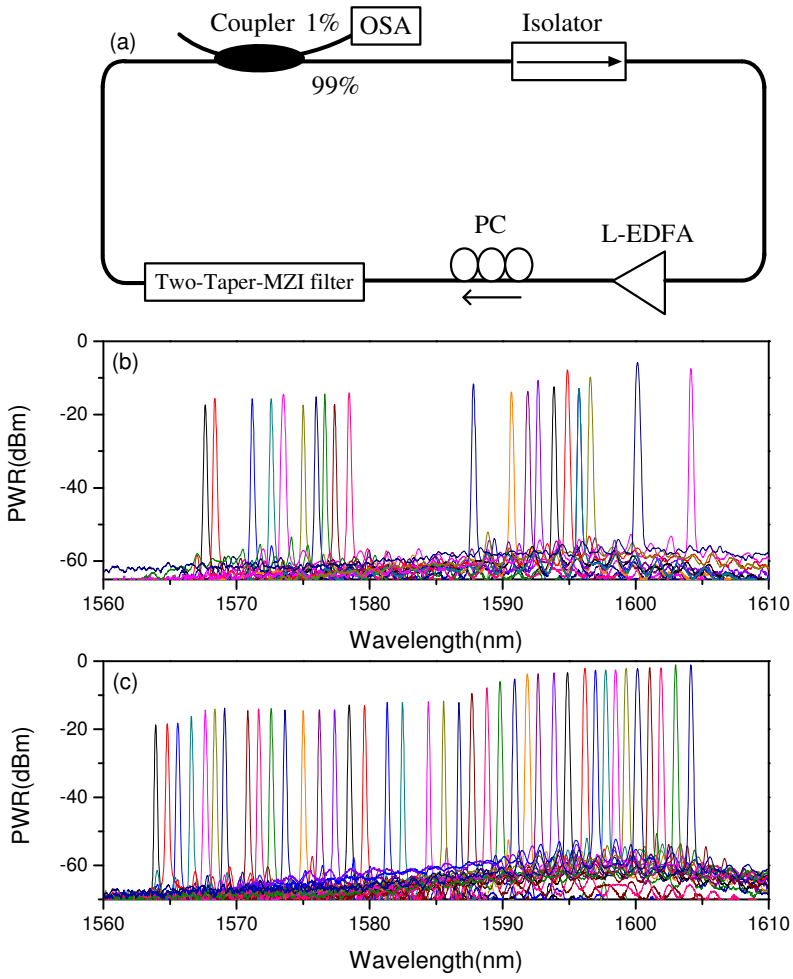

Figure 7.4: (a) Experimental setup of the L-band tunable ring laser using a two-taper MZI filter. Tuning characteristics of the ring laser with I_{EDFA} =63mA and L=35cm (b) before annealing and (c) after annealing.

the cavity loss. Once the pump power is over the threshold value, the SMSR of the laser output increases nonlinearly and tends to be saturated. Figure 7.5(c) shows that, with a pump power of 251.9mW, the laser can be tuned over the full C band with an SMSR of 50dB, a bandwidth less than 0.06nm (the maximum resolution of the OSA), and tuning steps of 0.3–0.7nm. It is shown that the output power difference is less than 0.5dB over

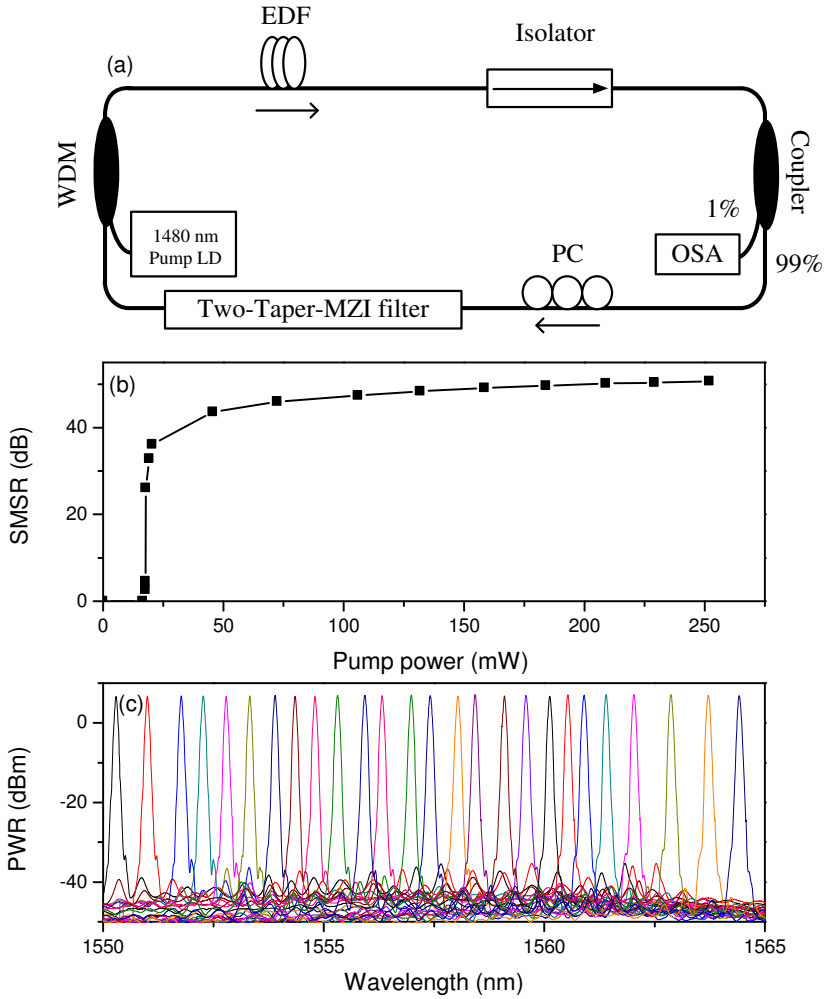

Figure 7.5: (a) Experimental setup of the C-band tunable ring laser incorporating a two-taper MZI filter. (b) SMSR of laser output versus pump current. (c) Tuning characteristics after annealing with pump power of 251.9mW.

the complete C band.

When the taper is in a loose state, the position of the moving stage is defined as the zero point in the coordinate systems shown in Fig. 7.2(a). The curvature of the taper can be changed by moving the stage along the $\pm z$ axis. This means that the taper is bent or stretched. In this way, it was found that the laser output was shifted

Table 7.1: Laser characteristics using MZIs with different lengths.

Characteristics	Cavity Length (cm)	SMSR(dB)	Bandwidth (nm)	Tuning Range (nm)	Step (nm)
L-EDFA	15	40–50	0.1–0.12	1564.9–1599.6	2–3
	20	45–50	0.1–0.14	1564.0–1602.4	1–2
	35	50	0.1	1563.9–1604.1	0.8–1
7m EDF	35	45–49	0.06	1557.0–1565.6	0.4–0.7
	100	42–50	0.06	1550.3–1564.6	0.3–0.7

to shorter wavelengths as the taper curvature was increased. Figures 7.6(a)–(c) show the relationship between the moving distances of the stage and the laser wavelengths. In order to cover the whole C-band range, slight adjustments along the x and y axes were also needed. Our experimental results further indicate that all tuning processes are reversible. To evaluate the laser output stability, we operated the laser in an open environment at room temperature. The wavelength shift was less than 0.06nm after 10 hours.

The laser tuning range was found to be associated with the cavity length of the MZI. The results in Table 7.1 imply that the tuning range increases as the cavity length increases. Since tuning is achieved by bending the taper, the material fatigue of the tapers is relevant to laser operation. Repeated tests were conducted before and after annealing. There was no sign of degradation of the laser output during these tests. We thus believe that these tapers are operating within the elastic region of their constituent material.

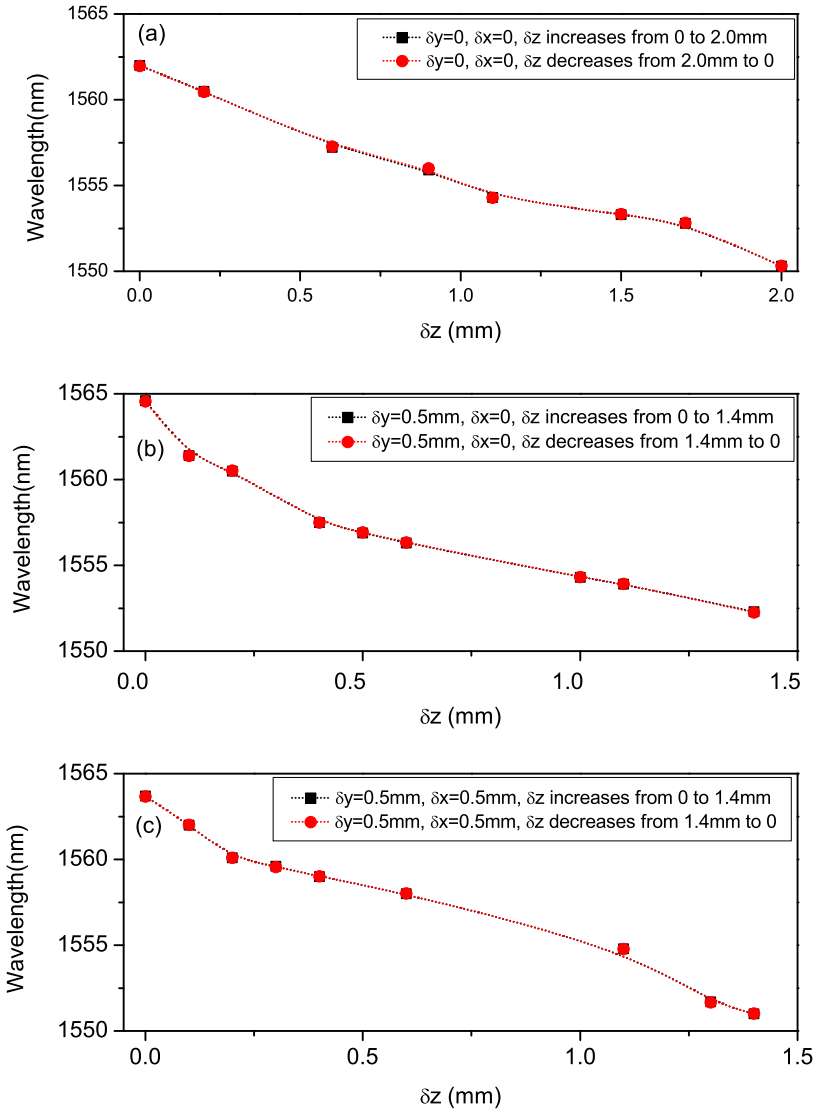

Figure 7.6: Laser tuning is realized by bending the taper along the x, y, and z axes. The black square and the red circle symbols represent the laser wavelength tuning circles. While keeping (a) Δy=0, Δx=0, (b) Δy=0.5mm, Δx=0, and (c) Δy=0.5mm, Δx=0.5mm, the laser is tuned by moving the stage along the z axis.

7.4 Bandwidth measurement

In the case of the EDF, it is found that the bandwidth of the laser is ∼0.06nm, which is equal to the maximum resolution of the OSA. In fact, typical grating-based OSAs do not offer enough measurement resolution required for laser bandwidth measurement. Scanning filter methods are not able to achieve this measurement resolution either. Compared with heterodyne detection, delayed self-heterodyne detection provides a simpler method to perform laser bandwidth measurement, because a large optical delay is used to replace a separate local oscillator.

The schematic setup for the optical delayed self-heterodyne detection is shown in Fig. 7.7. The laser output is split into two paths by the MZI. The optical frequency of the upper arm is offset by an acousto-optic modulator (AOM, Brimrose) with respect to the other. The frequency shift is ∼200MHz. The length of the delaying fiber is ∼2m, which must be longer than the coherence length of the laser, so that the two combining beams interfere as if they originated from two independent lasers. Thus the system performs in a manner similar to optical heterodyne detection. The bandwidth information is translated from optical frequencies to low frequencies, where electronics instrumentation operates. The interference signal is detected by using a photodetector (PD, Thorlabs PDB130C-AC). The spectrum is measured by using an electrical spectrum analyzer (ESA, Agilent E4446A). The measurement results are presented in Fig. 7.8. 2m delay line corresponds to a frequency rsolution of ∼50MHz [2, 54]. The cavity length is ∼23m, which corresponds to a mode spacing of 8.6MHz. When the interferometer

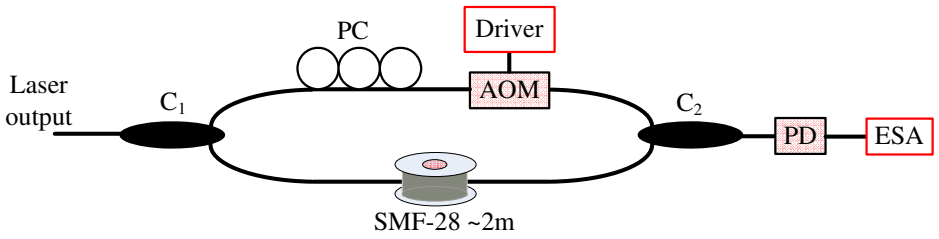

Figure 7.7: Schematic setup for optical delayed self-heterodyne detection. C_1, C_2: 3dB coupler; PC: polarization controller; AOM: acoustic-optic modulator; PD: photodetector; ESA: electrical spectrum analyzer.

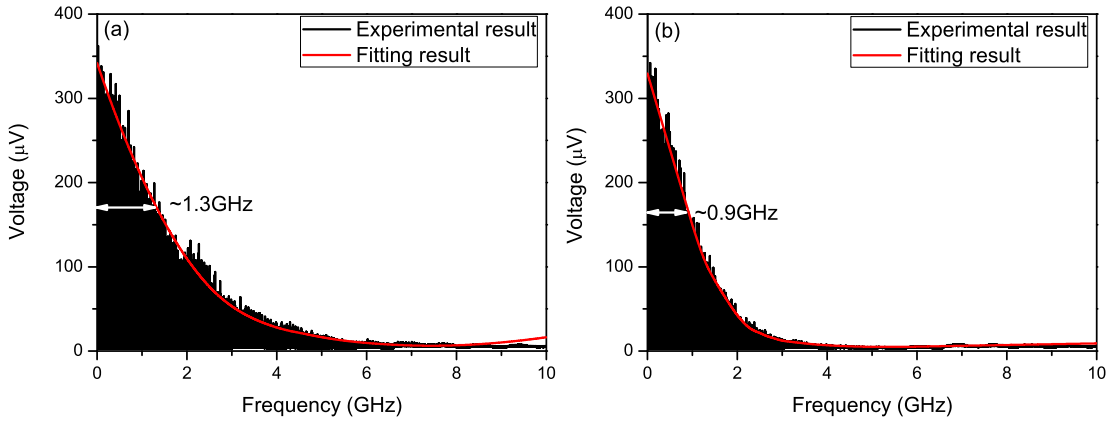

Figure 7.8: (a) (b) Laser bandwidth measurement using delayed self-heterodyne detection technique for cavity lengths of 35cm and 100cm, respectively.

length L=35cm, the bandwidth of the laser is ∼1.3GHz (10pm). When L is increased to 100cm, the bandwidth is improved to and ∼0.9GHz (7pm). Even through it is not a single longitudinal mode (SLM) laser, most longitudinal modes are suppressed and ∼100 modes are left.

7.5 Conclusion

In conclusion, we have successfully demonstrated a C- and L-band tunable ring laser using a two-taper MZI filter. The laser can be tuned in the 1550–1605nm wavelength range by using two different gain media. The fabrication of the MZI filter is simple, cost-effective, and repeatable. The material durability and operation stability are demonstrated in the experiments. It is expected that the stable laser could be used effectively for WDM systems in sensing and communication.

Chapter 8

Tunable Fabry-Perot filter using hollow-core photonic bandgap fiber and micro-fiber for a narrow-linewidth laser

In this chapter, a novel tunable fiber Fabry-Perot (FP) filter is proposed and demonstrated experimentally. The fiber FP filter is fabricated by using a hollow-core photonic bandgap fiber (HC-PBF) and a micro-fiber. The FP filter is incorporated in an Erbium-doped fiber ring laser (EDFRL) to build a simple and efficient mode selection mechanism. Section 8.1 presents the research motivation. Section 8.2 presents basic principle of FP filter and section 8.3 describes the fabrication and principle of this novel FP filter. Sec-

tion 8.4 shows an EDFRL setup and its characteristics. Both the theoretical discussion and experimental results confirm the single longitudinal mode (SLM) operation.

8.1 Introduction

Cost-effective tunable Fabry-Perot interferometers (FPIs) have been successfully commercialized and widely used for measurement of various parameters, such as strain, temperature, pressure, vibration, etc., in many fields [99–102]. In the past decade, most of the FPIs were based on splicing of different kinds of fibers, such as single mode fibers (SMFs) and multimode fibers (MMFs) [103], SMFs and photonic crystal fibers (PCFs)[104], SMFs and hollow-core photonic crystal fibers (HC-PCFs) [105], SMFs and hollow-core photonic bandgap fibers (HC-PBFs) [106], SMFs and tapered SMF tips [107]. However, these FPI sensor configurations have a limited tuning range on the order of micrometers.

Tunable lasers are of considerable interest for many applications, such as wavelength division multiplexed (WDM) communications, fiber sensors, high-resolution spectroscopy and optical coherent tomography. Linewidth is an important performance parameter. Standard distributed feedback (DFB) lasers and external cavity lasers (ECL) have typical linewidths of 5MHz and 100kHz, respectively. Tunable single-longitudinal-mode (SLM) lasers have the advantage of narrow spectral linewidth. Complex mode selection mechanisms have been used to achieve the SLM operation in erbium doped fiber ring lasers (EDFRL), such as multiple subring-cavities combined with either a fiber Bragg

grating (FBG) [84] or with an intracavity FP filter [85] or with a high finesse ring filter [108], a saturable absorber combined with either a widely tunable FBG [86, 87] or with an FP filter [88, 89], and a tunable FBG FP etalon [90, 91]. With a sub-cavity which is complicated and difficult to control, the side-mode suppression ratio (SMSR) of a conventional SLM-EDFRL can reach 50dB [84] or higher [108]. With a saturable absorber, the linewidth is reduced to ∼2kHz [84] or less [86, 88]. Due to the low finesse associated with low reflectivity in the transmission mode, the filter is used as a mode selecting element in ring laser, and has limited the linewidth (>5KHz) and tuning range (hundreds of GHz) of the fiber laser.

8.2 Principle of Fabry-Perot interferometer

A FPI consists of two parallel mirrors, having power reflectivities R_1 and R_2, separated by a cavity of length L containing a medium of refractive index n. The reflection process will be repeated many times until the amplitude is significantly reduced due to the multiple reflection losses. An illustration of an FPI is shown in Fig. 8.1. The excess loss, which corresponds to the portion of the incident power absorbed or scattered out of the beam by the mirror is neglected. The optical field amplitudes of light rays 0, 1, 2, and N are listed, where E_i is the input optical field, ϕ is the single-trip propagation phase delay in the interferometer, which is given by

$$\phi = \frac{2\pi nL}{\lambda}, \tag{8.1}$$

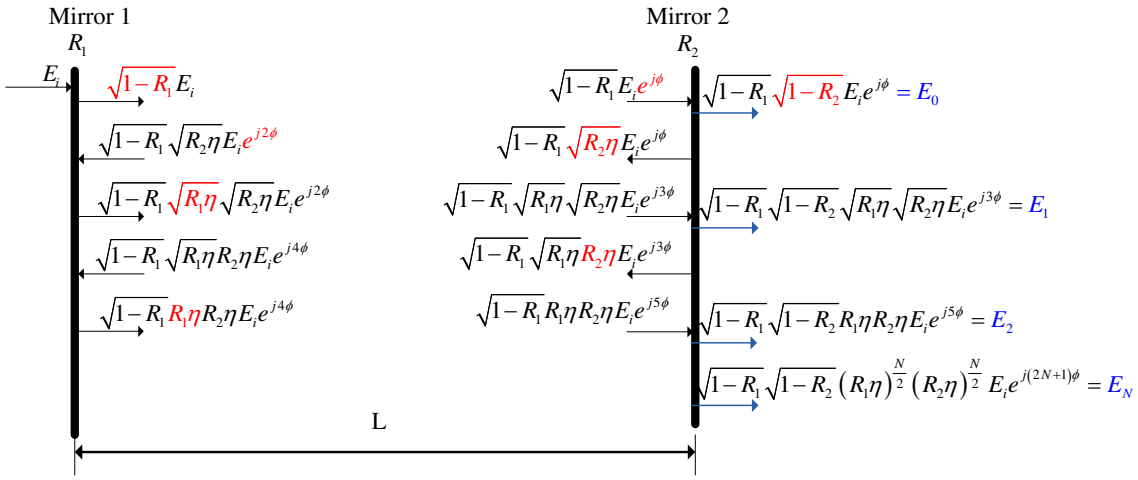

Figure 8.1: Transmission model of an FP filter.

where λ is the wavelength of light in vacuum.

Adding all transmitted beams, the total transmission field is

$$\begin{aligned} E_T &= \sum_{m=0}^{\infty} E_m \\ &= E_i\sqrt{1-R_1}\sqrt{1-R_2}e^{i\phi}\sum_{m=0}^{\infty}(\sqrt{R_1R_2}\eta e^{i2\phi})^m \\ &= E_i\sqrt{1-R_1}\sqrt{1-R_2}e^{i\phi}\frac{1}{1-\sqrt{R_1R_2}\eta e^{i}2\phi}. \end{aligned} \tag{8.2}$$

The normalized transmitted optical intensity $T(\lambda)$ can be derived as follows,

$$T(\lambda) = \left|\frac{E_T}{E_i}\right|^2 = \frac{(1-R_1)(1-R_2)}{1-\sqrt{R_1R_2}\eta^2 + 4\sqrt{R_1R_2}\eta\sin^2\phi}. \tag{8.3}$$

When $R_1 = R_2 = R$, $T(\lambda)$ is simplified to

$$T(\lambda) = \frac{(1-R)^2}{(1-R\eta)^2 + 4R\eta \sin^2(\frac{2\pi nL}{\lambda})}. \tag{8.4}$$

From Eq. (8.4), when the cavity length varies, the phase will change, and the reflection spectrum will shift.

8.3 Fabry-Perot filter fabrication and principle

A schematic diagram of the tunable FP filter is shown in Fig. 8.2(a). The filter consists of a section of HC-PBF (NKT Photonics, HC-1550) spliced with a standard SMF (Corning, SMF-28) and a section of micro-fiber. As shown in Fig. 8.2(b), the HC-PBF, which guides light by the photonic bandgap (PBG) effect, has an air-core surrounded by a micro-structured cladding comprising a triangular array of air holes in a silica background. The core and cladding diameters of the HC-1550 are 10.9μm and 120μm, respectively. The mode field diameter (MFD) of the HC-1550 is 7.5μm, which is different from that of the SMF (10.5μm). Fabrication of the etalon is straightforward and highly repeatable. First, the cleaved end of a HC-PBF is spliced to the cleaved end of a SMF-28 fiber using repeated arc discharges [109]. The micro-hole collapse effect of HC-PBFs should be taken into account. An electric arc fusion splicer (Fitel, FSU995A) with special parameters can repeat a low-loss fusion splice with good mechanical strength and a smooth reflective surface. Fresnel reflection is generated at the splicing point due to

modal field mismatch and refractive index difference. Second, the spliced HC-PBF is cleaved to a desired length L_m on the order of millimeters. Compared with the high transmission loss in a conventional Fizeau cavity with an air gap, the length of the low-loss FP cavity could be extended to several centimeters [105, 110]. Third, the micro-fiber is fabricated by chemical etching. A section of cleaved SMF is dipped into 5% Hydrofluoric (HF) acid vertically for about 20 hours. The fiber diameter, d, is reduced to 8–10μm. The micro-fiber with a uniform diameter of d and a length of ℓ can be designed to meet the requirement of the FP cavity. The end of micro-fiber acts as the other reflection mirror in the FP cavity. Fourth, in order to improve the fringe visibility, a gold film with a thickness of 20nm is coated at the end of the micro-fiber. The reflection coefficient of the film is $\sim$85%. A Fizeau-type etalon is formed by the reflection from the splicing surface of SMF and HC-PBF and the gold-coated end of the micro-fiber. The spacing of the FP filter can be changed over a large distance by adjusting the position of the micro-fiber in the hollow core of a HC-PBF. Microscope images of two reflection mirrors in the experiment are shown in Figs. 8.2(c) and (d). In these experiments, d=9μm, ℓ=3mm, and L_m=2.74mm.

For the FP filter, free spectral range (FSR) can be tuned by changing the longitudinal displacement of the micro-fiber, which is given by

$$FSR = \frac{\lambda^2}{2nL}, \tag{8.5}$$

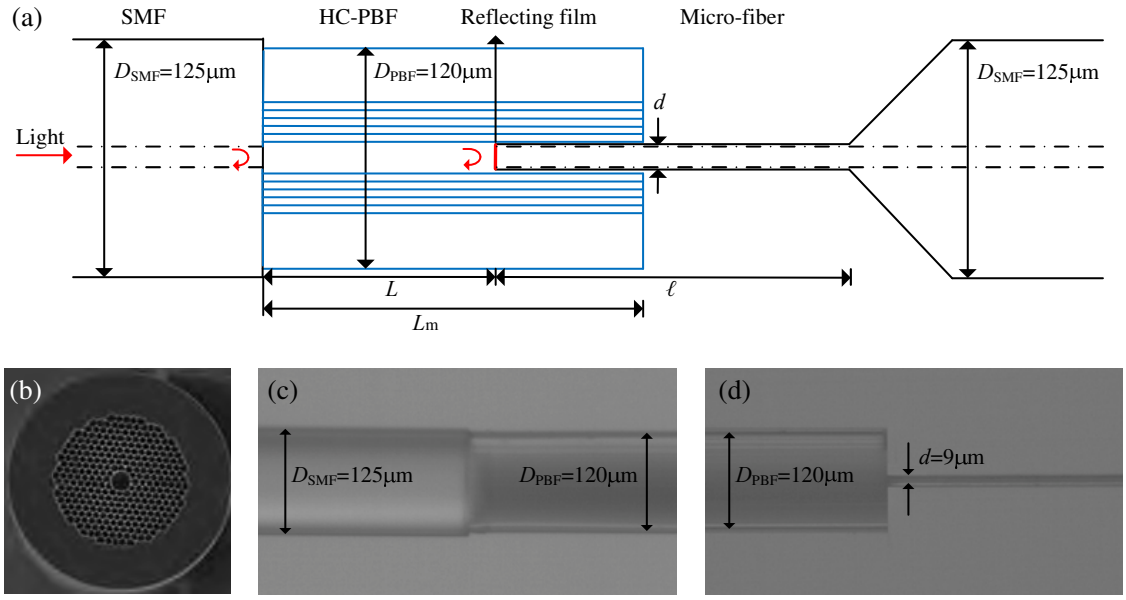

Figure 8.2: (a) Configuration of an FP filter based on HC-PBF and micro-fiber. D_{SMF}: Cladding diameter of SMF, D_{PBF}: Cladding diameter of HC-PBF, L_m: the length of HC-PBF, L: the cavity length, ℓ: the length of the micro-fiber, d: Cladding diameter of the micro-fiber. (b) Cross section of HC-1550. (c) Microscope image of a splicing point between SMF and HC-1550. (d) Microscope image of a HC-1550 with an inserted micro-fiber.

where L is the cavity length and n is the cavity refractive index. In the hollow core of HC-PBF, the medium is air and hence n=1. The FP filter with a long cavity length has a small FSR. Therefore, the reflection spectrum with a sharp slope allows the FP filter to be an efficient mode selecting etalon.

The model of electric fields at the FP cavity is shown in Fig. 8.3. R_1 and R_2 are the power reflection coefficients of the splicing point and the end of micro-fiber, respectively. R_1 is given by

$$R_1 = \left(\frac{n_{HC-PBF} - n_{SMF}}{n_{HC-PBF} + n_{SMF}} \right)^2, \tag{8.6}$$

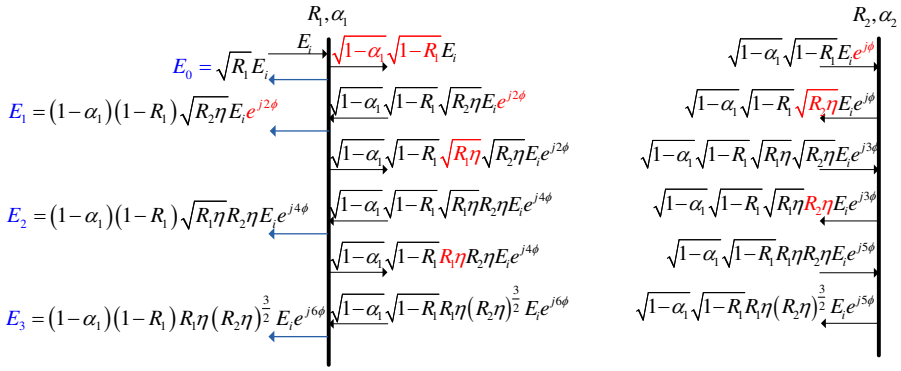

Figure 8.3: Reflection model of an FP filter.

where n_{HC-PBF} and n_{SMF} are refractive indices of the HC-PBF and SMF, respectively. R_1 is ∼3%. Before coating, the power reflection coefficient R_2 can be calculated similarly. After coating, R_2 is the reflection coefficient of the gold film, which is as high as 85%. α_1 is the transmission loss factor at the splicing point. α_{HC-PBF} is the transmission loss in the hollow core of HC-PBF. Here α_{HC-PBF} can be ignored [110]. $\eta < 1$ is the excess power loss of reflection on the mirror due to the non-ideal beam alignment. ϕ is the optical phase induced by the FP cavity, which is given in Eq. (8.1).

E_i is the input electric field and E_R is total reflected electric field at the detector, which is given approximately by

$$E_R = E_i \left[\sqrt{R_1} + (1-\alpha_1)(1-R_1)(R_2\eta)^{\frac{1}{2}} e^{j2\phi} + (1-\alpha_1)(1-R_1)(R_1\eta)^{\frac{1}{2}} R_2\eta e^{j4\phi} \right]. \quad (8.7)$$

The normalized reflective optical intensity $I_R(\lambda)$ can be derived as follows [54],

$$\begin{aligned} I_R =& \left|\frac{E_R}{E_i}\right|^2 \\ =& \left|\sqrt{R_1} + (1-\alpha_1)(1-R_1)(R_2\eta)^{\frac{1}{2}} e^{j2\phi} + (1-\alpha_1)(1-R_1)(R_1\eta)^{\frac{1}{2}} R_2\eta e^{j4\phi}\right|^2 \\ =& R_1 + (1-\alpha_1)^2(1-R_1)^2 R_2\eta - 2(1-\alpha_1)(1-R_1)R_1R_2\eta^{\frac{3}{2}} \\ &+ 2\left[(1-\alpha_1)(1-R_1)(R_1R_2\eta)^{\frac{1}{2}} + (1-\alpha_1)^2(1-R_1)^2 R_1^{\frac{1}{2}} R_2^{\frac{3}{2}}\eta^2\right]\cos 4\phi \\ &+ 4(1-\alpha_1)(1-R_1)R_1R_2\eta^{\frac{3}{2}}\cos^2 4\phi. \end{aligned} \tag{8.8}$$

Eq. (8.8) indicates that $I_R(\lambda)$ would reach its maximum and minimum when and $\cos 4\phi$=1 and $\cos 4\phi$=-1, respectively. The fringe visibility is determined by [106]

$$V = \frac{I_{R_{max}} - I_{R_{min}}}{I_{R_{max}} + I_{R_{min}}}. \tag{8.9}$$

Inserting Eq. (8.8) into (8.8), we obtain

$$V = \frac{2\left(1-\alpha_1\right)\left(1-R_1\right)\left(R_1R_2\right)^{\frac{1}{2}}\left[\eta^{\frac{1}{2}} + \left(1-\alpha_1\right)\left(1-R_1\right)R_2\eta^2\right]}{R_1 + \left(1-\alpha_1\right)^2\left(1-R_1\right)^2 R_2\eta + 2\left(1-\alpha_1\right)\left(1-R_1\right)R_1R_2\eta^{\frac{3}{2}}}, \tag{8.10}$$

and

$$\frac{\partial V}{\partial \eta} = \frac{2\left(1-\alpha_1\right)\left(1-R_1\right)\left(R_1R_2\right)^{\frac{1}{2}}}{\left[R_1+\left(1-\alpha_1\right)^2\left(1-R_1\right)^2R_2\eta+2\left(1-\alpha_1\right)\left(1-R_1\right)R_1R_2\eta^{\frac{3}{2}}\right]^2} \times\left[\frac{1}{2}R_1\eta^{\frac{1}{2}}+\left(1-\alpha_1\right)^3\left(1-R_1\right)^3R_2^2\eta^2 +\left(1-\alpha_1\right)^2\left(1-R_1\right)^2R_1R_2^2\eta^{\frac{5}{2}}-\frac{1}{2}\left(1-\alpha_1\right)^2\left(1-R_1\right)^2R_1R_2^2\eta^{\frac{1}{2}}\right]. \quad (8.11)$$

Using the experimental data, we have $\frac{\partial V}{\partial \eta} > 0$, which means that the fringe visibility V will decrease as η decreases. In addition, we know that η decreases as the cavity length L increases for a fixed length of the HC-PBF. Therefore, we obtain $\frac{\partial V}{\partial L} < 0$, which means that the fringe visibility of the FP filter decreases as the cavity length increases.

8.4 Experimental setup and results

The EDFRL configuration is shown in Fig. 8.4. The gain medium, a 7m EDF (R37PM01, OFS Inc.), is forward-pumped through a WDM by a 980nm laser diode (LD). The EDF has a peak absorption of 18dB/m at 1530nm. Two polarization controllers (PC) are used to adjust the polarization state of the light, which is used to optimize SMSR for each wavelength. An isolator (ISO) keeps the laser unidirectional. The laser output is monitored by an optical spectrum analyzer (OSA) through the 1% output port of a coupler (C_1). The 99% output of the coupler is injected into the FP filter via port 1 of a circulator. The reflected light of the FP filter is coupled into the main ring cavity

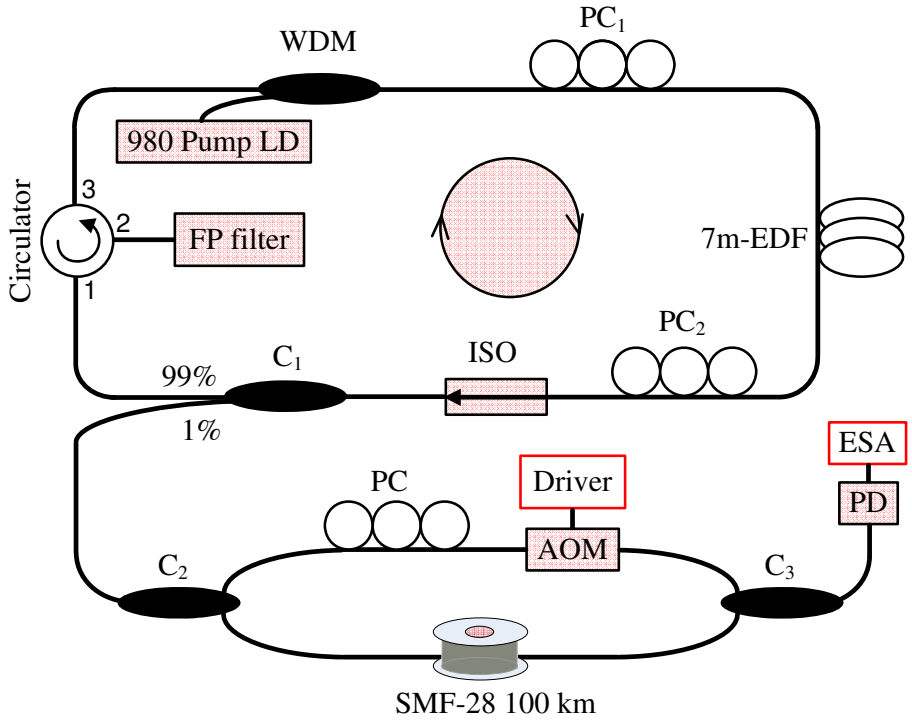

Figure 8.4: The upper ring is schematic setup of a tunable ring laser incorporating the novel FP filter. C_1: 99:1 coupler; PC_1, PC_2: polarization controller; ISO: isolator; The bottom MZI is schematic setup for optical delayed self-heterodyne detection. C_2, C_3: 3dB coupler; AOM: acoustic-optic modulator; PD: photodetector; ESA: electrical spectrum analyzer.

through port 3 of the circulator. The main ring cavity generates an enormous number of longitudinal modes. Suppression of side longitudinal modes is achieved by the novel FP filter with millimeter cavity length. The millisecond-scale fluorescence relaxation time of the EDF keeps the light going through a nanosecond round trip several million times to create high gain and long coherence length. In this way, a narrow-linewidth SLM operation is established by a simple combination of the novel FP filter and the single-ring cavity.

Figure 8.4 presents the reflection spectra (1550–1560nm) of the FP filter with dif-

ferent cavity lengths. These series of sharp fringes in wavelength space are used as a mode selection mechanism. When the cavity length L =0.36mm, 0.67mm, 1.23mm and 2.57mm, FSR=3.22nm, 1.72nm, 0.94nm and 0.45nm, respectively. Without and with gold coating, the insertion losses of the FP filter are 16.5dB and 12.7dB, respectively, with a cavity length of 0.36mm. The main loss is due to ∼3% Fresnel reflection at the splicing point between the HC-PBF and SMF. As shown in Fig. 8.5, the insertion loss increases as the cavity length of the FP filter increases due to non-ideal beam collimation in the HC-PBF and micro-fiber section. With the help of a 20nm gold film coated at the end of the micro-fiber, the contrast is improved from 2.9dB to 12dB with the cavity length of 0.36mm. The corresponding fringe visibility increases from 0.32 to 0.88. When the cavity length is increased to 2.57mm, the contrast is improved from 1dB to 5dB. The corresponding fringe visibility increases from 0.08 to 0.39. Because η decreases as the cavity length L increases, the fringe visibility of the FP filter decreases as the cavity length increases. Here $\frac{\partial V}{\partial L} < 0$ is verified experimentally. Comparing the slope of reflection spectra within a fixed wavelength range, the longer cavity length is associated with a sharper slope, which provides more efficient mode selection as an FP filter.

Tuning characteristics of the SLM-EDFRLs are shown in Figs. 8.6(a) and (b). The characteristics of the SLM-EDFRLs are listed in Table 8.1. With a short cavity length of 0.25mm and a tuning range of ±0.14mm, the FP filter has a larger FSR with a slow changing slope. The laser has a large tuning range over 1554–1562nm with a large step 0.2–0.3nm. The corresponding resolution of the translation stage is ∼0.004mm

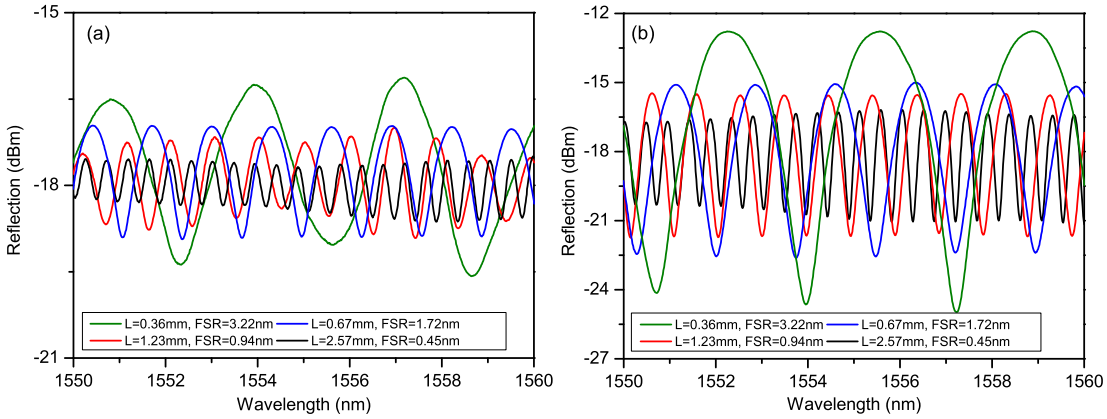

Figure 8.5: The reflection spectra of an FP filter (a) without and (b) with gold coating, respectively. When the cavity length L=0.36mm, 0.67mm, 1.23mm, and 2.57mm, FSR=3.22nm, 1.72nm, 0.94nm, and 0.45nm, respectively.

during laser wavelength tuning. When the cavity length increases to 2.37mm and the tuning range increases to ±0.37mm, the FP filter has a shorter FSR with a sharp slope. The tuning range of EDFRL is decreased to 1557.3–1560.2nm, while the tuning step is decreased to 0.06–0.1nm. The corresponding resolution of the translation stage is ∼0.002mm during laser wavelength tuning. The minimum resolvable tuning step of the laser is limited by the 0.0813802μm resolution of the motorized translation stage and the 0.06nm resolution of OSA. In practice, two accurate piezoelectrics (PZT) can be used for coarse and fine adjustment of the cavity length. The characteristics of the SLM-EDFRLs can thus be further improved. The power stability is also investigated. When the injected pump power is 190mW, the output power of the lasers are -8.0±0.4dBm and -7.6±0.1dBm, with the short and long FP cavities, respectively. Therefore, the high power stability of the proposed laser has been confirmed.

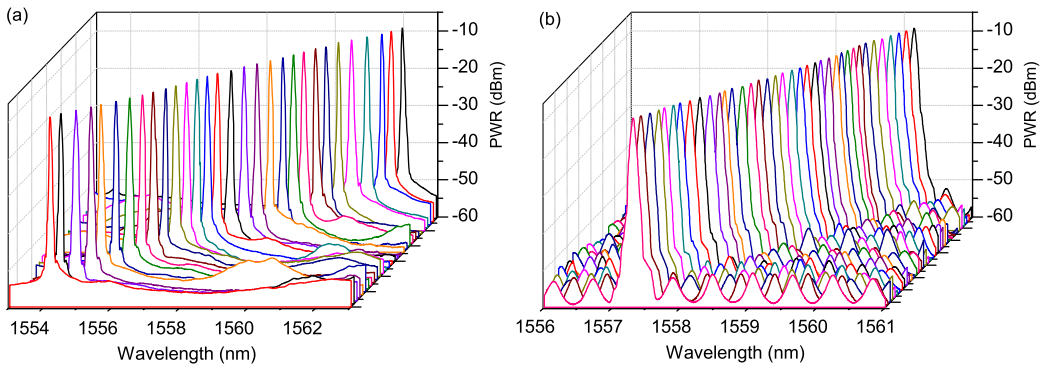

Figure 8.6: (a) Tuning characteristics with cavity length $L = 0.25 \pm 0.14$mm and pump power P_{EDF}=190mW. (b) Tuning characteristics with cavity length $L = 2.37 \pm 0.37$mm and pump power P_{EDF}=190mW.

As shown in Fig. 8.4, the linewidth of the laser output is measured by the self-heterodyne method. The laser output is launched into a MZI which is constructed by two 3dB couplers C_2 and C_3. An acousto-optic modulator (AOM, Brimrose) is added into the upper arm of MZI to generate a frequency shift of ∼200MHz. The length of delaying fiber is 100km, which corresponds to a 1kHz frequency resolution [54]. The interference signal is detected by using a photodetector (PD, Thorlabs PDB130C-AC). The spectrum is measured by using an electrical spectrum analyzer (ESA, Agilent E4446A).

Table 8.1: Laser characteristics.

Cavity length (mm)	0.25±0.14	2.37±0.37
Tuning range (nm)	1554–1562	1557.3–1560.2
Tuning step (nm)	0.2–0.3	0.06–0.1
SMSR (dB)	32–36	44–51
Linewidth (kHz)	5.1–9.1	3.0–5.5
Power (mW)	0.16±0.015	0.17±0.004

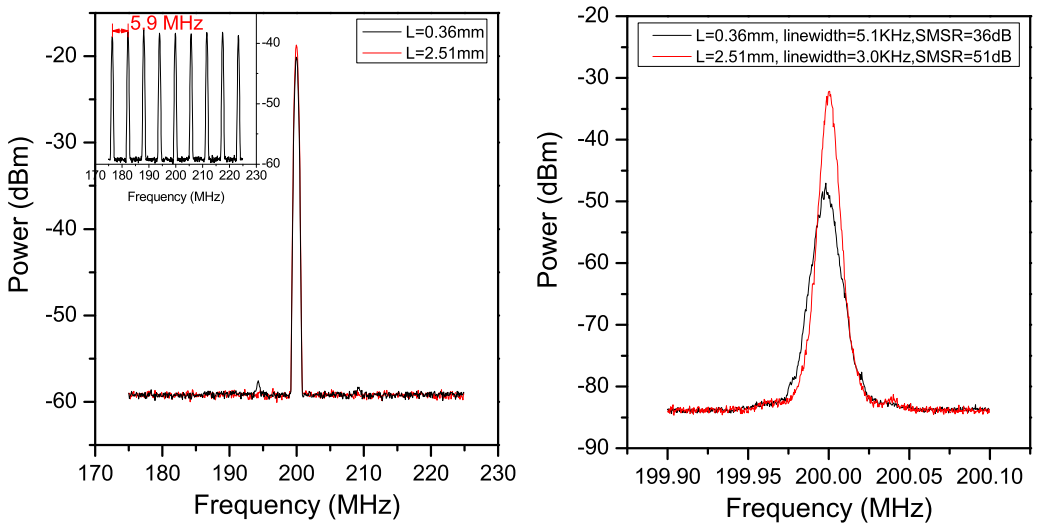

Figure 8.7: (a) Electrical spectra measurement of SLM-EDFRL with FP cavity lengths of L=0.36mm and L=2.51mm. The inset shows the electrical spectra of the beating signal of the main EDFRL cavity without FP filter. (b) 3dB linewidth measurement by ESA.

The electrical spectrum of the beating signal of the main EDFRL cavity without the FP filter is inserted into Fig. 8.7(a). The measured FSR is ∼5.9MHz. Figures 8.7(a) and (b) indicate the SLM operation and the narrow 3dB linewidths. For L=0.36mm, the SLM-EDFRL has an SMSR of 36dB and a linewidth of 5.1kHz. For L=2.51mm, the SLM-EDFRL has an SMSR of 51dB and a linewidth of 3.0kHz. Several residual side modes are highly suppressed and the spacing of the nearest side modes is ∼5.9MHz. The experimental results confirm that the FP filter with a longer cavity has much better side-mode suppression.

The SMSR is controlled by the polarization state of light, pump power and the mode selecting efficiency determined by the FP cavity length. For L=0.36mm and 2.51mm,

the threshold pump powers are 22mW and 20mW, respectively. As shown in Fig. 8.8(a) and (b), when the threshold pump current is reached, the EDFRL with a longer-cavity FP filter can obtain an SMSR of ∼31.2dB while the shorter one only has an SMSR of ∼16.5dB. In the low pump current range, all side modes vanish and the lasting longitudinal mode increases quickly, as shown by the curve of P_{EDF}=20mW in Fig. 8.8 (b). Therefore, the SMSR increases as the pump current increases. The SMSR reaches a maximum at the optimum pump current of P_{EDF}=102mW for both lasers. In the high pump current range, the side modes are partly suppressed and will increase as the pump current increases. Hence the SMSR decreases as the pump current increases. As shown in Fig. 8.8(a), linewidths are always limited in the range of 3–5kHz.

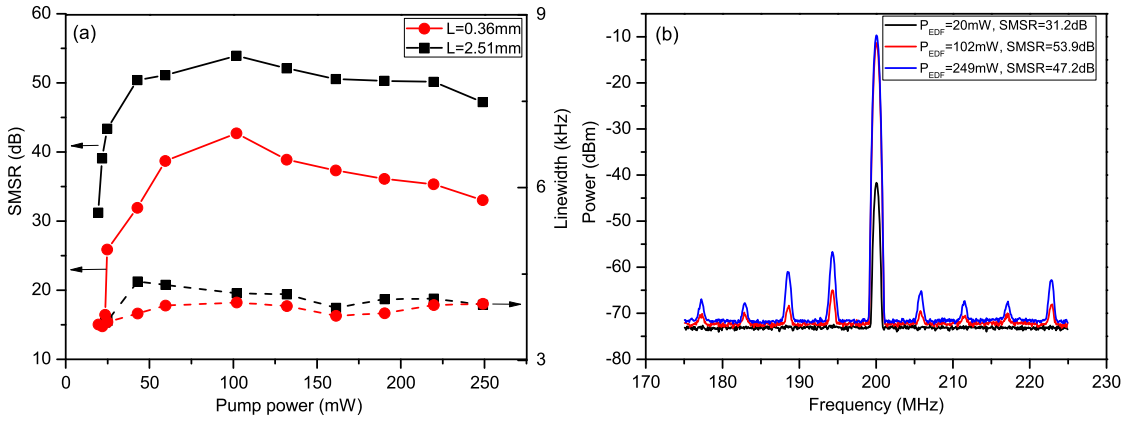

Figure 8.8: (a) SMSR (solid line) and linewidth (dash line) measurement when the pump power increases from the threshold value to 249mW. (b) Electrical spectra measurement of SLM-EDFRL with FP cavity lengths of L=2.51mm and P_{EDF}=20mW, 102mW and 249mW, respectively.

8.5 Conclusion

In conclusion, we designed and demonstrated a tunable FP filter, which is formed by a section of HC-PBF spliced with an SMF and a section of gold-coated micro-fiber. The hollow core of a HC-PBF is used as the interference cavity. The FP mirrors is comprised of a splicing point between a section of HC-PBF and a SMF and the gold-coated end of an inserted micro-fiber inside the HC-PBF. The repeatability of the fabrication process is proved in the experiments. The tunable FP filter with a millimeter cavity length constitutes an efficient mode selection mechanism in an EDFRL. With a cavity length of 0.25mm and a tuning range of ±0.14mm, the SLM-EDFRL can be tuned over 1554–1562nm with a minimum step of 0.2nm. The SMSR reaches 32–36dB and a linewidth of 5.1–9.1kHz. With a cavity length of 2.37mm and a tuning range of ±0.37mm, the SLM-EDFRL can be tuned over 1557.3–1560.2nm with a minimum step of 0.06nm. The SMSR reaches 44–51dB and a linewidth of 3.0–5.5kHz.

Chapter 9

Conclusion

9.1 Conclusion

This research proposes an efficient distributed birefringence measurement method–optical frequency-domain reflectometry (OFDR) technique–to continuously analyze the mode coupling process along tapered single-mode fibers (SMFs) and their thermal and mechanical properties. Based on the thermal properties study, it is found that annealing treatment is an essential step for the fabrication of fiber tapers, which can improve their optical properties. This is because the inhomogeneous refractive index character, due to residual stress induced by tapering process, can be distinctly eliminated by annealing treatment.

In addition, this OFDR method has been demonstrated to evaluate the polarization-preserving character of tapered polarization-maintaining fibers (PMFs). The reduced

thickness of stress-applying components results in the stress relaxation and reduces the birefringence in the tapered PMFs. Another factor is the generation of higher-order modes. Compared with cutback method, polarization extinction ratio (PER) and polarization dependent loss (PDL) measurement, the measured distributed birefringences along tapered PMFs reveal the accurate polarization maintaining ability. Because tapered PMF have various applications, the effective method to evaluate polarization preserving character is a matter of great significance.

This thesis also makes contribution to narrow-linewidth tunable Erbium doped fiber ring lasers (EDFRL). Instead of expensive fiber Bragg gratings (FBGs), Fabry-Perot (FP) filters and other complicated mode selecting devices, we build simple mode selecting mechanisms using micro-fiber devices. The fabrication is much easier and at a lower cost. First, in the EDFRL, the basic factor, the fluorescence relaxation time of gain medium, Erbium doped fiber (EDF), is studied. Compared with SOA, EDF has longer carrier lifetime, which benefits the formation of a ring laser and reduces the strict requirements for the mode selecting filters. Secondly, tapering is widely used as an effective mode conversion technique. Higher-order modes are easy to be excited in the tapering process. By exciting different higher-order mode, the refractive index difference is tuned. Based on this principle, a cost-effective two-taper MZI is built in a section of SMF and forms a tunable EDFRL over both C- and L-band wavelength ranges. Compared with tapered fiber tip, with a high transmission loss of $\sim$10dB, the transmission of a two-taper MZI is much lower ($<$1dB). This advantage improves lasers' performance, such as SMSR

and bandwidth. Thirdly, the hollow-core of a hollow-core photonic bandgap fiber (HC-PBF) is used as an FP cavity for the first time. Both low transmission loss and high finesse of such a tunable FP filter can implement stable single longitudinal mode (SLM) operation in a ring laser and obtain an SMSR of 51dB and a linewidth of 3.0kHz. The low transmission loss in the hollow core [110] makes it possible to extend a tunable FP cavity length to several millimeters, or even centimeters. Hence better laser performances could be obtained.

9.2 Future work

Some possible future research directions are presented as follows.

As mentioned in Chapters 3 and 4, for the distributed mode coupling measurement using OFDR system, there is a tradeoff between spectral resolution and spatial resolution due to finite rates of the TLS and the DAQ. The tunable laser's characters, such as coherent length, the frequency sweep range as well as the sweep speed, are related to the achievable spatial resolution and measurement range. The relations are shown in Eqs. (3.8) and (3.9). If we employ a tunable laser with better coherence, lower phase noises, wider frequency sweep range and faster tuning rate, OFDR will have better performances. In addition, the rate of DAQ should be improved. Therefore, the improvement of OFDR system will result in better spatial resolution for the distributed mode coupling measurement of fiber devices.

Using the proposed OFDR method, we can efficiently evaluate polarization preserv-

ing character of tapered PMFs. In this way, it is able to find a tapered PMF with smaller waist size and good polarization-maintaining property. One may make use of its high sensitivity and high birefringence to build sensors. First, tapered PMFs with asymmetric structures including two stress-applying components are highly sensitive to twist angle. If a light is launched to the axis of a tapered PMF at the input port, the transmission loss, PDL or other parameters may be measured as a function of the twist angle. Then these tapered PMFs could be used as torque sensors. Another application of taper PMFs is to be electrical current sensors by twining a tapered PMF around a straight copper wire. A tapered fiber becomes more pliable and can be bent at a much larger angle than SMF with very low losses. The ability of fiber tapers to guide light over bend radii of the order of a few micrometers has been exploited to minimize the sensor size [111]. Magnetic field sensors utilizing low-birefringence (LB) fibers have some disadvantages because LB fibers appeared to be very sensitive to external exposures, such as bending and squeezing. That means that, in order to achieve good accuracy for "field circumstances" (particularly in abroad temperature range), one have either to protect the optical scheme from external parameters changes or to install additional sensors to compensate correspondent errors. Although the birefringence in tapered PMFs is reduced, the value is still at a level of 10^{-4}. The high birefringence change could be useful for magnetic field detection. It is noted that a thin Teflon film may be coated on the tapered PMFs to reduce the thermal effect. Furthermore, based on the thermal and mechanical properties of SMF tapers and PMFs, tapered PMFs will have same

thermal response and several hundred times higher force sensitivity than that of PMFs. The tapering process may results in more inhomogeneous index characteristic in tapered PMFs than that in tapered SMFs, but the annealing treatment is helpful to significantly reduce the inhomogeneity, which may reduce polarization-maintaining property as well. We need to prove this tradeoff in the experiments. The autocorrelation wavelength shift indicates the refractive index difference between the fundamental mode and higher-order modes through mode coupling process; the cross-correlation wavelength shift indicates the refractive index change of the dominating mode (such as fast or slow mode in PMFs). Both the refractive index difference and the refractive index itself are linear functions of temperature and force, respectively. Using these parameters, tapered PMFs are able to simultaneous temperature and force sensors.

Appendix A

Cladding mode calculation in tapered fiber

For the cladding modes, $n_{air} < n_{eff} < n_{cl}$, we consider the bounded solutions with the core-cladding and cladding-air interfaces. A three-layer step-index fiber model with dispersion relation is proposed [37] and a list of clearer and ready-to-program relations is included [39].

The electromagnetic fields ψ, propagating in z-direction along the fiber, must satisfy the scalar wave equation, which is expressed in cylindrical coordinates (r, ϕ, z) as follows,

$$\left\{ \frac{\partial^2}{\partial r^2} + \frac{1}{r}\frac{\partial}{\partial r} + \frac{1}{r^2}\frac{\partial^2}{\partial \phi^2} + k^2 n^2 - \beta^2 \right\} \psi = 0, \tag{A.1}$$

where ψ represents electric or magnetic field, the wavenumber $k = \frac{2\pi}{\lambda}$ in terms of the free-space wavelength λ, n is the refractive index profile and β the propagation constant, $\beta = k n_{eff}$.

With defined modal parameters

$$u_1 = k \left(n_{co}^2 - n_{eff}^2 \right)^{\frac{1}{2}}, \tag{A.2a}$$

$$u_2 = k \left(n_{eff}^2 - n_{cl}^2 \right)^{\frac{1}{2}}, \tag{A.2b}$$

$$w_3 = k \left(n_{eff}^2 - n_{air}^2 \right)^{\frac{1}{2}}, \tag{A.2c}$$

the solution of Eq. (A.1) is as follows,

$$\psi = \begin{cases} AJ_\upsilon\left(u_1\rho\right)e^{i\upsilon\phi} & \text{if } 0 \le r \le \rho; \\ \left[BJ_\upsilon\left(u_1\rho\right) + CY_\upsilon\left(u_2\rho\right)\right]e^{i\upsilon\phi} & \text{if } \rho \le r \le \rho_{cl}; \\ DK_\upsilon\left(w_3\rho\right)e^{i\upsilon\phi} & \text{if } r \ge \rho_{cl}. \end{cases} \tag{A.3}$$

where A, B, C and D are constants, J_υ, Y_υ, and K_υ are the υth-order Bessel functions of the first kind and the seconde kind, and the modified Bessel function of the second kind, respectively. For the linearly polarized (LP) modes, LP_{0m} modes and LP_{1m} modes, $\upsilon = 0$ and $\upsilon = 1$, respectively. Therefore, the electric field and magnetic field components are given by

$$\Psi = \begin{cases} A_1 J_\upsilon\left(u_1\rho\right)e^{i\upsilon\phi} & \text{if } 0 \le r \le \rho; \\ \left[B_1 J_\upsilon\left(u_1\rho\right) + C_1 Y_\upsilon\left(u_2\rho\right)\right]e^{i\upsilon\phi} & \text{if } \rho \le r \le \rho_{cl}; \\ D_1 K_\upsilon\left(w_3\rho\right)e^{i\upsilon\phi} & \text{if } r \ge \rho_{cl}. \end{cases} \tag{A.4}$$

and

$$\Phi = \begin{cases} A_2 J_\upsilon\left(u_1\rho\right)e^{i\upsilon\phi} & \text{if } 0 \le r \le \rho; \\ \left[B_2 J_\upsilon\left(u_1\rho\right) + C_2 Y_\upsilon\left(u_2\rho\right)\right]e^{i\upsilon\phi} & \text{if } \rho \le r \le \rho_{cl}; \\ D_2 K_\upsilon\left(w_3\rho\right)e^{i\upsilon\phi} & \text{if } r \ge \rho_{cl}. \end{cases} \tag{A.5}$$

where A_j, B_j, C_j, and D_j $(j = 1, 2)$, are constants. The electric field and magnetic field are expressed as

$$\overrightarrow{E} = \left[E_r\hat{r} + E_\phi\hat{\phi} + E_z\hat{z}\right]e^{i(\beta z - \omega t)}, \tag{A.6a}$$

$$\overrightarrow{H} = \left[H_r\hat{r} + H_\phi\hat{\phi} + H_z\hat{z}\right]e^{i(\beta z - \omega t)}, \tag{A.6b}$$

with

$$E_r = \frac{\partial\Psi}{r\partial\phi} - \frac{\beta}{\omega\epsilon_i}\frac{\partial\Phi}{\partial r}, \tag{A.7a}$$

$$E_\phi = -\frac{\partial\Psi}{\partial r} - \frac{\beta}{\omega\epsilon_i}\frac{1}{r}\frac{\partial\Phi}{\partial\phi}, \tag{A.7b}$$

$$E_z = -\frac{1}{i\omega\epsilon_i}(k^2 n_i^2 - \beta^2)\Phi. \tag{A.7c}$$

and

$$H_r = \frac{\partial \Phi}{r\partial \phi} + \frac{\beta}{\omega\mu}\frac{\partial \Psi}{\partial r}, \tag{A.8a}$$

$$H_\phi = -\frac{\partial \Phi}{\partial r} + \frac{\beta}{\omega\mu}\frac{1}{r}\frac{\partial \Psi}{\partial \phi}, \tag{A.8b}$$

$$H_z = \frac{1}{i\omega\mu}(k^2 n_i^2 - \beta^2)\Psi. \tag{A.8c}$$

Substituting Eqs. (A.4) and (A.5) into the above Eqs. (A.7a)–(A.8c), all components are given by

$$E_r = \begin{cases} \left[\frac{iv}{r}A_1 J_v(u_1 r) - \frac{\beta u_1}{\omega\epsilon_{co}}A_2 J_v'(u_1 r)\right] e^{iv\phi} & \text{if } 0 \le r \le \rho; \\ \Big\{\frac{iv}{r}\left[B_1 J_v(u_2 r) + C_1 Y_v(u_2 r)\right] & \\ \quad - \frac{\beta u_2}{\omega\epsilon_{cl}}\left[B_2 J_v'(u_2 r) + C_2 Y_v'(u_2 r)\right]\Big\} e^{iv\phi} & \text{if } \rho \le r \le \rho_{cl}; \\ \left[\frac{iv}{r}D_1 K_v(w_3 r) - \frac{\beta w_3}{\omega\epsilon_{air}}D_2 K_v'(w_3 r)\right] e^{iv\phi} & \text{if } r \ge \rho_{cl}. \end{cases} \tag{A.9a}$$

$$E_\phi = \begin{cases} \left[-u_1 A_1 J_v'(u_1 r) - \frac{\beta}{\omega\epsilon_{co}}\frac{iv}{r}A_2 J_v(u_1 r)\right] e^{iv\phi} & \text{if } 0 \le r \le \rho; \\ \Big\{ - u_2\left[B_1 J_v'(u_2 r) + C_1 Y_v'(u_2 r)\right] & \\ \quad - \frac{\beta}{\omega\epsilon_{cl}}\frac{iv}{r}\left[B_2 J_v(u_2 r) + C_2 Y_v(u_2 r)\right]\Big\} e^{iv\phi} & \text{if } \rho \le r \le \rho_{cl}; \\ \left[-w_3 D_1 K_v'(w_3 r) - \frac{\beta}{\omega\epsilon_{air}}\frac{iv}{r}D_2 K_v(w_3 r)\right] e^{iv\phi} & \text{if } r \ge \rho_{cl}. \end{cases} \tag{A.9b}$$

$$E_z = \begin{cases} -\frac{u_1^2}{i\omega\epsilon_{co}}A_2 J_v(u_1 r) e^{iv\phi} & \text{if } 0 \le r \le \rho; \\ -\frac{u_2^2}{i\omega\epsilon_{cl}}\left[B_2 J_v(u_2 r) + C_2 Y_v(u_2 r)\right] e^{iv\phi} & \text{if } \rho \le r \le \rho_{cl}; \\ \frac{w_3^2}{i\omega\epsilon_{air}}D_2 K_v(w_3 r) e^{iv\phi} & \text{if } r \ge \rho_{cl}. \end{cases} \tag{A.9c}$$

$$H_r = \begin{cases} \left[\frac{iv}{r}A_2 J_v(u_1 r) + \frac{\beta u_1}{\omega\mu}A_1 J_v'(u_1 r)\right] e^{iv\phi} & \text{if } 0 \le r \le \rho; \\ \left\{\begin{array}{l} \frac{iv}{r}\left[B_2 J_v(u_2 r) + C_2 Y_v(u_2 r)\right] \\ -\frac{\beta u_2}{\omega\mu}\left[B_1 J_v'(u_2 r) + C_1 Y_v'(u_2 r)\right] \end{array}\right\} e^{iv\phi} & \text{if } \rho \le r \le \rho_{cl}; \\ \left[\frac{iv}{r}D_2 K_v(w_3 r) - \frac{\beta w_3}{\omega\mu}D_1 K_v'(w_3 r)\right] e^{iv\phi} & \text{if } r \ge \rho_{cl}. \end{cases} \tag{A.10a}$$

$$H_\phi = \begin{cases} \left[-u_1 A_2 J_v'(u_1 r) + \frac{\beta}{\omega\mu}\frac{iv}{r}A_1 J_v(u_1 r)\right] e^{iv\phi} & \text{if } 0 \le r \le \rho; \\ \left\{\begin{array}{l} -u_2\left[B_2 J_v'(u_2 r) + C_2 Y_v'(u_2 r)\right] \\ +\frac{\beta}{\omega\mu}\frac{iv}{r}\left[B_1 J_v(u_2 r) + C_1 Y_v(u_2 r)\right] \end{array}\right\} e^{iv\phi} & \text{if } \rho \le r \le \rho_{cl}; \\ \left[-w_3 D_2 K_v'(w_3 r) + \frac{\beta}{\omega\mu}\frac{iv}{r}D_1 K_v(w_3 r)\right] e^{iv\phi} & \text{if } r \ge \rho_{cl}. \end{cases} \tag{A.10b}$$

$$H_z = \begin{cases} \frac{u_1^2}{i\omega\mu}A_1 J_v(u_1 r) e^{iv\phi} & \text{if } 0 \le r \le \rho; \\ \frac{u_2^2}{i\omega\mu}\left[B_1 J_v(u_2 r) + C_1 Y_v(u_2 r)\right] e^{iv\phi} & \text{if } \rho \le r \le \rho_{cl}; \\ -\frac{w_3^2}{i\omega\mu}D_1 K_v(w_3 r) e^{iv\phi} & \text{if } r \ge \rho_{cl}. \end{cases} \tag{A.10c}$$

where $\epsilon_i = \epsilon_0 n_i^2$.

According to the boundary continuity condition at the core-cladding interface, where $r = \rho$, we have

$$\begin{aligned} -u_1 J_v'(u_1\rho)A_1 - \frac{\beta}{\omega\epsilon_0 n_{co}^2}\frac{iv}{\rho}J_v(u_1\rho)A_2 &= -u_2 J_v'(u_2\rho)B_1 - u_2 Y_v'(u_2\rho)C_1 \\ &\quad - \frac{\beta}{\omega\epsilon_0 n_{cl}^2}\frac{iv}{\rho}J_v(u_2\rho)B_2 - \frac{\beta}{\omega\epsilon_0 n_{cl}^2}\frac{iv}{\rho}Y_v(u_2\rho)C_2 \end{aligned} \tag{A.11a}$$

$$\frac{u_1^2}{i\omega\epsilon_0 n_{co}^2}J_v(u_1\rho)A_2 = \frac{u_2^2}{i\omega\epsilon_0 n_{cl}^2}J_v(u_2\rho)B_2 + \frac{u_2^2}{i\omega\epsilon_0 n_{cl}^2}Y_v(u_2\rho)C_2 \tag{A.11b}$$

$$\begin{aligned} -u_1 J_v'(u_1\rho)A_2 + \frac{\beta}{\omega\mu}\frac{iv}{\rho}J_v(u_1\rho)A_1 &= -u_2 J_v'(u_2\rho)B_2 - u_2 Y_v'(u_2\rho)C_2 \\ &\quad + \frac{\beta}{\omega\mu}\frac{iv}{\rho}J_v(u_2\rho)B_1 + \frac{\beta}{\omega\mu}\frac{iv}{\rho}Y_v(u_2\rho)C_1 \end{aligned} \tag{A.11c}$$

$$\frac{u_1^2}{i\omega\mu}J_v(u_1\rho)A_1 = \frac{u_2^2}{i\omega\mu}J_v(u_2\rho)B_1 + \frac{u_2^2}{i\omega\mu}Y_v(u_2\rho)C_1 \tag{A.11d}$$

We rewrite these equations in the following matrix form

$$\Re_1 \nu_1 = \Re_2 \nu_2, \tag{A.12}$$

where

$$\Re_1 \triangleq \begin{bmatrix} J'_\upsilon(u_2\rho) & Y'_\upsilon(u_2\rho) & \frac{\sigma_2}{u_2 n_{cl}^2 \rho} J_\upsilon(u_2\rho) & \frac{\sigma_2}{u_2 n_{cl}^2 \rho} Y_\upsilon(u_2\rho) \\ 0 & 0 & J_\upsilon(u_2\rho) & Y_\upsilon(u_2\rho) \\ \frac{\sigma_1}{u_2\rho} J_\upsilon(u_2\rho) & \frac{\sigma_1}{u_2\rho} Y_\upsilon(u_2\rho) & -J'_\upsilon(u_2\rho) & -Y'_\upsilon(u_2\rho) \\ J_\upsilon(u_2\rho) & Y_\upsilon(u_2\rho) & 0 & 0 \end{bmatrix} \tag{A.13}$$

$$\nu_1 \triangleq \begin{bmatrix} B_1 \\ C_1 \\ B_2 \\ C_2 \end{bmatrix} \tag{A.14}$$

$$\begin{aligned} \Re_2 &\triangleq \begin{bmatrix} \frac{u_1}{u_2} J'_\upsilon(u_1\rho) & \frac{\sigma_2}{u_2 n_{co}^2 \rho} J_\upsilon(u_1\rho) \\ 0 & \frac{u_1^2 n_{cl}^2}{u_2^2 n_{co}^2 x} J_\upsilon(u_1\rho) \\ \frac{\sigma_1}{u_2\rho} J_\upsilon(u_1\rho) & -\frac{u_1}{u_2} J'_\upsilon(u_1\rho) \\ \frac{u_1^2}{u_2^2} J_\upsilon(u_1\rho) & 0 \end{bmatrix} \\ &= \frac{u_1^2}{u_2} J_\upsilon(u_1\rho) \begin{bmatrix} J & \frac{\sigma_2}{u_1^2 n_{co}^2 \rho} \\ 0 & \frac{n_{cl}^2}{u_2 n_{co}^2} \\ \frac{\sigma_1}{u_1^2 \rho} & -J \\ \frac{1}{u_2} & 0 \end{bmatrix} \end{aligned} \tag{A.15}$$

$$\nu_2 \triangleq \begin{bmatrix} A_1 \\ A_2 \end{bmatrix} \tag{A.16}$$

$$\tag{A.17}$$

with

$$J \triangleq \frac{J'_\upsilon(u_1\rho)}{u_1 J_\upsilon(u_1\rho)} \tag{A.18}$$

$$\sigma_1 \triangleq \frac{i\beta\upsilon}{\omega\mu} = \frac{i\upsilon n_{eff}}{Z_0} \tag{A.19}$$

$$\sigma_2 \triangleq \frac{i\beta\upsilon}{\omega\epsilon_0} = i\upsilon n_{eff} Z_0 \tag{A.20}$$

with $Z_0 = \sqrt{\frac{\mu_0}{\epsilon_0}} = 377\Omega$.

According to boundary continuity condition at the cladding-air interface, where $r = \rho_{cl}$, we have

$$
\begin{aligned}
&- u_2 J'_\upsilon(u_2\rho_{cl})B_1 - u_2 Y'_\upsilon(u_2\rho_{cl})C_1 - \frac{\beta}{\omega\epsilon_0 n_{cl}^2}\frac{i\upsilon}{\rho_{cl}} J_\upsilon(u_2\rho_{cl})B_2 \\
&\quad - \frac{\beta}{\omega\epsilon_0 n_{cl}^2}\frac{i\upsilon}{\rho_{cl}} Y_\upsilon(u_2\rho_{cl})C_2 = -w_3 K'_\upsilon(w_3\rho_{cl})D_1 - \frac{\beta}{\omega\epsilon_0 n_{air}^2}\frac{i\upsilon}{\rho_{cl}} K_\upsilon(w_3\rho_{cl})D_2 \qquad \text{(A.21a)} \\
&- \frac{u_2^2}{i\omega\epsilon_0 n_{cl}^2} J_\upsilon(u_2\rho_{cl})B_2 - \frac{u_2^2}{i\omega\epsilon_0 n_{cl}^2} J_\upsilon(u_2\rho_{cl})C_2 = \frac{w_3^2}{i\omega\epsilon_0 n_{air}^2} K_\upsilon(w_3\rho_{cl})D_2 \qquad \text{(A.21b)} \\
&- u_2 J'_\upsilon(u_2\rho_{cl})B_2 - u_2 Y'_\upsilon(u_2\rho_{cl})C_2 + \frac{\beta}{\omega\mu}\frac{i\upsilon}{\rho_{cl}} J_\upsilon(u_2\rho_{cl})B_1 \\
&\quad + \frac{\beta}{\omega\mu}\frac{i\upsilon}{\rho_{cl}} Y_\upsilon(u_2\rho_{cl})C_1 = -w_3 K'_\upsilon(w_3\rho_{cl})D_2 + \frac{\beta}{\omega\mu}\frac{i\upsilon}{\rho_{cl}} K_\upsilon(w_3\rho_{cl})D_1 \qquad \text{(A.21c)} \\
&\frac{u_2^2}{i\omega\mu} J_\upsilon(u_2\rho_{cl})B_1 + \frac{u_2^2}{i\omega\mu} Y_\upsilon(u_2\rho_{cl})C_1 = -\frac{w_3^2}{i\omega\mu} K_\upsilon(w_3\rho_{cl})D_1 \qquad \text{(A.21d)}
\end{aligned}
$$

We write these equations in a more compact form using matrices, as follows,

$$\Re_3 \nu_1 = \Re_4 \nu_3, \qquad \text{(A.22)}$$

where

$$\Re_3 \triangleq \begin{bmatrix} J'_v(u_2\rho_{cl}) & Y'_v(u_2\rho_{cl}) & \frac{\sigma_2}{u_2 n_{cl}^2 \rho_{cl}} J_v(u_2\rho_{cl}) & \frac{\sigma_2}{u_2 n_{cl}^2 \rho_{cl}} Y_v(u_2\rho_{cl}) \\ 0 & 0 & J_v(u_2\rho_{cl}) & Y_v(u_2\rho_{cl}) \\ \frac{\sigma_1}{u_2\rho_{cl}} J_v(u_2\rho_{cl}) & \frac{\sigma_1}{u_2\rho_{cl}} Y_v(u_2\rho_{cl}) & -J'_v(u_2\rho_{cl}) & -Y'_v(u_2\rho_{cl}) \\ J_v(u_2\rho_{cl}) & Y_v(u_2\rho_{cl}) & 0 & 0 \end{bmatrix} \tag{A.23}$$

$$\Re_4 \triangleq \begin{bmatrix} \frac{w_3}{u_2} K'_v(w_3\rho_{cl}) & \frac{\sigma_2}{u_2\rho_{cl} n_{air}^2} K_v(w_3\rho_{cl}) \\ 0 & \frac{w_3^2 n_{cl}^2}{u_2^2 n_{air}^2} K_v(w_3\rho_{cl}) \\ \frac{\sigma_1}{u_2\rho_{cl}} K_v(w_3\rho_{cl}) & -\frac{w_3}{u_2} K'_v(w_3\rho_{cl}) \\ \frac{w_3^2}{u_2^2} K_v(w_3\rho_{cl}) & 0 \end{bmatrix} \tag{A.24}$$

$$= \frac{w_3^2}{u_2} K_v(w_3\rho_{cl}) \begin{bmatrix} K & \frac{\sigma_2}{w_3^2 n_{air}^2 \rho_{cl}} \\ 0 & -\frac{n_{cl}^2}{u_2 n_{air}^2} \\ \frac{\sigma_1}{w_3^2\rho_{cl}} & -K \\ -\frac{1}{u_2} & 0 \end{bmatrix} \tag{A.25}$$

$$\nu_3 \triangleq \begin{bmatrix} D_1 \\ D_2 \end{bmatrix} \tag{A.26}$$

with

$$K \triangleq \frac{K'_v(w_3\rho_{cl})}{w_3 K_v(w_3\rho_{cl})}. \tag{A.27}$$

With Eqs. (A.12) and (A.22), we have

$$\Re_3 \Re_1^{-1} \Re_2 \nu_2 = \Re_4 \nu_3, \tag{A.28}$$

where $\Re_1^{-1}$ is calculated and expressed as

$$\Re_1^{-1} = \frac{1}{J'_v(u_2\rho)Y_v(u_2\rho) - J_v(u_2\rho)Y'_v(u_2\rho)} \begin{bmatrix} Y_v(u_2\rho) & -\frac{\sigma_2}{u_2 n_{cl}^2 \rho} Y_v(u_2\rho) & 0 & -Y'_v(u_2\rho) \\ -J_v(u_2\rho) & \frac{\sigma_2}{u_2 n_{cl}^2 \rho} J_v(u_2\rho) & 0 & J'_v(u_2\rho) \\ 0 & -Y'_v(u_2\rho) & -Y_v(u_2\rho) & \frac{\sigma_1}{u_2\rho} Y_v(u_2\rho) \\ 0 & J'_v(u_2\rho) & J_v(u_2\rho) & -\frac{\sigma_1}{u_2\rho} J_v(u_2\rho) \end{bmatrix} \tag{A.29}$$

Eq. (A.28) is rewrited as

$$\xi_0 \begin{bmatrix} r_\upsilon & -\frac{\sigma_2}{u_2 n_{cl}^2}(\frac{1}{\rho_{cl}} q_\upsilon + \frac{1}{\rho} r_\upsilon) & -\frac{\sigma_2}{u_2 n_{cl}^2 \rho_{cl}} p_\upsilon & \frac{\sigma_1\sigma_2}{u_2^2 n_{cl}^2 \rho\rho_{cl}} p_\upsilon(\rho_{cl}) - s_\upsilon \\ 0 & -q_\upsilon & -p_\upsilon & \frac{\sigma_1}{u_2\rho} p_\upsilon \\ \frac{\sigma_1}{u_2\rho_{cl}} p_\upsilon(\rho_{cl}) & -\frac{\sigma_1\sigma_2}{u_2^2 n_{cl}^2 \rho\rho_{cl}} p_\upsilon(\rho_{cl}) + s_\upsilon & r_\upsilon & -\frac{\sigma_1}{u_2}(\frac{1}{\rho_{cl}} q_\upsilon + \frac{1}{\rho} r_\upsilon) \\ p_\upsilon(\rho_{cl}) & -\frac{\sigma_2}{u_2 n_{cl}^2 \rho} p_\upsilon(\rho_{cl}) & 0 & -q_\upsilon \end{bmatrix}$$

$$\begin{bmatrix} J & \frac{\sigma_2}{u_1^2 n_{co}^2 \rho} \\ 0 & \frac{n_{cl}^2}{u_2 n_{co}^2} \\ \frac{\sigma_1}{u_1^2 \rho} & -J \\ \frac{1}{u_2} & 0 \end{bmatrix} \begin{bmatrix} A_1 \\ A_2 \end{bmatrix} = \begin{bmatrix} K & \frac{\sigma_2}{w_3^2 n_{air}^2 \rho_{cl}} \\ 0 & -\frac{n_{cl}^2}{u_2 n_{air}^2} \\ \frac{\sigma_1}{w_3^2 \rho_{cl}} & -K \\ -\frac{1}{u_2} & 0 \end{bmatrix} \begin{bmatrix} D_1 \\ D_2 \end{bmatrix} \tag{A.30}$$

with

$$p_\upsilon \triangleq J_\upsilon(u_2\rho_{cl}) Y_\upsilon(u_2\rho) - J_\upsilon(u_2\rho) Y_\upsilon(u_2\rho_{cl}), \tag{A.31}$$

$$q_\upsilon \triangleq J_\upsilon(u_2\rho_{cl}) Y'_\upsilon(u_2\rho) - J'_\upsilon(u_2\rho) Y_\upsilon(u_2\rho_{cl}), \tag{A.32}$$

$$r_\upsilon \triangleq J'_\upsilon(u_2\rho_{cl}) Y_\upsilon(u_2\rho) - J_\upsilon(u_2\rho) Y'_\upsilon(u_2\rho_{cl}), \tag{A.33}$$

$$s_\upsilon \triangleq J'_\upsilon(u_2\rho_{cl}) Y'_\upsilon(u_2\rho) - J'_\upsilon(u_2\rho) Y'_\upsilon(u_2\rho_{cl}), \tag{A.34}$$

$$\xi_0 \triangleq \frac{u_1^2 J_\upsilon(u_1\rho)}{w_3^2 K_\upsilon(w_3\rho_{cl})[J'_\upsilon(u_2\rho) Y_\upsilon(u_2\rho) - J_\upsilon(u_2\rho) Y'_\upsilon(u_2\rho)].} \tag{A.35}$$

Eq. (A.28) is calculated, which is given by

$$\xi_0 \begin{bmatrix} \frac{\sigma_1\sigma_2 u_{21}}{u_2 n_{cl}^2 \rho\rho_{cl}} p_\upsilon + J r_\upsilon - \frac{1}{u_2} s_\upsilon & \frac{\sigma_2}{u_2 n_{cl}^2 \rho_{cl}} J p_\upsilon - \frac{\sigma_2}{u_2^2 n_{co}^2 \rho_{cl}} q_\upsilon - \frac{\sigma_2 u_{21}}{n_{co}^2 \rho} r_\upsilon \\ \frac{\sigma_1 u_{21}}{\rho} p_\upsilon & J p_\upsilon - \frac{n_{cl}^2}{u_2 n_{co}^2} q_\upsilon \\ \frac{\sigma_1}{u_2\rho_{cl}}(J p_\upsilon - \frac{1}{u_2} q_\upsilon) - \frac{\sigma_1 u_{21}}{\rho} r_\upsilon & -\frac{\sigma_1\sigma_2 u_{21}}{u_2 n_{co}^2 \rho\rho_{cl}} p_\upsilon - J r_\upsilon + \frac{n_{cl}^2}{u_2 n_{co}^2} s_\upsilon \\ J p_\upsilon - \frac{1}{u_2} q_\upsilon & -\frac{\sigma_2 u_{21}}{n_{co}^2 \rho} p_\upsilon \end{bmatrix}$$

$$\begin{bmatrix} A_1 \\ A_2 \end{bmatrix} = \begin{bmatrix} K & \frac{\sigma_2}{w_3^2 n_{air}^2 \rho_{cl}} \\ 0 & -\frac{n_{cl}^2}{u_2 n_{air}^2} \\ \frac{\sigma_1}{w_3^2 \rho_{cl}} & -K \\ -\frac{1}{u_2} & 0 \end{bmatrix} \begin{bmatrix} D_1 \\ D_2 \end{bmatrix} \tag{A.36}$$

with

$$u_{21} \triangleq \frac{1}{u_2^2} - \frac{1}{u_1^2}, \tag{A.37}$$

$$u_{32} \triangleq \frac{1}{u_2^2} + \frac{1}{w_3^2}. \tag{A.38}$$

The solution is

$$\zeta_0 = \zeta_0', \tag{A.39}$$

where

$$\zeta_0 = \frac{1}{\sigma_2} \frac{u_2(JK + \frac{\sigma_1\sigma_2 u_{21}u_{32}}{n_{cl}^2\rho\rho_{cl}})p_\upsilon - Kq_\upsilon + Jr_\upsilon - \frac{1}{u_2}s_\upsilon}{-u_2(\frac{u_{32}}{n_{cl}^2\rho_{cl}}J - \frac{u_{21}}{n_{co}^2\rho}K)p_\upsilon + \frac{u_{32}}{n_{co}^2\rho_{cl}}q_\upsilon + \frac{u_{21}}{n_{co}^2\rho}r_\upsilon}, \tag{A.40}$$

$$\zeta_0' = \sigma_1 \frac{u_2(\frac{u_{32}}{\rho_{cl}}J - \frac{u_{21}n_{air}^2}{n_{cl}^2\rho}K)p_\upsilon - \frac{u_{32}}{\rho_{cl}}q_\upsilon - \frac{u_{21}}{\rho}r_\upsilon}{u_2(\frac{n_{air}^2}{n_{cl}^2}JK + \frac{\sigma_1\sigma_2 u_{21}u_{32}}{n_{co}^2\rho\rho_{cl}})p_\upsilon - \frac{n_{air}^2}{n_{co}^2}Kq_\upsilon + Jr_\upsilon - \frac{n_{cl}^2}{u_2 n_{co}^2}s_\upsilon}. \tag{A.41}$$

Bibliography

[1] J. D. Love, W. M. Henry, W. J. Stewart, R. J. Black, S. Lacroix, and F. Gonthier. Tapered single-mode fibres and devices - part 1. adiabaticity criteria. *IEE Proc.-J Optoelectron*, 138:343–354, 1991.

[2] R. Hui and M. O′Sullivan. *Fiber Optic Measurement Techniques*. Elsevier, 2009.

[3] C. A. Villarruel and R. P. Moeller. Fused single-mode fiber access couplers. *Electron. Lett.*, 17:243–244, 1981.

[4] B. S. Kawasaki, K. O. Hill, and R. G. Lamont. Biconical-taper single mode fiber coupler. *Opt. Lett.*, 6:327–328, 1981.

[5] K. Okamoto. Single-polarization operation in highly birefringent optical fibers. *Appl. Opt.*, 23:2638–2642, 1984.

[6] W. K. Burns, M. Abebe, and C. A. Villarruel. Parabolic model for shape of fiber taper. *Appl. Opt.*, 24:2753–2755, 1985.

[7] J. Bures, S. Lacroix, and J. Lapierre. Analysis of a fused biconical single-mode fiber optic coupler. *Appl. Opt.*, 22:1918–1922, 1983.

[8] R. J. Black, S. Lacroix, F. Gonthier, and J. D. Love. Tapered single-mode fibres and devices–Part 2: Experimental and theoretical quantification. *IEE Proc.-J Optoelectron*, 138:355–364, 1991.

[9] T. A. Birks and Y. W. Li. The shape of fiber tapers. *J. Lightwave Technol.*, 10:432–438, 1992.

[10] J. Ward, D. O'Shea, B. J. Shortt, M. J. Morrissey, K. Deasy, and S. Nic Chormaic. Heat-and-pull rig for fiber taper fabrication. *Rev. Sci. Instrum.*, 77:083105, 2006.

[11] H. S. Haddock, P. M. Shankar, and R. Mutharasan. Fabrication of biconical tapered optical fibers using hydrofluoric acid. *Mater. Sci. Eng. B*, 97:87–93, 2003.

[12] H.S. Mackenzie and F.P. Payne. Evanescent field amplification in a tapered single-mode optical fiber. *Electron. Lett.*, 26:130–132, 1990.

[13] J. C. Knight, G. Cheung, F. Jacques, and T. A. Birks. Phase-matched excitation of whispering-gallery-mode resonances by a fiber taper. *Opt. Lett.*, 22:1129–1131, 1997.

[14] M. Cai, O. Painter, and K. J. Vahala. Observation of critical coupling in a fiber taper to a silica-microsphere. whispering-gallery mode system. *Phys. Rev. Lett.*, 85:74–77, 2000.

[15] M. Cai, O. Painter, K. J. Vahala, and P. C. Sercel. Fiber-coupled microsphere laser. *Opt. Lett.*, 25:1430–1432, 2000.

[16] D. Donlagic. In-line higher order mode filters based on long highly uniform fiber tapers. *J. Lightwave Technol.*, 24:3532–3539, 2006.

[17] Y. Jung, G. Brambilla, and D. J. Richardson. Broadband single-mode operation of standard optical fibers by using a sub-wavelength optical wire filter. *Opt. Express*, 16:14661–14667, 2008.

[18] K. Q. Kieu and M. Mansuripur. Biconical fiber taper sensors. *IEEE Photon. Technol. Lett.*, 18:2239 – 2241, 2006.

[19] F. J. Arregui, I. R. Matas, and M. Lopez-Amo. Optical fiber strain gauge based on a tapered single-mode fiber. *Sensors and Actuators A: Physical*, 79:90–96, 2000.

[20] S. Zhu, F. Pang, and T. Wang. Single-mode tapered optical fiber for temperature sensor based on multimode interference. In *Optical Sensors and Biophotonics III, in Proceedings of the SPIE*, page 8311, Shanghai, China, 2011.

[21] C. Bariain, I. R. Matas, F. J. Arregui, and M. Lopez-Amo. Optical fiber humidity sensor based on a tapered fiber coated with agarose gel. *Sensors and Actuators B.*, 69:127–131, 2000.

[22] Z. Tian, S. S. H. Yam, J. Barnes, W. Bock, P. Greig, J. M. Fraser, H.-P. Loock, and R. D. Oleschuk. Refractive index sensing with machzehnder interferometer based on concatenating two single-mode fiber tapers. *IEEE Photon. Technol. Lett.*, 20:626–628, 2008.

[23] Z. Tian, S. S. H. Yam, and H.-P. Loock. Refractive index sensor based on an abrupt taper michelson interferometer in a single-mode fiber. *Opt. Lett.*, 33:1105–1107, 2008.

[24] Z. Tian and S. S.-H. Yam. In-line abrupt taper optical fiber mach-zehnder interferometric strain sensor. *IEEE Photon. Technol. Lett.*, 21:161–163, 2009.

[25] R. J. Black and R. Bourbonnais. Core-mode cutoff for finite-cladding lightguides. *Inst. Elect. Eng. Proc.*, 133:377–384, 1986.

[26] F. Gonthier, J. Lapierre, C. Veilleux, S. Lacroix, and J. Bures. Investigation of power oscillations along tapered monomode fibers. *Appl. Opt.*, 26:444–449, 1987.

[27] S. Lacroix, R. Bourbonnais, F. Gonthier, and J. Bures. Tapered monomode optical fibers: Understanding large power transfer. *Appl. Opt.*, 25:4421–4425, 1986.

[28] K. Kieu and M. Mansuripur. Tuning of fiber lasers by use of a single-mode biconic fiber taper. *Opt. Lett.*, 31:2435–2437, 2006.

[29] A. J. Fielding, K. Edinger, and C. C. Davis. Experimental observation of mode evolution in single-mode tapered optical fibers. *J. Lightwave Technol.*, 17:1649–1656, 1999.

[30] A. Iocco, H. G. Limberger, R. P. Salathe, L. A. Everall, K. E. Chisholm, J. A. R. Williams, and I. Bennion. Bragg grating fast tunable filter for wavelength division multiplexing. *J. Lightwave Technol.*, 17:1217–1221, 1999.

[31] H. G. Limberger, N. Hong Ky, D. M. Costantini, R. P. Salath′e, C. A. P. Muller, and C. R. Fox. Efficient active bragg grating tunable filters. In *in Proc. OFS′97, OSA Tech. Dig. Series,OSA Topical Meeting*, Williamsburg,USA, 1997.

[32] X. Dong, P. Shum, X. Yang, M. Lim, and C. Chan. Bandwidth-tunable filter and spacing-tunable comb filter with chirped-fiber bragg gratings. *Opt. Commun.*, 259:645–648, 2006.

[33] J. Stone and L. W. Stulz. Pigtailed high finesse tunable FP interferometer with large, medium and small FSR. *Electron. Lett.*, 23:781–783, 1987.

[34] T. Watanabe, Y. Inoue, K. Kaneko, N. Ooba, and T. Kurihara. Polymeric arrayed-waveguide grating multiplexer with wide tuning range. *Electron. Lett.*, 33:1547–1548, 1997.

[35] A. Castillo-Guzman, J. E. Antonio-Lopez, R. Selvas-Aguilar, D. A. May-Arrioja, J. Estudillo-Ayala, and P. LiKamWa. Widely tunable erbium-doped fiber laser based on multimode interference effect. *Opt. Express*, 18:591–597, 2010.

[36] G. Sun, Y. Zhou, Y. Hu, and Y. Chung. Broadly tunable fiber laser based on merged sagnac and intermodal interferences in few-mode high-birefringence fiber loop mirror. *IEEE Photon. Technol. Lett.*, 22:766–768, 2010.

[37] C. Tsao. *Optical Fiber Waveguide Analysis*. Oxford University Press, New York, 1992.

[38] A. Yariv. *Optical Electronics in modern communications*. Oxford University Press, Inc., 1997.

[39] T. Erdogan. Cladding-mode resonances in short- and long-period fiber grating filters. *J. Opt. Soc. Am. A*, 14:1760–1773, 1997.

[40] G. Brambilla, V. Finazzi, and D. Richardson. Ultra-low-loss optical fiber nanotapers. *Opt. Express*, 12:2258–2263, 2004.

[41] L. C. Ozcan, V. Treanton, F. Guay, and R. Kashyap. Highly symmetric optical fiber tapers fabricated with a CO_2 laser. *IEEE Photon. Technol. Lett.*, 19:656–658, 2007.

[42] T. Pangaribun, K. Yamada, S. Jiang, H. Ohsawa, and M. Ohtsu. Reproducible fabrication technique of nanometric tip diameter fiber probe for photon scanning tunneling microscope. *Jpn. J. Appl. Phys.*, 31:L1302–L1304, 1992.

[43] http://cp.literature.agilent.com/litweb/pdf/5990-3281en.pdf.

[44] N. Gu, C. Li, L. Sun, Z. Liu, Y. Sun, and L Xu. Controllable fabrication of fiber nano-tips by dynamic chemical etching based on siphon principle. *J. Vac. Sci. Technol. B*, 22:2283–2285, 2004.

[45] R. Stockle, C. Fokas, V. Deckert, R. Zenobi, B. Sick, B. Hecht, and U. P. Wild. High-quality near-field optical probes by tube etching. *Appl. Phys. Lett.*, 75:160–162, 1999.

[46] X. Huo, S. Pan, and S. Wu. Fabrication of pure silica core multimode ultraviolet optical fibre probes by tube etching. *Chinese Phys. Lett.*, 24:2876–2878, 2007.

[47] C. W. Extrand and S. I. Moon. Critical meniscus height of liquids at the circular edge of cylindrical rods and disks. *Langmuir*, 25:992–996, 2009.

[48] U. Roth, O. Paulus, and U. Menyes. Surface activity of amphiphiles in hydrogen fluoride water solutions. *Colloid Polym. Sci.*, 273:800–806, 1995.

[49] M. E. Froggatt, D. K. Gifford, S. Kreger, M. Wolfe, and B. J. Soller. Characterization of polarization-maintaining fiber using high-sensitivity optical-frequency-domain reflectometry. *J. Lightwave Technol.*, 24:4149–4154, 2006.

[50] Robert W. Boyd. *Nonlinear Optics, 3rd ed.* Elsevier Inc.,Academic Press, New York, 2008.

[51] M. Born and E. Wolf. *Principles of Optics,7th ed.* Cambridge University Press, New York, 1999.

[52] G. P. Agrawal. *Fiber-Optic Communications Systems.* Wiley, 2002.

[53] E. G. Neumann. Analysis of the backscattering method for testing optical fiber cables. *Electron. Commun. (AEU)*, 34:157–160, 1980.

[54] D. Derickson. *Fiber Optic Test and Measurement*. Prentice Hall PTR, New Jersey, 1998.

[55] C. Hentschel. *Fiber optic handbook*. Hewlett-Packard, 1989.

[56] B. J. Soller, D. K. Gifford, M. S.Wolfe, and M. E. Froggatt. High resolution optical frequency domain reflectometry for characterization of components and assemblies. *Opt. Express*, 13:666–674, 2005.

[57] W. Eickhoff and R. Ulrich. Optical frequency domain reflectometry in single-mode fiber. *Appl. Phys. Lett.*, 39:693–695, 1981.

[58] U. Glombitza and E. Brinkmeyer. Coherent frequency domain reflectomtry for charactization of single-mode integrated optical waveguides. *J. Lightwave Technol.*, 11:1377–1384, 1993.

[59] M. Froggatt, D. Gifford, S. Kreger, M. Wolfe, and B. Soller. Distributed strain and temperature discrimination in unaltered polarization maintaining fiber. In *in Proceedings of the 18th Optical Fiber Sensors Conference*, page ThC5, Cancun, Mexico, 2006.

[60] G. Mussi, P. Stamp, N. Gisin, R. Passy, and J. P. von der Weid. Polarization effects in coherent frequency-domain reflectometry. *IEEE Photon. Tech. Letters*, 8:1377–1384, 1996.

[61] P. Oberson, B. Huttner, O. Guinnard, L. Guinnard, G. Ribordy, and N. Gisin. Optical frequency domain reflectometry with a narrow linewidth fiber laser. *IEEE Photon. Tech. Letters*, 12:867–869, 2000.

[62] M. Froggatt and J. Moore. High-spatial-resolution distributed strain measurement in optical fiber with rayleigh scatter. *Appl. Opt.*, 37:1735–1740, 1998.

[63] S. Kreger, D. Gifford, M. Froggatt, B. Soller, and M. Wolfe. High resolution distributed strain or temperature measurements in single- and multi-mode fiber using swept-wavelength interferometry. In *OFS 18 Technical Digest*, page ThE42, Cancun, Mexico, 2006.

[64] D. Marcuse. *Light Transmission Optics*. Van Nostrand Reinhold, New York, 1982.

[65] L. G. Cohen. Comparison of single-mode fiber dispersion measurement techniques. *J. Lightw. Technol.*, 3:958–966, 1985.

[66] M. J. Adams. *An Introduction to Optical Waveguides*. Wiley, New York, 1981.

[67] I. H. Malitson. Interspecimen comparison of the refractive index of fused silica. *J. Opt. Soc. Am.*, 55:1205–1208, 1965.

[68] A. W. Snyder and J. D. Love. *Optical Waveguide Theory*. Chapman and Hall, London, 1983.

[69] I. P. Kaminow. Polarization in optical fibers. *IEEE J. Quantum Electron.*, 17:15–22, 1981.

[70] B. H. Lee and J. Nishii. Dependence of fringe spacing on the grating separation in a long-period fiber grating pair. *Laser Phys.*, 38:3450–3459, 1999.

[71] S. Xie, X. Bao, and L. Chen. Distributed fiber beat length, birefringence and differential group delay measurement using BOTDA technique. *in Proc. SPIE*, 7753:7753A6, doi:10.1117/12. 899543., 2011.

[72] X. Wang, W. Li, L. Chen, and X. Bao. Distributed mode coupling measurement along tapered single-mode fibers with optical frequency-domain reflectometry. *J. Lightwave Technol.*, 30:1499–1508, 2012.

[73] T. Wieduwilt, S. Brückner, and H. Bartelt. High force measurement sensitivity with fiber bragg gratings fabricated in uniform-waist fiber tapers. *Meas. Sci. Technol.*, 22:075201, 2011.

[74] F. Pigeon, S. Pelissier, A. Mure-Ravaud, H. Gagnarie, and C. Veillas. Optical fiber young modulus measurement using an optical method. *Electron. Lett.*, 28:1034–1035, 1992.

[75] Y. Jung, G. Brambilla, and D. J. Richardson. Polarization-maintaining optical microfiber. *Opt. Lett.*, 35:2034–2036, 2010.

[76] Datasheet of Panda PMF. http://www.corning.com/assets/0/965/989/1081/b6e2ce01-9222-497b-9dfd-2c7ab82a80cf.pdf.

[77] J. Noda, K. Okamoto, and Y. Sasaki. Polarization-maintaining fibers and their applications. *J. Lightwave Technol.*, 4:1071–1089, 1986.

[78] T. Hosaka, Y. Sasaki, K. Okamoto, and J. Noda. Stress-applied polarization-maintaining optical fibers-design and fabrication. *Electronics and Communications in Japan (Part II: Electronics)*, 68:37–47, 1985.

[79] S. C. Rashleigh and M. J. Marrone. Influence of the fiber diameter on the stress birefringence in high-birefringence fibers. *Opt. Lett.*, 8:292–294, 1983.

[80] Y. Li and X. Bao. The observation of comb-like transmission spectrum from a tapered single mode fiber tip. *Appl. Phys. Lett.*, 93:261107, 2008.

[81] G. P. Agrawal and N. K. Dutta. *Semiconductor lasers*. Van Nostrand Reinhold, New York, 1993.

[82] M. J. F. Digonnet. *Rare-Earth Doped Fiber Lasers and Amplifiers*. Marcel Dekker, Inc., New York, 1993.

[83] E. Desurvire. *Erbium-Doped Fiber Amplifiers: Principles and Applications*. John Wiley and Sons, Inc., New York, 1994.

[84] C. C. Lee, Y. K. Chen, and S. K. Liaw. Single-longitudinal-mode fiber laser with a passive multiple-ring cavity and its application for video transmission. *Opt. Lett.*, 23:358–360, 1998.

[85] C. H. Yeh, T. T. Huang, H. C. Chien, C. H. Ko, and S. Chi. Tunable s-band erbium-doped triple-ring laser with single-longitudinal-mode operation. *Opt. Express*, 15:382–386, 2007.

[86] Y. W. Song, S. A. Havstad, D. Starodubov, Y. Xie, A. E. Willner, and W. J. Feinberg. 40nm-wide tunable fiber ring laser with single-mode operation using a highly stretchable fbg. *IEEE Photon. Technol. Lett.*, 13:1167–1169, 2001.

[87] J. Liu, J. P. Yao, J. Yao, and T. H. Yeap. Single-longitudinal-mode multiwavelength fiber ring laser. *IEEE Photon. Technol. Lett.*, 16:1020–1022, 2004.

[88] K. Zhang and J. U. Kang. C-band wavelength-swept single-longitudinal-mode erbium-doped fiber ring laser. *Opt. Express*, 16:14173–14179, 2008.

[89] M. Tang, X. Tian, S. Fu X. Lu, P. P. Shum, Z. Zhang, M. Liu, Y. Cheng, and J. Liu. Single-frequency 1060nm semiconductor-optical-amplifier-based fiber laser with 40 nm tuning range. *Opt. Lett.*, 34:2204–2206, 2009.

[90] X. P. Cheng, P. Shum, C. H. Tse, J. L. Zhou, M. Tang, W. C. Tan, R. F. Wu, and J. Zhang. Single-longitudinal-mode erbium-doped fiber laser based on high finesse fiber bragg grating fabry-perot etalon. *IEEE Photon. Technol. Lett.*, 20:976–978, 2008.

[91] D. Chen, H. Fu, and W. Liu. Single-longitudinal-mode erbium-doped fiber laser based on a fiber bragg grating fabry-perot filter. *Laser Phys.*, 17:1246–1248, 2007.

[92] T. A. Birks, P. St. J. Russell, and C. N. Pannell. Low power acousto-optic device based on a tapered single mode fiber. *IEEE Photon. Technol. Lett.*, 6:725–727, 1994.

[93] H. Y. Choi, M. J. Kim, and B. H. Lee. All-fiber mach-zehnder type interferometers formed in photonic crystal fiber. *Opt. Express*, 15:5711–5720, 2007.

[94] X. Wang, Y. Li, and X. Bao. Tunable ring laser using a tapered single mode fiber tip. *Appl. Opt.*, 48:6827–6831, 2009.

[95] T. Wei, X. Lan, and H. Xiao. Fiber inline core-cladding-mode mach-zehnder interferometer fabricated by two-point CO_2 laser irradiations. *IEEE Photon. Technol. Lett.*, 21:669–671, 2009.

[96] L. C. Bobb, P. M. Shankar, and H. D. Krumboltz. Bending effects in biconically tapered single-mode fibers. *IEEE Photon. Technol. Lett.*, 8:1084–1090, 1990.

[97] O. Frazão, R. Falate, J. L. Fabris, J. L. Santos, L. A. Ferreira, and F. M. Araújo. Optical inclinometer based on a single long-period fiber grating combined with a fused taper. *Opt. Lett.*, 31:2960 –2962, 2006.

[98] L. Shao and J. Albert. Compact fiber-optic vector inclinometer. *Opt. Lett.*, 35:1034 –1036, 2010.

[99] H. F. Taylor. *Fiber optic Fabry-Perot sensors,F. T. S. Yu and S. Yin, eds.* Marcel Dekker, New York, 2002.

[100] H. Singh and J. S. Sirkis. Simultaneously measuring temperature and strain using optical fiber microcavities. *J. Lightwave Technol.*, 15:647–653, 1997.

[101] Y. Zhu and A. B. Wang. Miniature fiber-optic pressure sensor. *IEEE Photon. Technol. Lett.*, 17:447–449, 2005.

[102] T. K. Gangopadhyay and P. J. Henderson. Vibration: history and measurement with an extrinsic fabry-perot sensor with solid-state laser interferometry. *Appl. Opt.*, 38:2471–2477, 1999.

[103] Z. Huang, Y. Zhu, X. Chen, and A. B. Wang. Intrinsic fabry-perot fiber sensor for temperature and strain measurements. *IEEE Photon. Technol. Lett.*, 17:2403–2405, 2005.

[104] R. Jha, J. Villatoro, G. Badenes, and V. Pruneri. Refractometry based on a photonic crystal fiber interferometer. *Opt. Lett.*, 34:617–619, 2009.

[105] Y. J. Rao, T. Zhu, X. C. Yang, and D. W. Duan. In-line fiber-optic etalon formed by hollow-core photonic crystal fiber. *Opt. Lett.*, 32:2662–2664, 2007.

[106] Y. J. Rao, M. Deng, T. Zhu, and H. Li. In-line Fabry-Perot etalons based on hollow-core photonic bandgap fibers for high-temperature applications. *J. Lightwave Technol.*, 27:4360–4365, 2009.

[107] X. W. Wang, J. Ch. Xu, Zh. Wang, K. L. Cooper, and A. B. Wang. Intrinsic fabry-perot interferometer with a micrometric tip for biomedical applications. In *in Proceedings of the IEEE 32nd Annual Northeast on Bioengineering Conference 2006*, pages 55–56, Easton, PA., 2006.

[108] S. L. Pan and J. P. Yao. A wavelength-tunable single-longitudinal-mode fiber ring laser with a large sidemode suppression and improved stability. *IEEE Photon. Technol. Lett.*, 22:413–415, 2010.

[109] L. Xiao, W. Jin, and M. S. Demokan. Fusion splicing small-core photonic crystal fibers and single-mode fibers by repeated arc discharges. *Opt. Lett.*, 32:115–117, 2007.

[110] Datasheet of HC-1550. http://www.nktphotonics.com/files/files/hc-1550-02-100409.pdf.

[111] M. Belal, Z. Song, Y. Jung, G. Brambilla, and T. P. Newson. Optical fiber microwire current sensor. *Opt. Lett.*, 35:3045–3047, 2010.

Curriculum Vita

Full Name Xiaozhen Wang

Education Ph.D. (2008–2012)
Department of Physics,
University of Ottawa, Canada
Supervisor: Prof. Xiaoyi Bao

Ph.D. student (2005–2008)
Department of Electronic Engineering,
Xiamen University, P. R. China
Supervisor: Prof. Xiaopeng Dong

B.E. (2001–2005)
Department of Electronic Engineering,
Xiamen University, P. R. China

List of publications

Journal Papers

Xiaozhen Wang, Wenhai Li, Liang Chen, and Xiaoyi Bao, "Thermal and mechanical

properties of tapered single mode fiber measured by OFDR and its application for high-sensitivity force measurement", *Optics Express*, 20 (14), 14779–4788, 2012.

Ping Lu, Ganbin Lin, **Xiaozhen Wang**, Liang Chen, and Xiaoyi Bao, "Lateral squeezing measurement using a tapered fiber Mach-Zehnder interferometer ", Submitted to *IEEE Photonics Technology Letters*, 2012.

Ganbin Lin, Ping Lu, **Xiaozhen Wang**, Dapeng Zhou, and Xiaoyi Bao,"Birefringence characterization of twin-core fiber using OFDR ", Submitted to *IEEE Photonics Technology Letters*, 2012.

Xiaozhen Wang, Wenhai Li, Liang Chen, and Xiaoyi Bao, "Distributed mode coupling measurement along tapered single-mode fibers with optical frequency-domain reflectometry", *IEEE Journal of Lightwave Technology*, 30 (10), 1499–1508, 2012.

Xiaozhen Wang, Tao Zhu, Liang Chen, and Xiaoyi Bao, "Tunable Fabry-Perot filter using hollow-core photonic bandgap fiber and micro-fiber for a narrow-linewidth laser", *Optics Express*, 19 (10), 9617–9625, 2011.

Guolu Yin, **Xiaozhen Wang**, and Xiaoyi Bao, "The effect of beam waists on performance of the tunable fiber laser based on in-line two-taper Mach-Zehnder interferometer filter", *Applied Optics*, 50 (29), 5714–5720, 2011.

Yi Li, **Xiaozhen Wang**, and Xiaoyi Bao, "Sensitive acoustic vibration sensor using single-mode fiber tapers", *Applied Optics*, 50 (10), 1873–1878, 2011.

Xiaozhen Wang, Yi Li, and Xiaoyi Bao, "C- and L-band tunable fiber ring laser using a two-taper Mach-Zehnder interferometer filter", *Optics Letters*, 35 (20), 3354–3356, 2010.

Xiaozhen Wang, Yi Li, and Xiaoyi Bao, "Tunable ring laser using a tapered single mode fiber tip", *Applied Optics*, 48 (35), 6827–6831, 2009.

Wang Xiaozhen, Xiaopeng Dong, and Xie Zuosheng, "Measurement and analysis of the birefringence of photonic crystal fiber with wavelength scanning method", *Optical and Quantum Electronics*, 39, 1081–1090, 2007.

Xiaopeng Dong, Xie Zuosheng, **Wang Xiaozhen**, and Jin hailan, "Design and analysis of novel wave-plate made by the photonic crystal fibers", Journal of Optoelectronics and Laser, Supplement, 125–127, 2006.

Conference presentations

Xiaozhen Wang, Wenhai Li, Liang Chen, and Xiaoyi Bao, "High-sensitivity force measurement using optical tapered fiber with optical frequency-domain reflectometry", in Proceedings of the 22^{nd} International Conference on Optical Fiber Sensors, Beijing, China, Oct. 2012.

Xiaozhen Wang, Tao Zhu, Liang Chen, and Xiaoyi Bao, "Tunable Fabry-Perot filter based on hollow-core photonic bandgap fiber and micro-fiber and its application", , *Proc. SPIE 7753, 77530E, in Proceedings of the 21^{st} International Conference on Optical Fiber Sensors*, Ottawa, Canada, May. 2011.

Xiaozhen Wang, Yi Li, Liang Chen, and Xiaoyi Bao, "Tunable light source using a chemical polished fiber tip as a filter", *Conference of Photonics North*, Niagara Falls, Canada, Jun. 2010.

Xiaozhen Wang, Yi Li, and Xiaoyi Bao, "Tunable fiber ring laser using a two-taper Mach-Zehnder interferometer filter", *Conference of CIPI 2010 Annual General Meeting*, Niagara Falls, Canada, Jun. 2010.

Yi Li, **Xiaozhen Wang**, and Xiaoyi Bao, "Acoustic emission sensor based on biconical fiber microtapers", *Proc. SPIE Int. Soc. Opt. Eng. 7503, 75032V, in Proceedings of the 20^{th} International Conference on Optical Fiber Sensors*, UK, Oct. 2009.

Wang Xiaozhen, Xiaopeng Dong, and Li Weiwen, "Analysis of the sensitivity enhanced refractive index sensing characteristics with optical fiber Bragg gratings", the 13^{rd} National Conference on Optical Fiber Communication and the 14^{th} National Conference on Integrated Optics (OFCIO 2007), Nanjing, China, Nov. 2007.

Xiaopeng Dong, **Wang Xiaozhen**, and Xie Zuosheng, "Measurement and analysis of

the birefringence of photonic crystal fiber with wavelength scanning method", the 4th International Conference on Materials for Advanced Technologies (ICMAT 2007), Singapore, Jul. 2007.

Xiaopeng Dong, Xie Zuosheng, and **Wang Xiaozhen**, "Design and analysis of novel wave-plate made by the photonic crystal fibers", Symposium on the Academics and Strategy Development of the Optoelectronics in China, Sanya, China, Dec. 2006.